Progress in Surface Science 92 (2017) 203–239

Contents lists available at ScienceDirect

Progress in Surface Science

journal homepage: www.elsevier.com/locate/progsurf

Review article

Atomic-scale investigation of nuclear quantum effects of surface water: Experiments and theory

Jing Guo[a], Xin-Zheng Li[b,c], Jinbo Peng[a], En-Ge Wang[a,c,*], Ying Jiang[a,c,*]

[a] International Center for Quantum Materials, School of Physics, Peking University, Beijing 100871, PR China
[b] School of Physics, Peking University, Beijing 100871, PR China
[c] Collaborative Innovation Center of Quantum Matter, Beijing 100871, PR China

ARTICLE INFO

Keywords:
Scanning tunneling microscopy
Path-integral molecular dynamics
Water molecule
Nuclear quantum effects
Hydrogen bond

ABSTRACT

Quantum behaviors of protons in terms of tunneling and zero-point motion have significant effects on the macroscopic properties, structure, and dynamics of water even at room temperature or higher. In spite of tremendous theoretical and experimental efforts, accurate and quantitative description of the nuclear quantum effects (NQEs) is still challenging. The main difficulty lies in that the NQEs are extremely susceptible to the structural inhomogeneity and local environments, especially when interfacial systems are concerned. In this review article, we will highlight the recent advances of scanning tunneling microscopy and spectroscopy (STM/S), which allows the access to the quantum degree of freedom of protons both in real and energy space. In addition, we will also introduce recent development of *ab initio* path-integral molecular dynamics (PIMD) simulations at surfaces/interfaces, in which both the electrons and nuclei are treated as quantum particles in contrast to traditional *ab initio* molecular dynamics (MD). Then we will discuss how the combination of STM/S and PIMD are used to directly visualize the concerted quantum tunneling of protons within the water clusters and quantify the impact of zero-point motion on the strength of a single hydrogen bond (H bond) at a water/solid interface. Those results may open up the new possibility of exploring the exotic quantum states of light nuclei at surfaces, as well as the quantum coupling between the electrons and nuclei.

1. Introduction

1.1. Nuclear quantum effects (NQEs)

Water is vital to human's daily life and has been extensively investigated throughout the history of science. However, the molecular-level understanding of the structure and many unusual properties of water still remains a great challenge in spite of the persistent development of new scientific instruments and theoretical methods. The mystery of water mainly arises from the

Abbreviations: STM, Scanning tunneling microscopy; STS, Scanning tunneling spectroscopy; IETS, Inelastic electron tunneling spectroscopy; EELS, Electron energy loss spectroscopy; SFG, Sum-frequency generation spectroscopy; NMR, Nuclear magnetic resonance; XRD, X-ray diffraction; IR spectroscopy, Infrared spectroscopy; nc-AFM, Noncontact atomic force microscopy; NV center, Nitrogen-vacancy center; PIMD, Path-integral molecular dynamics; MD, Molecular dynamics; MC simulations, Monte-Carlo simulations; DFT, Density functional theory; VASP, Vienna *ab initio* simulation package code; PES, Potential energy surface; TI, Thermodynamic integration; cNEB, Climbing image nudged elastic band; NQEs, Nuclear quantum effects; H bond, Hydrogen bond; DOS, Density of states; HOMO, Highest occupied molecular orbital; LUMO, Lowest unoccupied molecular orbital; PDOS, Projected density of states; E_F, Fermi level; vdW, Van der Waals; ZPM, Zero-point motion; ZPE, Zero-point energy; D, Deuterium; H_3S, Hydrogen sulfide; HF, Hydrogen fluoride; C_6H_{12}, Cyclohexan; AS, Anticlockwise state; CS, Clockwise state

* Corresponding authors at: International Center for Quantum Materials, School of Physics, Peking University, Beijing 100871, PR China.
E-mail addresses: egwang@pku.edu.cn (E.-G. Wang), yjiang@pku.edu.cn (Y. Jiang).

https://doi.org/10.1016/j.progsurf.2017.11.001

Available online 21 November 2017

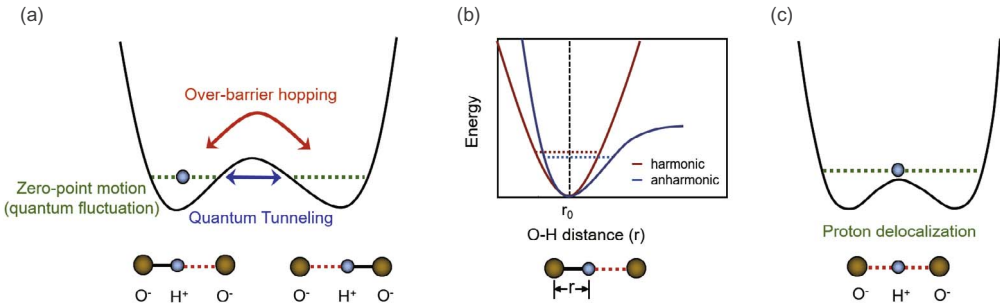

Fig. 1. Nuclear quantum effects of H bond. (a) Symmetric double-well potential of interconversion between covalent bond and H bond via proton transfer. Red and blue double-ended arrows denote over-barrier hopping and quantum tunneling of proton, respectively. The zero-point motion (quantum fluctuation) of protons is depicted by dotted green lines. (b) Schematic of the harmonic (red) and anharmonic (blue) zero-point motion of the proton. r_0 denotes the equilibrium O—H distance under the harmonic potential. (c) Reduction of the reaction barrier leading to the proton delocalization and, consequently, symmetric H bond.

intermolecular hydrogen-bonding (H-bonding) interaction. It is well known that H bonds have a strong classic component coming from electrostatics. However, its quantum component can be exceptionally prominent due to the quantum motion of light H nuclei (proton), which play important roles in the structure, dynamics, and macroscopic properties of H-bonded materials [1–10]. Therefore, the accurate assessment of NQEs has been a key issue for the understanding of many extraordinary physical and chemical properties of water.

The NQEs of water mainly arise from quantum tunneling and zero-point motion (ZPM) of protons. In water, the H atom links two oxygen atoms via a covalent bond at one side and a H bond at the other side. Classically, the covalent bond and H bond could be switched through over-barrier proton hopping, as shown in Fig. 1a. Nevertheless, such a switching can be also realized by proton tunneling (Fig. 1a) when the height and width of the potential barrier is sufficiently small, which has been observed in many H-bonded systems [1,11–17]. Another quantum nature of proton is ZPM or quantum fluctuation. Unlike classical particles, which are localized in the local minimum of potential well, protons constantly fluctuate at zero-point energy (ZPE) state due to the Heisenberg uncertainty principle. In a harmonic potential well, the ZPM is symmetric, making the averaged position of the proton coincides with the local minimum of potential well (Fig. 1b). However, the real potential profile of O—H···O has an anharmonic character. The anharmonic ZPM of H nuclei causes the O—H covalent bond to expand with respect to the case under harmonic potential, thus the H-bonding strength is enhanced (Fig. 1b). Once the reaction barrier of the proton transfer is significantly reduced, the ZPE plays a decisive role. In this situation, the proton will be totally delocalized and equally shared by the oxygen atoms, leading to a symmetric H bond (Fig. 1c).

1.2. The impact of NQEs on the structure and properties of water and ice

The NQEs usually show up in isotopic substitution experiments. When replacing hydrogen (H) atoms with heavier deuterium (D) atoms, macroscopic properties of water exhibit significant isotope effects, which have been explicitly summarized in a recent review [7]. For example, the melting temperature is increased by 3.82 K upon substituting D with H [18,19] and the temperature of the maximum density is 7.21 K higher in D_2O compared with H_2O [20,21]. Upon deuteration, the viscosity increases 23% accompanied by a 23% decrease in water diffusion [19,20,22,23]. Spectroscopic studies of liquid water at ambient temperature provide evidence that D_2O is more structured than H_2O [2,24–27]. These observations suggest that the H-bonding strength is enhanced when exchanging H with D, namely, the NQEs incline to weaken the H-bonding strength in liquid water at room temperature. However, the opposite trend appears at higher temperature [18,28] and conflicting theoretical simulations also exist [29]. So far, a consensus is not reached and it remains an open question how large the quantum component of H bond is.

The NQEs in water/ice become more prominent at low temperature or when the O—O distance of water molecules is small [1,30,31], for example, under high pressure, confined in the nano-cavity or at interfaces. The proton dynamics in ice I_h (hexagonal ice) and ice I_c (cubic ice) does not freeze out even down to 5 K, suggesting the existence of the concerted proton tunneling [17]. However, the direct evidence of the concerted proton tunneling is still lacking and under debate [11,17,32–34]. In particular, high-pressure ice has received considerable attention since the intermolecular distance can be continuously tuned by applying high pressure. As the pressure is increased, the ice undergoes phase transition from ice VIII to ice VII, which is believed to be driven by proton tunneling [1]. Symmetric ice X appears at even higher pressure as a result of zero-point fluctuations, in which the proton sits exactly halfway between the two oxygen atoms [1,35–37].

The adsorption of water on various solid surfaces gained extensive attention as well, as it is ubiquitous in nature and plays a crucial role in a great many environmental, biophysical, catalysis and even technological processes [3,38–44]. The distance between adjacent water molecules is subjected to the atomic arrangement of the surfaces because of the water-substrate interaction. Li et al. reported the substrate dependent NQEs of the H bond by quantum calculations, where the magnitude of proton delocalization between two oxygen atoms was determined by the substrate lattice constant, resulting in partially (on Pt(111) and Ru(0001)) or totally (on Ni(111)) symmetric H bonds [45]. Meanwhile, Kumagai et al. discovered the symmetric H bond in a water-hydroxyl complex on Cu(110) from real-space experiments [46]. In addition, the high diffusion rate of water dimers on Pd(111) at low

temperature [47] was supposed to arise from the H-bonding tunneling dynamics of the dimer [48]. Then proton tunneling processes were visualized in a water dimer adsorbed on a Cu(110) surface [49].

Interestingly, water under nano-confinement shows many anomalous behaviors [50–61]. For example, extremely fast proton transport through nanochannels and exceedingly wide-range phase transition temperature of water confined in carbon nanotubes were reported [50,51,53,61]. Water confined in a carbon nanotube shows the signature of proton delocalization at low temperature [56]. More strikingly, it was recently found that a single water molecule confined inside a hexagonal shaped channel of the gemstone beryl exhibited a new quantum state, in which the proton is delocalized and tunnels between the six symmetrically equivalent positions [60].

1.3. NQEs in other H-bonded materials and biological systems

Besides water, NQEs exist in other H-bonded materials as well. In the recently discovered superconducting hydrogen sulfide (H_3S) system, which shows the highest superconducting transition temperature T_c of 203 K under high pressure, there is a pronounced isotope effect on T_c [62]. In addition, it was revealed that the superconducting phase only emerged upon H-bond symmetrization, in which the H atoms reside exactly midway between two sulfur atoms [5]. When the protons are treated as quantum particles, the symmetrization pressure will be greatly lowered due to the ZPM of the protons. Therefore, NQEs influence the superconducting phase diagram of hydrogen sulfide dramatically [5]. NQEs could also influence H-bonding interactions and consequently the structure of other H-bonded materials, for instance, hydrogen fluoride (HF) systems [63,64], cyclohexane (C_6H_{12}) molecules and superstructures on metal surfaces [65], protonated and hydroxylated water [30,31].

NQEs also play key roles in many biological processes such as DNA tautomerization [66–68] and enzyme catalysis reactions [69–74]. It was shown that the enzyme-catalyzed reaction was dominated by proton tunneling [75] and exhibited a large kinetic isotope effect greater than 100 [76,77]. The enzyme ketosteroid isomerase contains a H-bonded network at its active site, which facilitates the quantum delocalization of protons, leading to a pronounced isotope effect on its acidity [73]. Another interesting finding is that protein is more stable in D_2O compared with H_2O [78,79] and the bacteria can survive in pure D_2O environment [80].

Now we can clearly see that NQEs could not just be treated as corrections to the classical H bond interactions. Instead, NQEs could have a decisive impact in the structure, dynamics, and macroscopic properties of H-bonded materials and biological systems. Although the studies of NQEs in water and aqueous systems have been summarized in several excellent reviews [4,7–9], the accurate and quantitative description of NQEs is very scarce mainly due to the great challenge in pursuing a proper treatment of the nuclear motion at a quantum mechanical level in theory and the lack of atomic-scale experimental techniques for condensed phases. In this review, we focused on the atomic-scale investigation of NQEs of surface water with the recently advanced STM technique and PIMD calculation method.

1.4. Experimental and theoretical challenges of studying NQEs

Theoretically, one needs to go beyond the traditional “ball-and-stick” model for the description of the chemical bonding interactions [81]. The most rigorous treatment resides on generating a high-dimensional potential energy surface (PES) for all nuclear degrees of freedom in the configuration space and solving the corresponding Schrödinger equation for the many-body entity of the nuclei. Because of the scaling problem, the targeting systems are normally restricted to very small ones related to gas phase reactions [82–84]. Starting from the 1980s, an alternative treatment based on the Feynman’s path-integral representation of the quantum mechanics has earned popularity in simulations of large molecular and condensed matter systems [30,31,45,85–102]. Simulations on the influence of NQEs on H bonds, on surface geometries and reactions, and surface water emerged and started to shed light on the atomic level details of these problems [7,29,32,63,64,103–111]. Despite enormous theoretical efforts toward pursuing proper treatment of the nuclear motion at a quantum mechanical level, accurate and quantitative description of NQEs on the H-bonding interaction has proven to be experimentally challenging.

Conventional experimental methods of studying NQEs are summarized in Table 1, such as sum-frequency generation (SFG) [126], X-ray diffraction (XRD) [2,35], nuclear magnetic resonance (NMR) [11], neutron scattering [60,112–114,120,134,135], and so on. Spectroscopic studies offer valuable insights into the nuclear quantum behaviors of H-bonded materials. However, those techniques have poor spatial resolution and only measure the average properties of many H bonds, which are susceptible to structural inhomogeneity and local environments [15,136]. Subsequently, the spatial variation and interbond coupling of H bonds lead to spectral broadening, which on the one hand results in the difficulty of spectral assignment, on the other hand may easily smear out the subtle details of NQEs.

Scanning tunneling microscopy (STM) is a promising tool to probe the NQEs of surface water at the atomic-level, with sub-Ångström spatial resolution [137–139], single-bond vibrational sensitivity [140–142] and atom/molecule manipulation capability [143,144]. In the past decade, STM has been extensively used to investigate the structure and dynamics of water on solid surfaces [3,15,40,145–150]. However, it is not easy to apply STM to study the NQEs of surface water. The main reason lies in that STM is based on the principle of electron quantum tunneling and the tunneling current is only sensitive to the density of states (DOS) of electrons around the Fermi level (E_F) rather than the nuclei. One viable way to probe the NQEs is via electron-nuclei coupling, but this requires exceptionally high sensitivity of STM to the frontier orbitals. Unfortunately, water is a close-shell molecule, so the frontier orbitals of adsorbed water are located far away from the E_F, resulting in very poor signal-to-noise ratio for imaging and spectroscopy of STM.

In order to overcome the intrinsic limitation, we have developed a series of experimental techniques based on STM, which allow us to access the degree of freedom of protons both in real and energy space. As shown in Section 2, we achieved submolecular-

Table 1
Summary of experimental studies of NQEs.

Technique	System	Exhibition of NQEs	Ref(s).
Neutron scattering	Supercooled water	Proton delocalization	[112]
	Ice	Concerted proton tunneling	[17]
	Ice and water	NQEs on the proton's delocalization and vibrational properties	[113–119]
	Nanoconfined water	Proton delocalization	[56,60,120]
	Water in Beryl	Proton tunneling	[60]
XRD	High pressure ice	H-bond symmetrization (ice X)	[35]
	H-bonded materials	Isotope effects on the local structure	[2,26,121]
	Enzyme-catalyzed reaction	Proton tunneling	[75,122]
EELS	Hydrogen atoms on metal surfaces	Proton delocalization	[10]
Raman spectroscopy	High pressure ice	H-bond symmetrization (ice X)	[28,36]
IR spectroscopy	High pressure ice	H-bond symmetrization (ice X)	[123,124]
	Cyclohexane on Rh(111)	NQEs on the H-bond (C—H···Metal) interaction	[65]
Brillouin spectroscopy	High pressure ice	H-bond symmetrization (ice X)	[125]
SFG	Interfacial water (HOD)	NQEs on the bond orientation	[126]
Rotational spectroscopy	Water hexamer prism	Concerted proton tunneling	[16]
Dielectric measurement	Ice	Concerted proton tunneling	[34]
NMR	Solid p-*tert*-butyl calix arene	Concerted proton tunneling	[11]
STM	Single hydrogen atoms on Cu(001)	Proton tunneling	[13]
	Heave atoms and molecules on Cu(111)	Quantum tunneling	[127–129]
	Water dimer and hydroxyl complexes on Cu(110)	Proton tunneling	[14,49,130]
	Water–hydroxyl complex on Cu(110)	H-bond symmetrization	[46]
	Water tetramer on NaCl(001)	Concerted proton tunneling	[131]
	Water monomer on NaCl(001)	NQEs on the H bond strength	[132]
	Porphycene molecule on Ag(110)	Proton tunneling	[133]

resolution orbital imaging of water by tuning the tip-water coupling, from which we can discern the O—H directionality of water monomer and discriminate the H-bonding chirality of water clusters. By developing tip-enhanced inelastic electron tunneling spectroscopy (IETS) [140,151,152], we obtained the vibrational spectroscopy of water with enhanced signal-to-noise ratio at single molecule level, which can be employed as an ideal probe for sensing the quantum motion of protons. Theoretically, we have implemented highly efficient path-integral molecular dynamics (PIMD) simulations, in which both electrons and nucleus are treated as quantum particles (Section 3). Based on those novel techniques and methods, we highlight the possibility of atomic-scale investigation of NQEs of surface water in the subsequent sections. In Section 4, we directly visualized the concerted quantum tunneling of protons within the water tetramer by monitoring the reversible interchange of H-bonding chirality in a controlled fashion with a Cl-terminated tip. The influence of the atomic-scale local environment on the concerted proton tunneling is also discussed. In Section 5, we quantitatively assessed the quantum component of a single H bond at a water-solid interface, revealing that the anharmonic quantum fluctuations of H nuclei weaken the weak H bonds and strengthen the relatively strong ones. However, this trend could be reversed when the H bond is strongly coupled to the atomic-scale polar environment. Finally, we summarize the review in Section 6 and provide an outlook for the future investigation of NQEs in water as well as the new possibilities provided by recently developed scanning probe techniques.

2. Recent advances of STM towards accessing the degree of freedom of protons

2.1. Submolecular-resolution imaging of interfacial water

2.1.1. Background

One basic requirement for studying the NQEs of water by scanning probe methods is to locate in real space the position of protons within the H-bonded network, such that the motion of the protons can be tracked. This requires the ability to access the internal degree of freedom of water molecule, namely, to achieve submolecular-resolution imaging. To date, STM has been extensively applied to image the H-bonding configurations of water at surfaces since the beginning of this century. So far, the majority of the work is focused on metal surfaces since STM normally requires conductive substrates. The clustering and wetting behavior of water molecules on noble metal surfaces have been reviewed in Refs. [3,40,145–147]. The structural diversity of water nanoclusters and overlayers on various metal substrates arises from the delicate interplay between the water-water and water-metal interactions [153–160].

However, in the previous STM studies it was very difficult to resolve the internal structure of water molecule and discern the O—H directionality. The main reason is that water is a close-shell molecule and the frontier orbitals of water are located very far away from the E_F. Thus, the water molecule simply acts as an energy barrier for the electrons to tunnel through, thus prohibiting the imaging of submolecular features. In addition, the strong electronic coupling between the water and the metal substrates may easily smear out the fine orbital structures of water.

In order to overcome these limitations, we firstly inserted an ultrathin insulating NaCl(001) bilayer between the Au(111) substrate and water molecules to electronically decouple the water molecules from the metal substrate, such that the native molecular

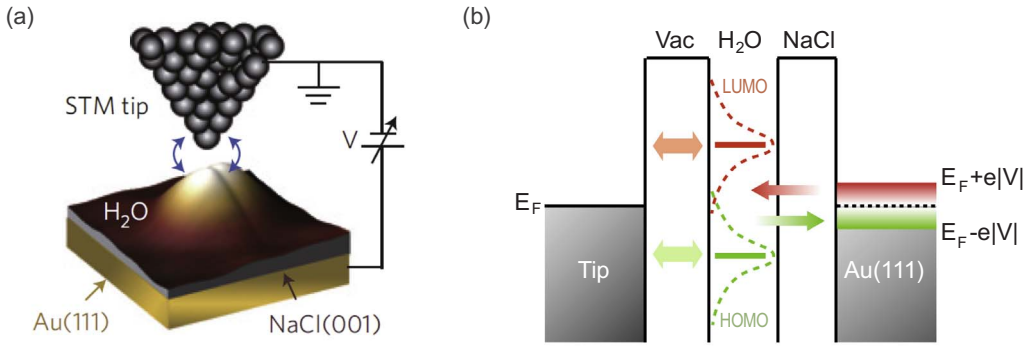

Fig. 2. The mechanism of orbital imaging of water molecules. (a) Schematic of the experimental setup. The insulating NaCl(001) bilayer between the Au(111) substrate and water molecule electronically decouples the water molecule from the metal substrate. The double-ended blue arrows in (a) denote the tip-water coupling. (b) Double-barrier single-molecule junction of water. The broadenings of HOMO and LUMO (green and red dashed curves) are induced by the coupling of the HOMO and LUMO with the tip (double-ended green and red arrows). The single-ended green and red arrows denote the flowing directions of tunneling currents at the positive and negative biases, respectively. Reproduced from Ref. [175] with permission.

orbitals of water are mostly preserved (Fig. 2a). Second, STM tip was employed as a top gate to enhance the molecular DOS of water around the E_F in a controlled fashion via tip-water coupling (Fig. 2b). These key steps enabled us to image the frontier molecular orbitals of water molecules near the zero bias, which are spatially locked together with its geometric structure. The submolecular-resolution orbital images not only allow the direct identification of the topology of the H-bonded network, but also open up the possibility of accessing the degree of freedom of protons in real space. The details are described in the following.

2.1.2. Methods

The experiments were performed in an ultra-high vacuum low temperature STM (*Createc*, Germany) with the base pressure better than 5×10^{-11} mbar. The Au(111) single crystal was cleaned by repeatedly sputtering with Argon ion at 1 keV and followed annealing at about 900 K for 10 min, forming a Au(111)-22 × √3 reconstructed surface. The NaCl (Sigma Aldrich, 99.999%) was then evaporated thermally from a Knudsen-cell at a temperature of 720 K onto the Au(111) surface held at room temperature for 2 min. The ultrapure H_2O (Sigma Aldrich, deuterium-depleted) was further purified under vacuum by freeze-pumpthaw cycles to remove remaining impurities. The H_2O molecules were dosed *in situ* onto the Au-supported NaCl(001) surface at 5 K or 77 K through a dosing tube, which pointed toward the sample from a distance of about 6 cm. The subsequent STM measurements were performed at 5 K or 77 K with electrochemically etched tungsten tips, which were cleaned by alternating annealing and sputtering before the experiments. The STM tip is further optimized *in situ* by applying voltage pulse (2–10 V) and repeatedly indenting into the Au surface until the STM images shows sharp contrast at the step edges. Bias voltage refers to the sample voltage with respect to the tip. All STM topographic images were obtained in constant current mode. The scanning tunneling spectroscopy (STS) dI/dV spectra were acquired using lock-in detection of the tunneling current by adding a 10 mV_{rms} modulation at 250 Hz to the sample bias. Image processing was performed by *Nanotec* WSxM [161].

Density functional theory (DFT) calculations were performed using Vienna *ab initio* simulation package code (VASP) [162,163] to study the adsorption configuration of water monomers and nanoclusters on the NaCl surface. Van der Waals (vdW) corrections for dispersion forces were considered within the vdW-DF scheme by using the optB88-vdW method [164]. Projector augmented-wave pseudopotentials [165] were used together with a plane wave basis set and a cutoff energy of 550 eV for the expansion of the electronic wave functions. In the DFT calculation, we constructed a NaCl/Au coincidence structure by superposing a NaCl (2 × 2) unit cell on a $\begin{pmatrix} 3 & 1 \\ 1 & 3 \end{pmatrix}$ superstructure of the Au(111) substrate with a residual strain of about 5%. To match the square symmetry of the NaCl(001) lattice, the angle of the $\begin{pmatrix} 3 & 1 \\ 1 & 3 \end{pmatrix}$ supercell of the Au(111) substrate was changed from 82° to 90°. The Au substrate was modelled by a four-layer slab and a bilayer NaCl(001) slab with a lattice constant of 5.665 Å was used.

2.1.3. Orbital imaging of water monomers

STM image of clean Au(111) shows the characteristic 22 × √3 reconstructed surface, where the atoms of surface layer occupy both the hcp and the fcc sites (Fig. 3a). The domain walls between the hcp and the fcc regions form the so-called herringbone structures. The NaCl inclines to nucleate at the step edges of the Au(111) substrate with a carpet-like growth mode and forms bilayer(001)-terminated islands (Fig. 3b) [166]. Recently, Mattaei et al. have clarified that the carpet-like growth mode is driven by the maximization of electrostatic interaction between the NaCl nanostructure and a metal step edge, and not its minimization [167]. In the atomically resolved STM image of the NaCl film (inset of Fig. 3b), the Cl^- anions are visualized as round protrusions and the Na^+ cations are invisible because of the higher DOS around the E_F at the Cl^- sites than the Na^+ sites [168].

Upon dosing water on Au(111)-supported NaCl(001) surfaces at 5 K, the water molecules were frozen on the surface, leading to the formation of isolated water monomers appearing as bright protrusions in the STM image (Fig. 3c). The water monomer exhibited symmetric double-lobe structures with two orthogonal adsorption orientations (Fig. 3d and e). With the square lattice of the

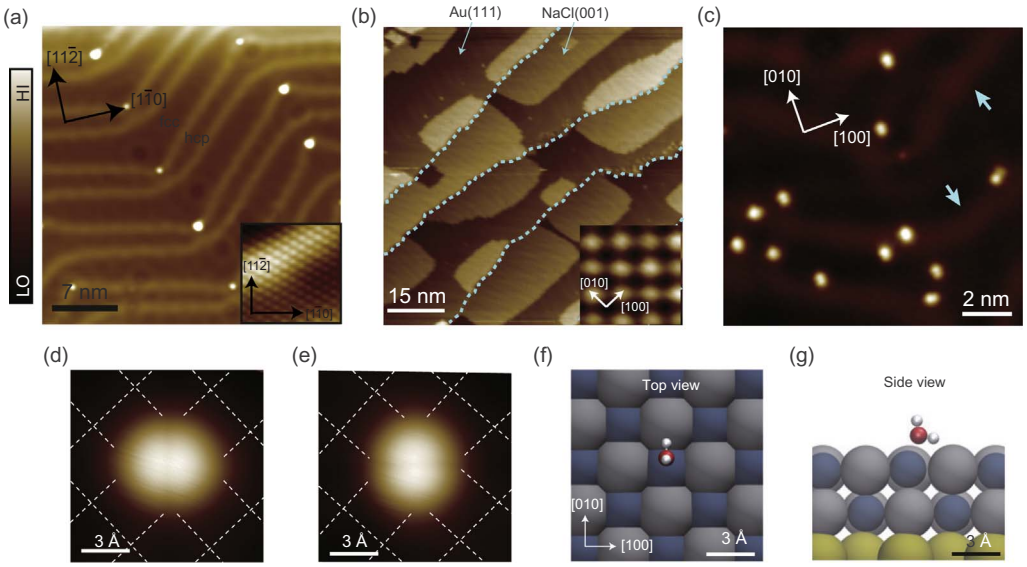

Fig. 3. Water monomers adsorbed on the Au-supported NaCl(001) films. (a) STM image of the Au(111) $22 \times \sqrt{3}$ reconstruction surface with herringbone structures. The inset is the atomically resolved STM image of Au(111) substrate. The size of the inset is $3 \times 3\,nm^2$. (b) STM topography of bilayer NaCl(001) islands supported by the Au(111) substrate. The inset is zoom-in STM image of NaCl(001) surface with atomic resolution. Cyan dotted lines denote the step edges of the Au(111) substrate. (c) STM image of water monomers adsorbed on the Au-supported NaCl(001) surface. The single protrusions correspond to individual water monomers. Herringbone structures of the underlying Au(111) substrate are highlighted by cyan arrows. (d, e) High-resolution STM images of water monomers with orthogonal orientations, in which the square lattices of NaCl(001) surface arising from the Cl^- are superimposed (white grids). (f, g) Calculated adsorption configuration of a water monomer on NaCl(001)/Au(111) surface. O, H, Au, Cl^- and Na^+ are denoted by red, white, gold, gray and dark-cyan spheres, respectively. The scanning set points are (a) 1 V, 20 pA; inset: 10 mV, 2 nA; (b) 2 V, 9 pA; inset: 50 mV, 20 pA; (c–e) 100 mV, 50 pA. The STM images were obtained at 5 K. Reproduced from Ref. [175] with permission.

underling NaCl surface superimposed, we found that the water monomer adsorbed on the top site of Na^+ along the orientation of Na^+-Cl^- direction. DFT calculations revealed that water monomer adsorbed on the NaCl surface with a "standing" configuration with one OH pointing upwards to the vacuum, the other OH pointing toward the NaCl surface (Fig. 3f and g), which is stabilized by the long-range van der Waals forces from the Au substrate and against the "flat" configuration of water monomers on metal and NaCl surfaces reported previously [169–171].

Fig. 4a is the calculated projected density of states (PDOS) for a water monomer adsorbed on the Au-supported NaCl(001) films. Due to the decoupling effect of NaCl bilayer, the native molecular orbitals of water are mostly preserved and the broadenings of the HOMO and LUMO are very small. It is obvious that the highest occupied molecular orbital (HOMO) and lowest unoccupied molecular orbital (LUMO) locate far away from the E_F, resulting in negligible DOS of the water molecule within the energy range of $\pm$ 2 V. In principle, one can directly image the HOMO and LUMO through resonant tunneling, just as demonstrated for organic molecules on NaCl surface [137]. However, this method is not applicable to water molecules, since the water would become unstable under such large bias voltages because of vibrational excitation induced by high-energy inelastic tunneling electrons [15,151].

We found that STM tip may electronically couple with the water molecule in agreement with the Newns-Anderson model [172], resulting in the enhancement of molecular DOS around E_F [173]. The calculated PDOS of water monomer with the tip-molecule coupling included exhibited considerable broadening and shift of the HOMO and LUMO towards E_F (Fig. 4b). The tail states below -0.5 eV and the states around E_F are mostly of HOMO character, whereas the states around 0.6 eV are mostly of LUMO character (Fig. 4c). As the tip approaches the monomer, both the HOMO- and LUMO-like states near the E_F are enhanced owing to the increased tip-molecule coupling. Those features were further confirmed by measuring the dI/dV spectra on the water monomer at different tip-water distances (Fig. 4d).

It is worth to mention that HOMO/LUMO bias polarity is reversed when comparing the calculation results (Fig. 4c) with the experimental findings (Fig. 4d). In our experiment, the bias voltage was applied to the sample as shown in the STM set-up (Fig. 2). Normally, HOMO is located at negative bias and LUMO appears at positive bias. However, this is the case for strong molecule-substrate interaction and negligible tip-molecule coupling. In contrast, the decoupling effect provided by NaCl film leads to negligible coupling between the molecule and the Au substrate and the tip-molecule coupling is dominant. Thus, the role of tip and Au substrate are inverted, the tip could be considered as a "nano-substrate" and the Au substrate becomes a "macroscopic tip", leading to the observation of HOMO at positive bias and LUMO at negative bias.

Fig. 5a is a typical high-resolution STM image obtained at a positive bias voltage, showing a double-lobe structure, which agrees perfectly with the calculated HOMO of the water monomer (Fig. 5d). When switching to negative bias, the double-lobe structure almost fades away and an egg-shaped lobe emerges within the nodal plane (Fig. 5b), closely resembling the calculated LUMO feature of the water monomer (Fig. 5e). More interestingly, the HOMO and LUMO can be imaged simultaneously by choosing an appropriate bias voltage (Fig. 5c). It is worth noting that such a composite STM image does not correspond to a simple superposition of the HOMO and LUMO (Fig. 5f), but probably arises from the interference effect between the tunneling paths through the two orbitals.

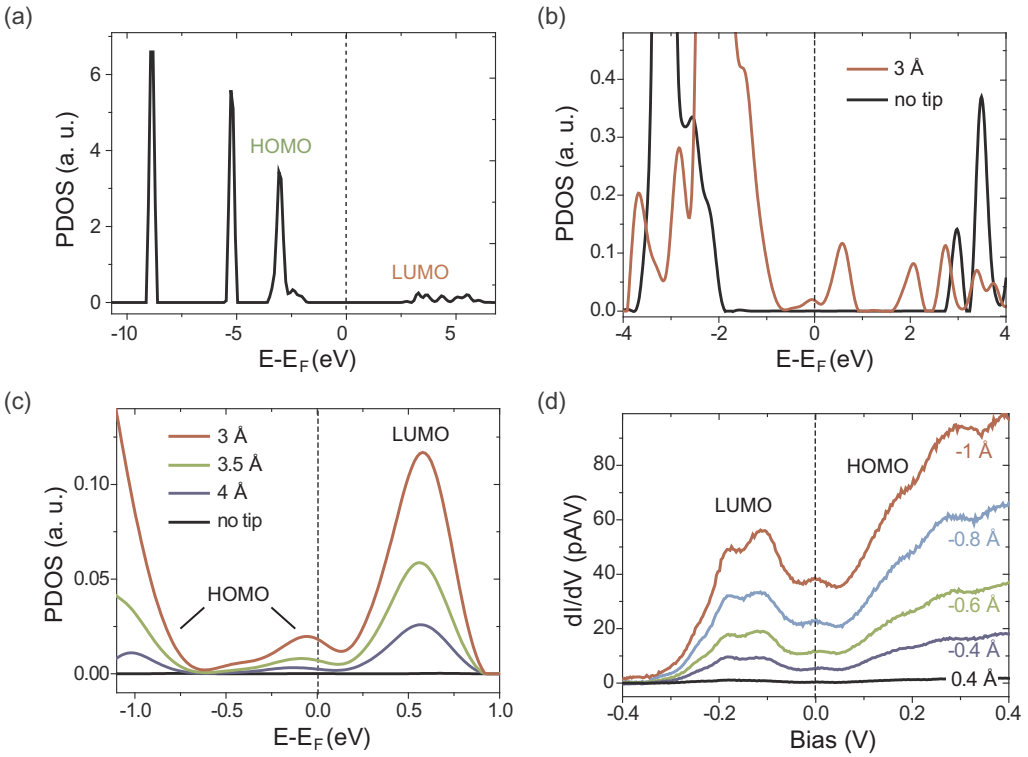

Fig. 4. Gating the HOMO and LUMO states of a water monomer towards the E_F via tip-water coupling. (a) PDOS of a water monomer adsorbed on NaCl(001) projected onto the water molecule. (b) Calculated PDOS of a water monomer with and without tip-water coupling. (c) Zoom in PDOS of water monomer at different tip heights. The tip height is defined as the vertical distance between the endmost atom of the STM tip and the oxygen atom of water. (d) dI/dV spectra of water monomer measured at different tip-water separations with the NaCl background signal removed. Z offsets highlighted in (d) are referenced to the gap set with: V = 100 mV and I = 50 pA. Reproduced from Ref. [175] with permission.

The submolecular-resolution orbital images allow us to distinguish with high precision the orientation of the water molecule on the surface, namely, O—H directionality. The symmetric structure with respect to the nodal plane of the HOMO image (Fig. 5a) indicates that the HOH plane of water is perpendicular to the surface. The egg-shaped LUMO lobe (Fig. 5b) with only one axis of symmetry, allows us to determine that the flat OH bond of the monomer is oriented along the [010] direction of the NaCl(001) surface. Those observations are in excellent agreement with the DFT calculation results (Fig. 3f and g). In addition to the symmetric double-lobe structure, we also observed asymmetric water monomers, whose HOH plane is no longer perpendicular to the NaCl surface (Fig. 6). This is due to the inhomogeneity of the NaCl surface resulting from the herringbone structures of Au substrate.

The tip-modulated orbital imaging is very sensitive to the tip height and the details of the tip apex. With decreasing tip height, the HOMO/LUMO features of water monomers gradually emerge and become prominent as a result of enhanced tip-water coupling. When the tunneling current is fixed, sweeping the bias from positive to negative voltages leads to the gradual change from HOMO to LUMO features. Fig. 7 shows STM images of different water monomers with three typical types of STM tips. It is obvious that different tip apexes result in similar HOMO and LUMO features, but with variation of energy scale and different sensitivities to HOMO and LUMO.

2.1.4. Discrimination of H-bonding chirality of water tetramers

Individual water monomers could be manipulated in a well-controlled manner by a Cl-functionalized STM tip (set point: V = 10 mV, I = 150 pA). This provides an efficient way to construct water tetramers and other clusters. The Cl-terminated tip was obtained by picking up a Cl atom from the NaCl surface (set point: V = 5 mV and I = 5 nA), which can be confirmed by improved resolution and the appearance of a single Cl vacancy (Fig. 8). Fig. 9 shows a complete manipulation sequence of assembling the monomers (Fig. 9a) to form a dimer (Fig. 9c), a trimer (Fig. 9d), and a tetramer (Fig. 9e). We note that the water dimer and trimer are not very stable such that they can be easily disturbed by the tip during scanning. However, the tetramer is quite stable once formed, allowing long-term imaging and spectroscopic measurements.

The water tetramer appears as a square protrusion at large tip height (Fig. 10a), then it turns into an equivalent four lobe structure with decreasing tip-molecule distance (Fig. 10b). DFT calculations show that each water molecule donates and accepts just one H bond and the other four OH bonds point obliquely upward away from the surface (Fig. 10c and d). The O—O distances in the calculated water tetramer on NaCl is 2.75 Å. The O—H distance is 1 Å and the hydrogen bond distance (O—H···O) is 1.75 Å. The hydrogen-bond strength could be estimated from the O—H···O distance (r) using an empirical relation, $E_B = 0.134r^{-3.05}$ (with r in nm

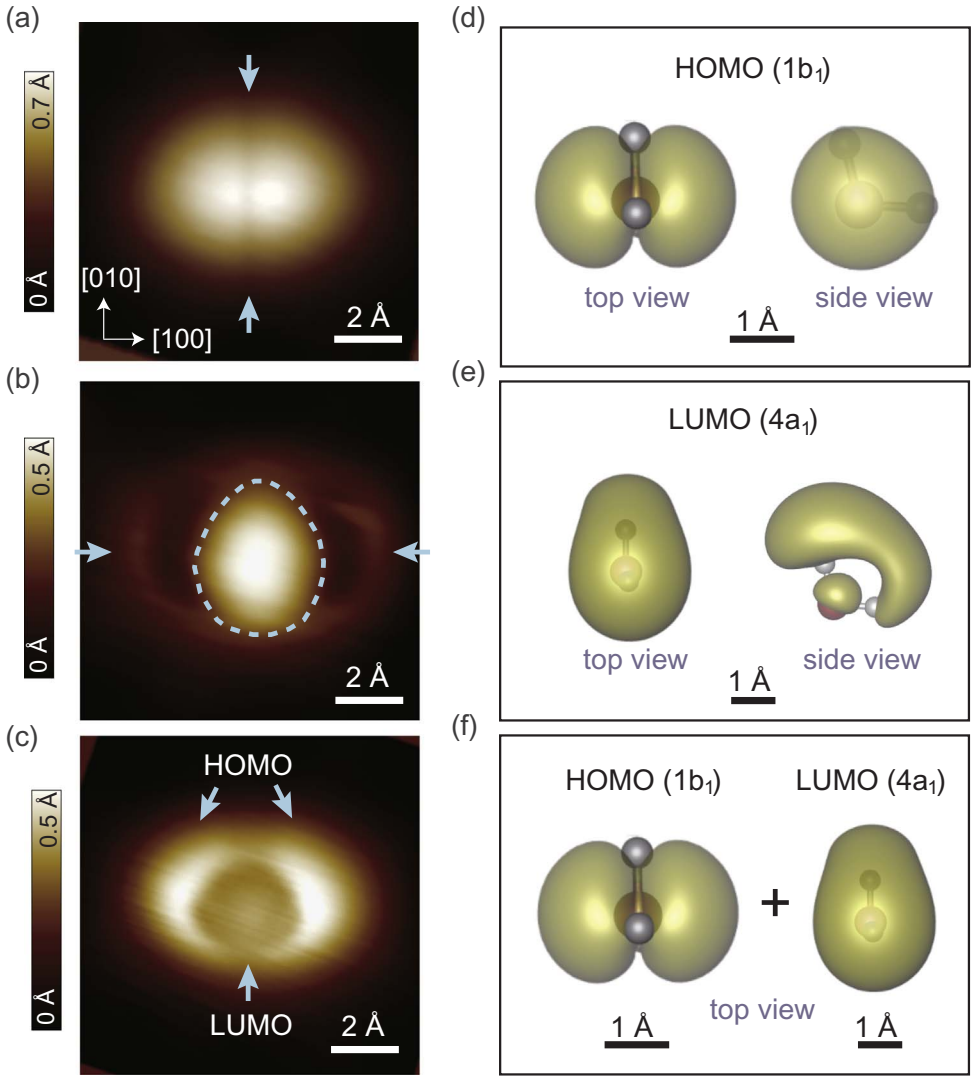

Fig. 5. Orbital imaging of a water monomer. (a–c) High-resolution STM images of HOMO (a), LUMO (b), HOMO + LUMO (c) of a water monomer. The nodal plane of the HOMO is highlighted by the cyan arrows in (a). The dashed oval and arrows in (b) denote the egg shape of the LUMO and the faint ring structures arising from the remaining HOMO, respectively. Set point (a) 100 mV, 500 pA; (b) −100 mV, 800 pA; (c) −50 mV, 550 pA. (d–f) Calculated HOMO(d), LUMO (e), HOMO + LUMO (f) of a water monomer adsorbed on NaCl(001) by plotting isosurfaces of charge densities integrated over 1 eV of the HOMO/LUMO tail close to E_F. O and H atoms of H_2O are denoted by red and light-gray spheres, respectively. The STM images were obtained at 5 K. Reproduced from Ref. [175] with permission.

and E_B in kJ/mol), which is about 27 kJ/mol (280.8 meV). Such a cyclic water tetramer contains two degenerate chiral states, clockwise and anticlockwise H-bonding loops. In a previous work the chirality of H-bonded methanol hexamer was indirectly deduced by combining STM with DFT simulations [174]. However, it has been not possible to directly visualize the O—H directionality and the associated chirality of water nanoclusters. We found that the tip-modulated orbital imaging technique also works for the water clusters.

Once the tip-water coupling is switched on, the water tetramers exhibit left-handed or right-handed rotation features, corresponding to the two different chiral states of tetramer (Fig. 10e, f and i, j). Upon increasing the tip-water coupling by decreasing the tip-water separation, surprisingly, each lobe of the tetramer appears as helical structures highlighted by curved dotted arrows (Fig. 10 g and k). Such helical structures resemble the HOMO of water molecule, which shows the same chiral character because of the tilt of the HOH plane from the surface normal (Fig. 10 h and l). Indeed, the calculated PDOS of water tetramer adsorbed on NaCl (001) suggests the broadening and shift of the HOMO towards E_F as a result of tip-water coupling, whereas the LUMO is less effected and stays above 1 eV [175].

Based on the submolecular-resolution orbital images, we are able to discriminate in real space the orientation of water monomers and the H-bonding directionality of water tetramers. This technique opens up the possibility of determining the detailed topology of H-bonded networks at water/solid interfaces with atomic precision, which was only possible through

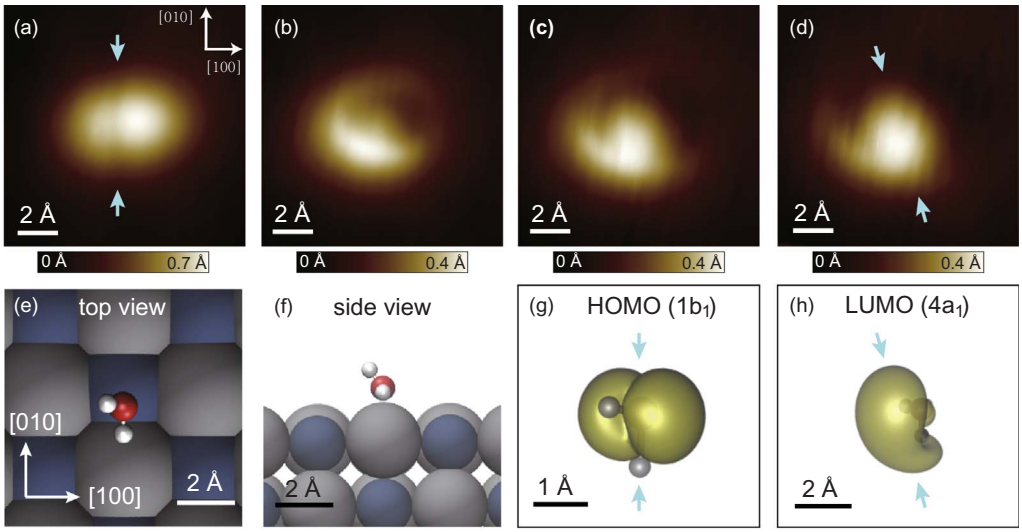

Fig. 6. Orbital imaging of an asymmetric water monomer adsorbed on the surface. (a–d) High-resolution STM images of HOMO (a), HOMO + LUMO (b and c), LUMO (d) of a water monomer. Set point: (a)10 mV, 100 pA; (b) −200 mV, 100 pA; (c) −250 mV, 100 pA; (d) −300 mV, 100 pA. (e, f) Top and side views, respectively, of the calculated adsorption configuration of an asymmetric water monomer. (g, h) Calculated isosurfaces of the charge density of HOMO and LUMO, respectively. The STM images were obtained at 5 K. Reproduced from Ref. [175] with permission.

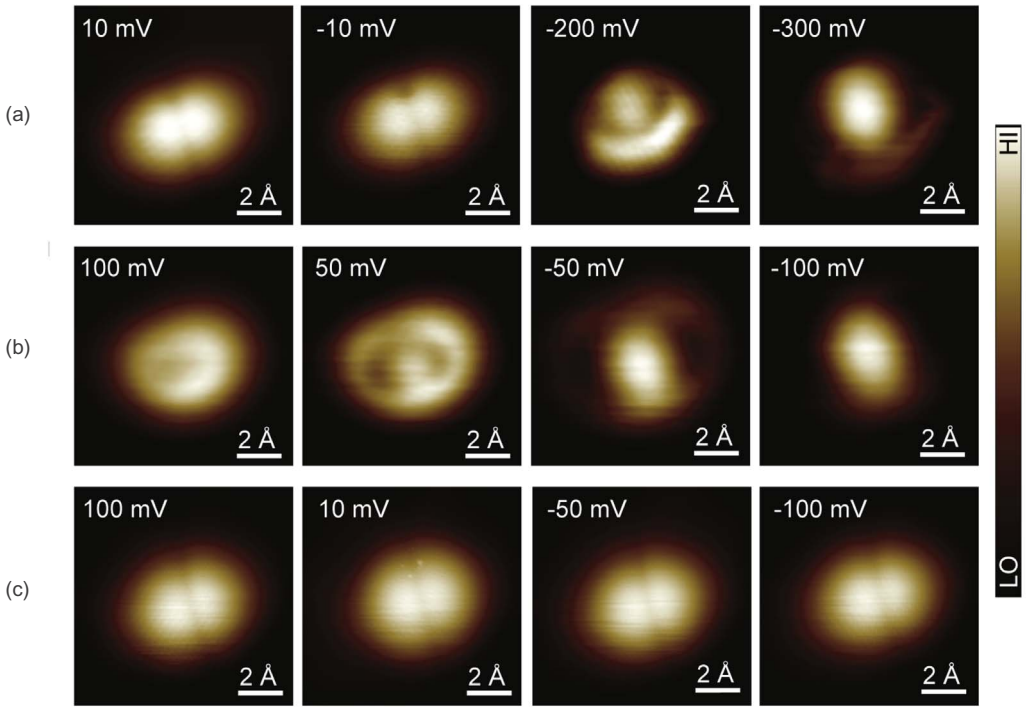

Fig. 7. Orbital imaging of different water monomers obtained with three different types of tip apex. The bias is inserted in the images and the tunneling current is 250 pA (a), 50 pA (b and c). Different tips show the selectively sensitivity to HOMO and LUMO. The STM images were obtained at 5 K. Reproduced from Ref. [175] with permission.

theoretical simulations in the past [154,155,160,169–171,176]. The ability to resolve the O—H directionality of water allows us to track the proton motion in real space, which provides further opportunities for probing the NQEs of protons at the atomic-scale such as correlated quantum tunneling of multiple protons in a water nanocluster [131], which will be discussed in Section 4. In addition, the tip-modulated orbital-imaging technique reveals new understanding of STM experiments and may be applicable to a broad range of molecular systems and materials.

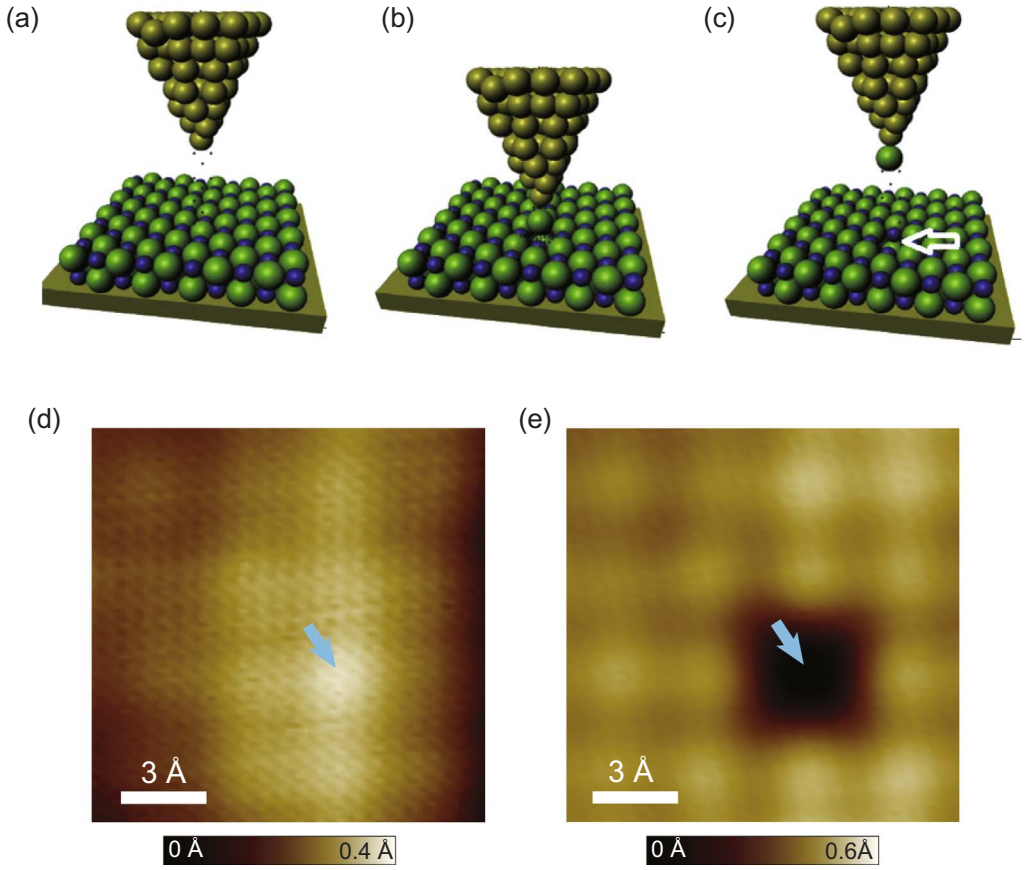

Fig. 8. Preparation of a Cl-functionalized tip. (a–c) The Cl-terminated tip was obtained by approaching a bare STM tip to the position of Cl atom of NaCl surface in close proximity (b) until a Cl atom transfers onto the apex of the STM tip (c). (d) STM image of the NaCl(001) surface acquired with a bare sharp STM tip. The atomic resolution arising from the Cl^- anions is resolved. The cyan arrow denotes the position where the STM tip is positioned. (e) STM image of the same area after the tip is retracted to the original set point. A Cl atom is missing (denoted by the cyan arrow) and the atomic resolution is improved, indicating that the STM tip is Cl-functionalized. Set point: (d) 50 mV, 100 pA; (e) 50 mV, 50 pA. The STM images were obtained at 5 K. Reproduced from Ref. [131] with permission. (For interpretation of the references to color in this figure legend, the reader is referred to the web version of this article.)

2.1.5. Growth and structure of larger water nanoclusters and 2D ice

When water molecules are dosed on the Au-supported NaCl(001) films at 77 K, they diffuse quickly and aggregate to form some water nanoclusters of different sizes. We found four typical types of water clusters with regular shape, denoted as I, II, III and IV in Fig. 11. In addition, larger water clusters with irregular shapes were also observed [177]. In order to identify the structure of these nanoclusters, we performed high-resolution STM imaging and *ab initio* DFT calculations.

Fig. 11 shows the high-resolution STM images and the calculated adsorption configurations of the four types of water clusters. The type-I water cluster corresponds to a water tetramer, which is the same as the one constructed at 5 K. The water tetramer is the most frequently discovered cluster on the surface and acts as the basic building block to form larger water clusters. The STM images of type-II, -III and -IV water clusters exhibit interesting bilayer structures, in which the tetramers in the lower layers are connected by bridging water molecules in the upper layers. Such a bridging mechanism was confirmed by the DFT calculations [177]. The type-IV water cluster consists of four tetramers, which are interconnected by six bridging water molecules, four at the periphery and two in the center (Fig. 11d). Interestingly, the pair of inner bridging water molecules results in the formation of a Bjerrum D-type defect [178,179], where there are two protons between the nearest neighbor oxygen atoms, but they avoid facing each other due to the repulsive interactions between the two upward H atoms. Such Bjerrum D-type defects have also been observed in water-hydroxyl layers on Cu(110) [179,180]. The other OH bond of each bridging water molecule points downward, forming H bond with the Cl^- anion so that the Cl^- is lifted by $\sim$0.5 Å from the NaCl surface.

With increasing water coverage, water molecules will eventually wet the NaCl(001) surface and form large-scale 2D ice islands via the bridging mechanism (Fig. 12a). The magnified STM image of 2D ice appears as an array of paired protrusions with two orthogonal orientations, one of which is denoted by a dashed white ellipse (Fig. 12b). As an extension of type-IV cluster, the 2D ice overlayer shows tetragonal bilayer structure, where the tetramer arrays in the lower layer are interconnected by paired bridging water molecules within the upper layer, giving rise to a large density of Bjerrum-D type defects (Fig. 12c). Those Bjerrum-D type defects provide a large number of dangling OH bonds, facilitating the nucleation of second-layer ice highlighted by cyan arrows in Fig. 12a.

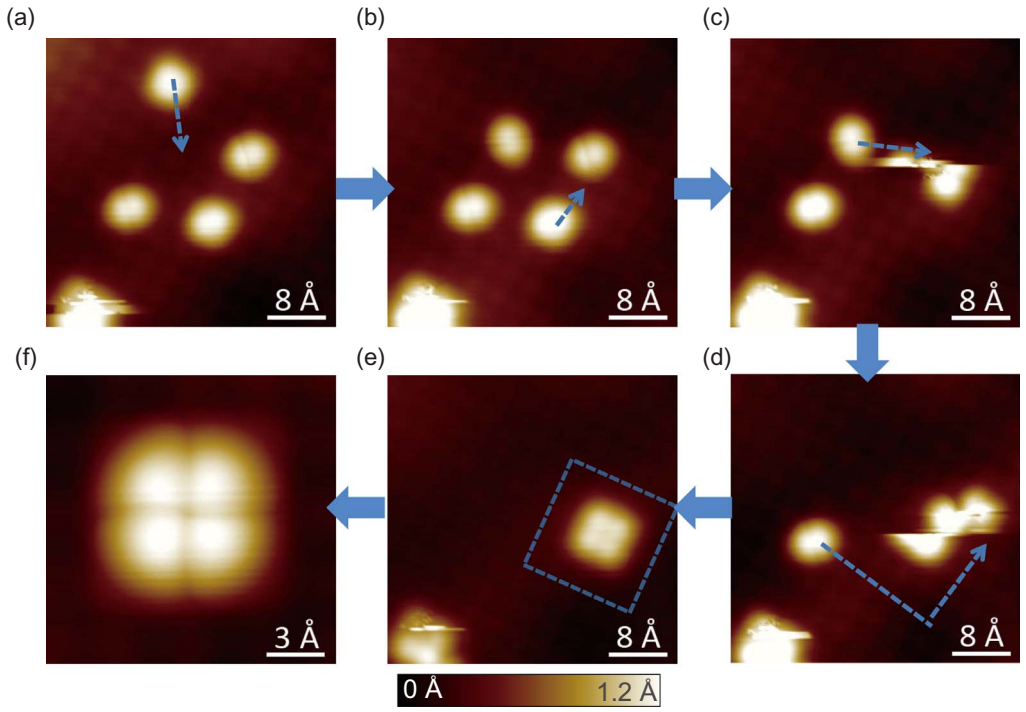

Fig. 9. Construction procedure of a water tetramer with the Cl-terminated tip. Water monomers were manipulated by the tip along the trajectories highlighted by the blue dashed arrows in (a–d). (e) The formation of a water tetramer. Set point of (a–e): 80 mV, 50 pA, 5 K. (f) Zoom-in STM image of the constructed water tetramer. Set point: 20 mV, 80 pA, 5 K. Reproduced from Ref. [175] with permission. (For interpretation of the references to color in this figure legend, the reader is referred to the web version of this article.)

Such a tetragonal bilayer ice structure built from cyclic water tetramers goes well beyond the conventionally simple hexagonal bilayer model. Recently, similar square ice structure was also observed between the layers of graphene bilayer due to the hydrophobic confinement [59]. Notably, the formation of the periodic Bjerrum-D type defects with unusually high density in the 2D ice strongly violates the Bernal-Fowler-Pauling ice rules [181] and may play a crucial role in catalyzing heterogeneous chemical reactions on water-coated salt surfaces as well as in influencing various phenomena such as heterogeneous ice nucleation, salt dissolution and caking.

2.2. Single-molecule vibrational spectroscopy of interfacial water

2.2.1. Background

Vibrational spectroscopy has long been employed to characterize the intramolecular and intermolecular interactions of water [152,182–188], providing a sensitive probe for NQEs of protons in energy space through isotope substitution experiments. Laser-based techniques, such as infrared and Raman spectroscopy have been used to characterize the NQEs of water in gas and condensed phases [28,36,185]. As a kind of nonlinear laser spectroscopy, SFG, provides a unique tool to probe NQEs of interfacial water at the molecular level [126]. In spite of the compatibility to a wide range of environments, these laser-based vibrational spectroscopies also suffer from the disadvantages of poor spatial resolution and spectral broadening, thus prohibiting the accurate and quantitative description of the NQEs.

On the other hand, electron spectroscopy could probe molecular vibrations as well via electron-vibration coupling, for example, electron energy loss spectroscopy (EELS) and inelastic electron tunneling spectroscopy (IETS). IETS was first demonstrated fifty years ago by Jaklevic and Lambe in metal-metal oxide-metal junctions [189], in which some of the tunneling electrons interact with vibrations of the molecules at the interface and become inelastic tunneling electrons. Such inelastic processes open a new conductance channel, leading to the change in differential conductance. The vibrational fingerprint can be magnified as prominent peak and dip that are point-symmetric with respect to the zero bias in the second derivative of current to the bias voltage (d^2I/dV^2). In 1988, Stipe et al. pushed the sensitivity of IETS down to single- molecule level using STM [140]. Most of STM-IETS measurements have been performed on molecules whose frontier orbitals are located far away from the E_F [151,190,191]. In such off-resonance cases, the electron-vibration coupling is just a weak perturbation on the elastic scattering picture, leading to a very small cross section for the vibration excitation and weak IET signals with the differential conductance change of a few percent [192,193].

This limitation is particularly true for close-shell molecules like water. Consequently, vibrational spectroscopy of interfacial water by STM has been rarely reported. Morgenstern et al. demonstrated the first IETS of water submonolayer on Ag(111) and assigned the IET features to various vibrational modes of the water molecule [194]. However, the IET signals were too weak to identify the

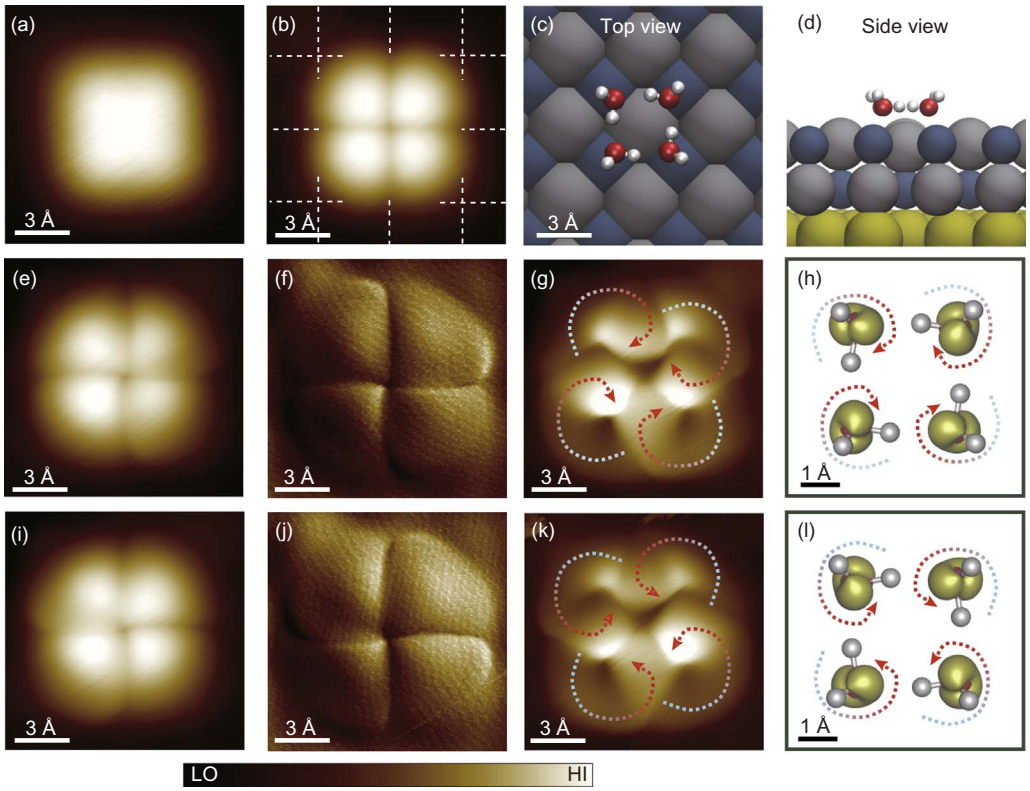

Fig. 10. Orbital imaging of water tetramers on NaCl(001)/Au(111) surface. (a, b) STM images of a water tetramer acquired at different tunneling gaps. The white square grid in (b) denotes the sub-lattice of Cl^-. (c, d) Top (c) and side (d) views of the calculated adsorption structure of a tetramer. (e–l) HOMO imaging of a water tetramer with two different chiral states, anticlockwise (e–h) and clockwise (i–l) H-bonded loops. (e, i) STM images of water tetramer. The four lobes are no longer equivalent and the boundaries between the four lobes exhibit left-handed (e) or right-handed (i) rotation, which is more evident in the corresponding derivative images (f and j). (g, k) STM images of the water tetramers with enhanced tip-water coupling. The lobes of the water tetramers shown in (e) and (i) are resolved into helical structures as highlighted by curved dotted arrows with gradient (high: red, low: cyan). (h, l) Calculated HOMO of the two chiral tetramers by plotting isosurfaces of charge densities integrated over 1 eV of the HOMO tail close to E_F. The chirality of the HOMO resembles that of the helical structures as shown in (g) and (k). Set point of the STM images: (a) 40 mV, 10 pA; (b) 10 mV, 50 pA; (e and i) 10 mV, 80 pA; (g and k)10 mV, 140 pA. The STM images were obtained at 5 K. Reproduced from Ref. [175] with permission.

vibrational modes accurately because of the wide HOMO-LUMO gap of water molecules. In addition, Kumagai et al. obtained IET spectra of the hydroxyl group and its clusters, which were constructed in a controlled way by STM tip manipulation [14,15,195]. These spectra enabled the precise identification of OH/OD bending and stretching modes. However, the apparent vibrational features in the IET spectra mainly arose from the interchange motion between different structures of hydroxyl species. Hence, it has been very difficult to obtain reliable vibrational spectroscopy of water with conventional IETS.

Persson and Baratoff theoretically predicted in 1987 that a differential conductance change of 10% or more could be achieved in IETS when a molecular resonance happens to be within the bias window of IET process [196]. In such a case, the tunneling electrons interact strongly with the molecular vibration, termed as resonantly enhanced IETS [196]. In 2009, the resonantly-enhanced IETS was experimentally realized by Song et al. in a three-terminal single-molecule device by tuning the location of HOMO with respect to the E_F via voltage gating [197]. In a similar way, we show the possibility of gating the frontier orbitals of a water monomer on NaCl (001) surface with a functionalized STM tip through tip-molecule coupling. The signal-to-noise ratio of the tip-enhanced IETS [132] is increased by orders of magnitude over the conventional STM-IETS.

2.2.2. *Methods*

The STM measurements were all performed at 5 K. The scanning tunneling spectroscopy, dI/dV and d^2I/dV^2 spectra, were acquired simultaneously using a lock-in amplifier by demodulating the first and second harmonics of the tunneling current, respectively. A modulation voltage of 5–7 mV_{rms} at 237 Hz was added with the feedback loop open.

To understand the IETS signal theoretically, one needs to study the electronic transport problem taking into account electron's interaction with molecular vibrations. The experimental IETS of water monomer is analyzed with the transport calculations based on DFT in combination with nonequilibrium Green's functions developed in Ref. [198]. We calculate the electronic structure using SIESTA [199], transport properties using TranSIESTA [200], and electron-vibration coupling and IETS using Inelastica [201].

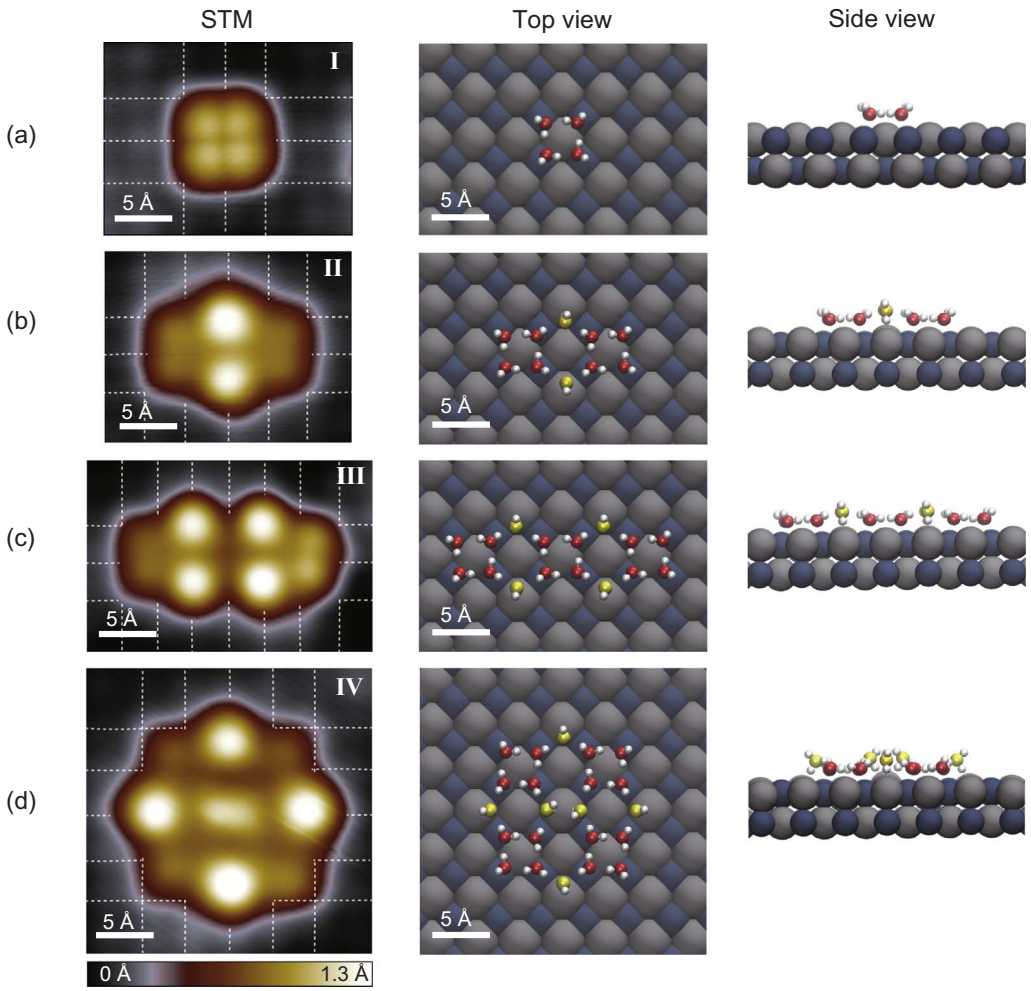

Fig. 11. High-resolution STM images and schematic models of four types of water clusters. (a) Type-I; (b) type-II; (c) type-III; and (d) type-IV. The first column is the STM topographies of the water nanoclusters acquired at 5 K. The white square grid denotes the sub-lattice of Cl^-. The second the third columns are the top and side views of the calculated adsorption configurations of the water clusters, respectively. H, Cl^- and Na^+ are denoted by white, gray and dark-cyan spheres, respectively. The O atoms of water molecules in upper layers are represented by yellow spheres and the lower layers are red spheres. Set point (a) 20 mV, 50 pA; (b) 7 mV, 550 pA; (c) 6 mV, 400 pA; (d) 5 mV, 120 pA. The STM images were obtained at 5 K. Reproduced from Ref. [177] with permission.

2.2.3. Selective orbital gating of water monomers with a Cl-tip

As shown in the schematic of the experimental setup (Fig. 13a), we measured the IETS of water monomer (D_2O) adsorbed on the Au-supported NaCl(001) surface. The DOD plane of the D_2O monomer is perpendicular to the surface with one OD dangling upward, the other OD forming a H bond with the Cl^- of the NaCl surface [175]. As discussed in Section 2.1, the STM tip not only acts as a probe, but also could modify the molecular DOS around the E_F via tip-molecule electronic coupling. This actually offers a viable way to tune the off-resonance IET process into near-resonance case.

However, we noticed that the terminations of the bare STM tips are usually uncontrollable, which will influence the gating efficiency of different molecular orbitals [175]. In order to obtain reliable IET spectra in a well-controlled fashion, we functionalized the tip apex with a Cl atom. We found that the Cl-terminated tip can selectively enhance the HOMO states around E_F (Fig. 13b), while the LUMO is less affected. Compared to the bare metal tip, the orbital gating with a Cl-tip is more efficient because of the strong coupling between the HOMO with the Cl p_z orbital. The STM images of water monomers acquired with a Cl-tip always exhibited a HOMO-like double-lobe structure with a nodal plane in between (Fig. 13d), while the LUMO was not observed throughout the accessible bias range (from -400 mV to 400 mV). In such a near-resonance case (Fig. 13c), the electron-vibration interaction is resonantly enhanced, leading to the increase of IET cross section. Considering the key role of tip gating in enhancing the IET signals, we named this technique as tip-enhanced IETS.

2.2.4. Tip-enhanced IETS of D_2O monomers

Fig. 14 is the typical tip-enhanced IETS of the D_2O monomer on the Au-supported bilayer NaCl(001) surface. At large tip height, the spectra are featureless (blue curves), simply following the background NaCl signal. When approaching the tip by 80 pm toward

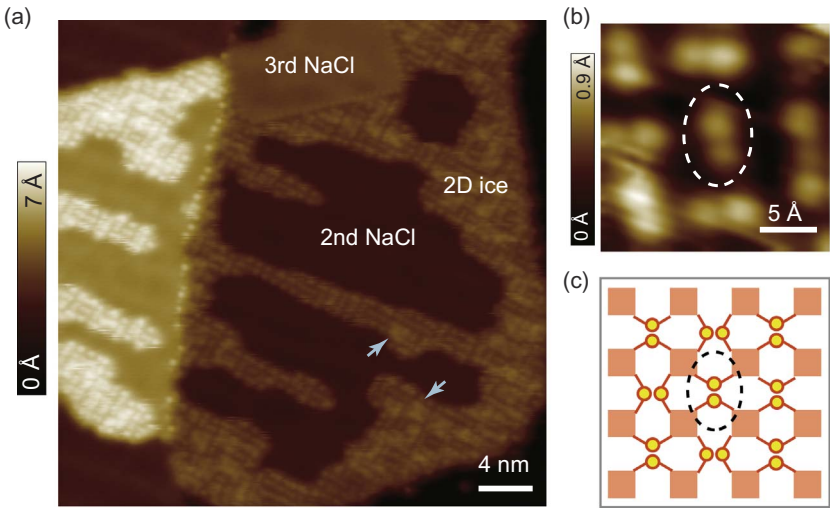

Fig. 12. The formation of 2D tetragonal bilayer ice on the NaCl(001) surface. (a) STM image of the 2D ice on a NaCl island. Additional water molecules adsorbed on the 2D ice islands, highlighted by the cyan arrows. (b) Zoom-in STM image of 2D ice. (c) Schematic model of the 2D tetragonal bilayer ice, corresponding to (b). The red solid squares denote the water tetramers and the yellow spheres denote the bridging water molecules. The dashed white and black ellipses in b and c highlight one of the Bjerrum D-type defect. Set point: (a) 400 mV, 10 pA; (b) 350 mV, 10 pA. The STM images were acquired at 77 K. Reproduced from Ref. [177] with permission.

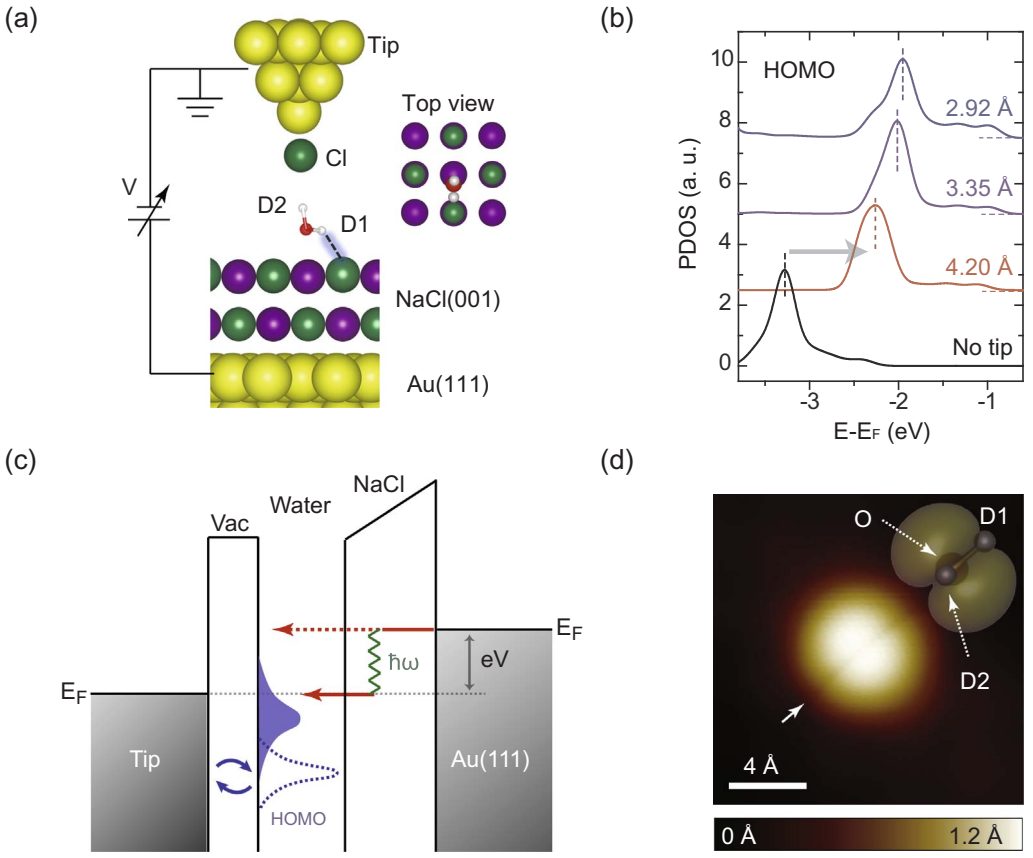

Fig. 13. Orbital gating of a water monomer via tip-water coupling with a Cl-tip. (a) Schematic of the experimental setup. Water monomer adsorbed on the Au-supported NaCl(001) surface with a "standing" configuration with a dangling OD (D2) and a H-bonded OD (D1, denoted by dashed line). O, D, Au, Cl^-, and Na^+ are denoted by red, white, golden, green, and purple spheres, respectively. (b) Calculated PDOS of water monomer with and without STM tip. The peaks of these curves denote the HOMO states of water monomer. The position the peaks are highlighted by dashes lines. HOMO moves towards the E_F when the tip appears (gray arrow). (c) Schematic of the tip-enhanced IET process. The tip-water coupling tunes the HOMO to the proximity of the E_F, leading to resonantly-enhanced IETS. (d) STM image of water monomer acquired with a Cl-terminated tip at V = 100 mV, I = 50 pA, resembles the calculated isosurface of charge density of the HOMO (inset). Reproduced from Ref. [132] with permission. (For interpretation of the references to color in this figure legend, the reader is referred to the web version of this article.)

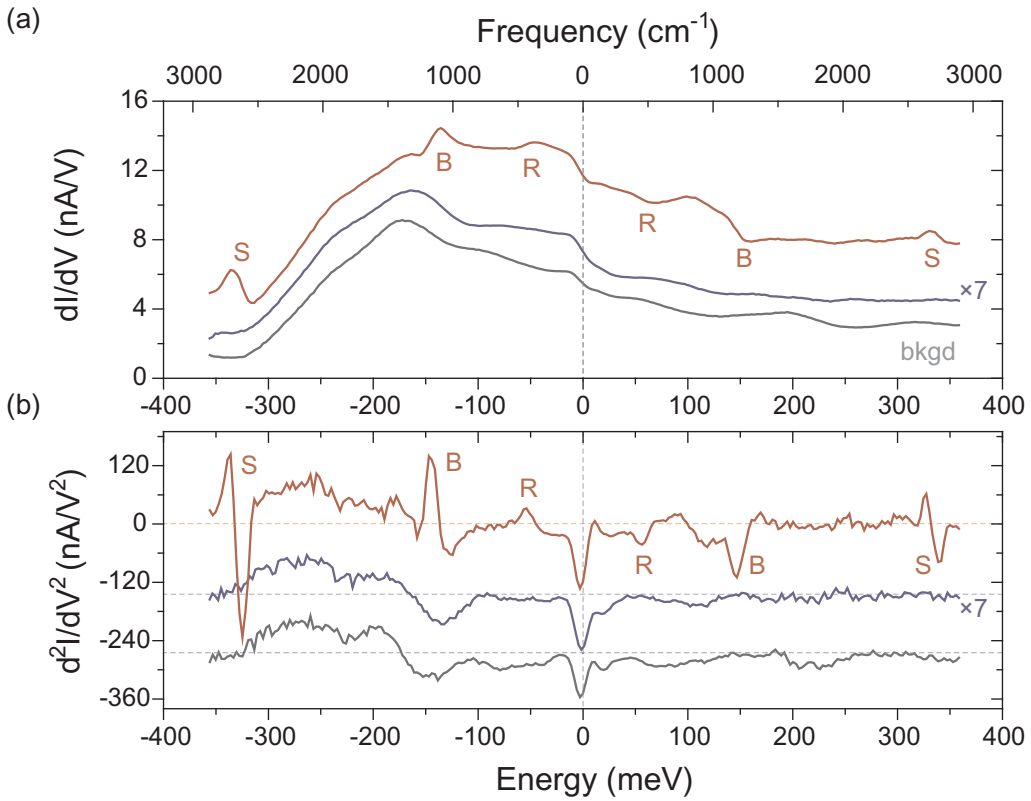

Fig. 14. Tip-enhanced IETS of a D_2O monomer. (a) dI/dV (b) d^2I/dV^2 spectra obtained at different tip heights. Red and blue curves are taken on the water monomer with the tip height offset of −120 pm and −40 pm, respectively. Gray curve is the background NaCl signal acquired at the tip height offset of −120 pm. Tip heights in the experiment in this section are referenced to the gap set with V = 100 mV and I = 50 pA. "R", "B", "S" represent water rotational, bending and stretching vibration mode, respectively. These curves are offset presented in the y axes for clarity and the zero levels of each curve are denoted by the dashed horizontal lines. Reproduced from Ref. [132] with permission.

the water molecule, additional kinks emerge in the dI/dV spectrum (red). These features are more prominent in the corresponding d^2I/dV^2 spectrum and appear as peaks and dips in point symmetry with respect to the zero bias. According to the calculated vibrational modes of a water monomer adsorbed on the NaCl (001) surface, we assigned the spectral features to the frustrated rotational ("R"), bending ("B"), and stretching mode ("S"), respectively [132]. The experimental (calculated) energies of those vibrational modes are: "R" 55 meV (40 meV), "B" 147 meV (140 meV), "S" 326 meV (310 meV).

We found that the IETS of water molecules is very sensitive to the tip position on the water monomer, as shown in Fig. 15. When the tip was positioned on the nodal plane (black dot), the IET spectrum only shows rather weak vibrational features (black curve). On the one hand, the molecular DOS is the smallest at the nodal plane, resulting in a very small cross section for vibration excitation in the IET process. On the other hand, the coupling between the HOMO and Cl p_z orbital will be enhanced upon moving the tip a little bit away from the nodal plane due to their opposite symmetry. In addition, the tip-enhanced IETS is also sensitive to the nature of the tip apex (Fig. 16). Different tip terminations may selectively gate different molecular orbitals (with different symmetries) to E_F. According to the IETS propensity rules [202,203], only the vibrational modes whose symmetry match those of the molecular orbitals around E_F are detectable in the tip-enhanced IETS.

In addition, the tip-water coupling may have significant influence on the intrinsic energies of the vibrational modes. Indeed, we found that the stretching modes will red shift with decreasing tip height and can be fitted by inversed exponential functions (Fig. 17). Extrapolating these curves to infinite tip height allows us to eliminate the tip effect. The resulting energies of D2, D1 and H1 stretching modes are 338.7 ± 0.3, 326.8 ± 0.5 and 446 ± 0.4 meV, respectively (for detail discussions about D2/D1 modes, see Section 5.2). The redshifts or softening of those vibrational modes suggest the increased H-bonding interaction between the tip (the NaCl substrate) and the water monomer (for details, see Section 5.3).

2.2.5. Lineshape of tip-enhanced IETS

Fig. 18a is the high-resolution IETS at different tip-molecule distances. With decreasing tip height, the intensity of the normalized IET feature is enhanced by more than one order of magnitude. Meanwhile, the line shape changes gradually from a symmetric dip to an asymmetric Fano-like shape [204]. In order to understand the underlying physical picture of the apparent two features, we simulated the IETS of a D_2O monomer at different tip heights using the DFT-based transport theory [198,200] (Fig. 18b), which is in excellent agreement with the experimental data.

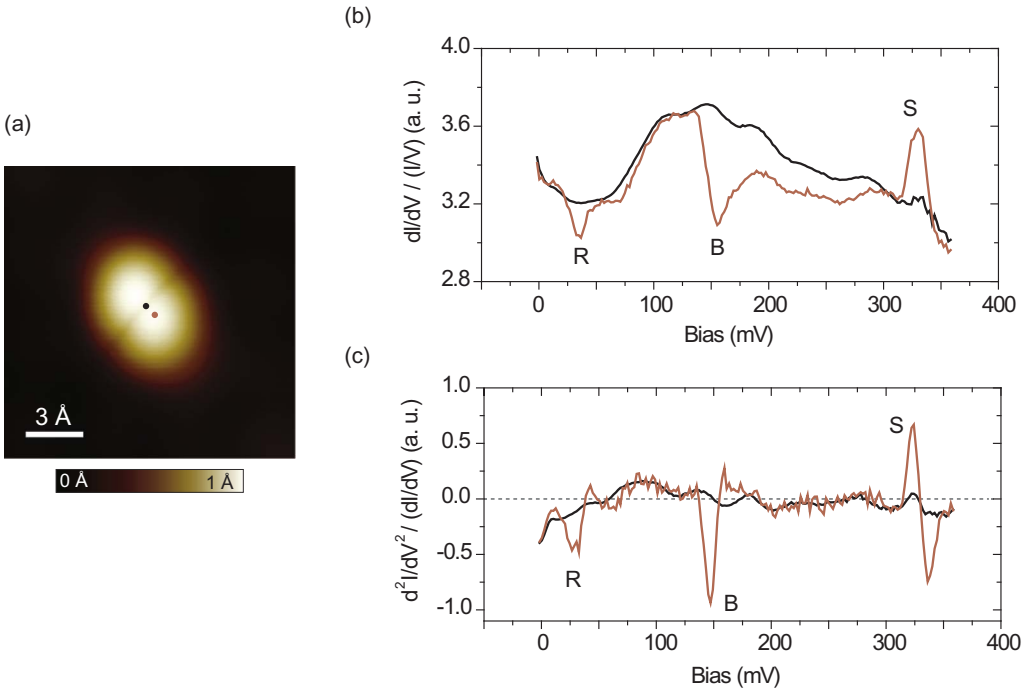

Fig. 15. Site-dependent IETS of a D_2O monomer. (a) STM image of a water monomer. Set point: V = 100 mV, I = 50 pA. (b) dI/dV (c) d^2I/dV^2 spectra obtained at different sites. The black (red) curves in (b) and (c) correspond to the tip positions of black (red) dots in (a). Reproduced from Ref. [132] with permission. (For interpretation of the references to color in this figure legend, the reader is referred to the web version of this article.)

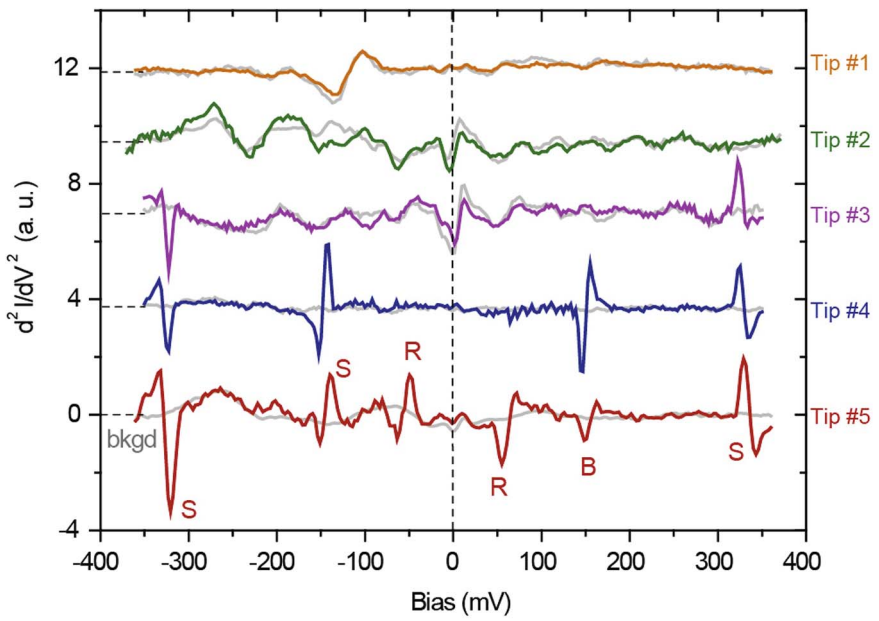

Fig. 16. Selective enhancement of vibrational modes by tip-enhanced IETS. IETS of a D_2O monomer acquired with different types of tips, showing that the tip-enhanced IETS is very sensitive to the nature of tip apex. Tip #1 is sensitive to both the HOMO and HOMO-1. Tip #2 is sensitive to none of the orbitals. Tips #3–5 are all sensitive to the HOMO, but with different resolution. The different vibrational modes of the D_2O monomer are denoted as "R" (rotational), "B" (bending), and "S"(stretching). Gray curves were acquired on the NaCl surface (denoted as "bkgd"). Reproduced from Ref. [132] with permission.

Detailed analysis indicates that both inelastic and new high-order elastic channels become open and determine the lineshape and spectral intensity of IETS signal. Inelastic process (Fig. 19c) opens an additional transport channel, and contributes to a peak in the d^2I/dV^2 signal for positive bias. In contrast, the two high-order elastic processes (Fig. 19a and b) may contribute to a dip due to their interference with the zero-order elastic tunneling. In the near-resonance case, the high-order elastic processes become more

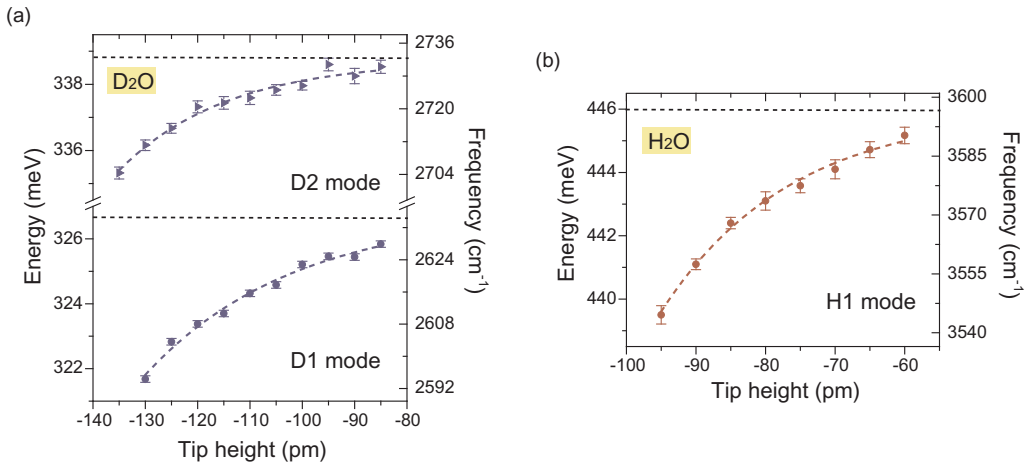

Fig. 17. Extraction of the intrinsic vibrational energies of stretching modes of water monomers. Energies of D1, D2 (a) and H1 (b) stretching modes as a function of tip height. Each group of data is fitted to an inversed exponential decay. Extrapolating these curves to infinite tip height allows us to obtain the intrinsic energies (dashed lines) without the influence of the tip. Tip heights are referenced to the gap set with V = 100 mV and I = 50 pA. Reproduced from Ref. [132] with permission.

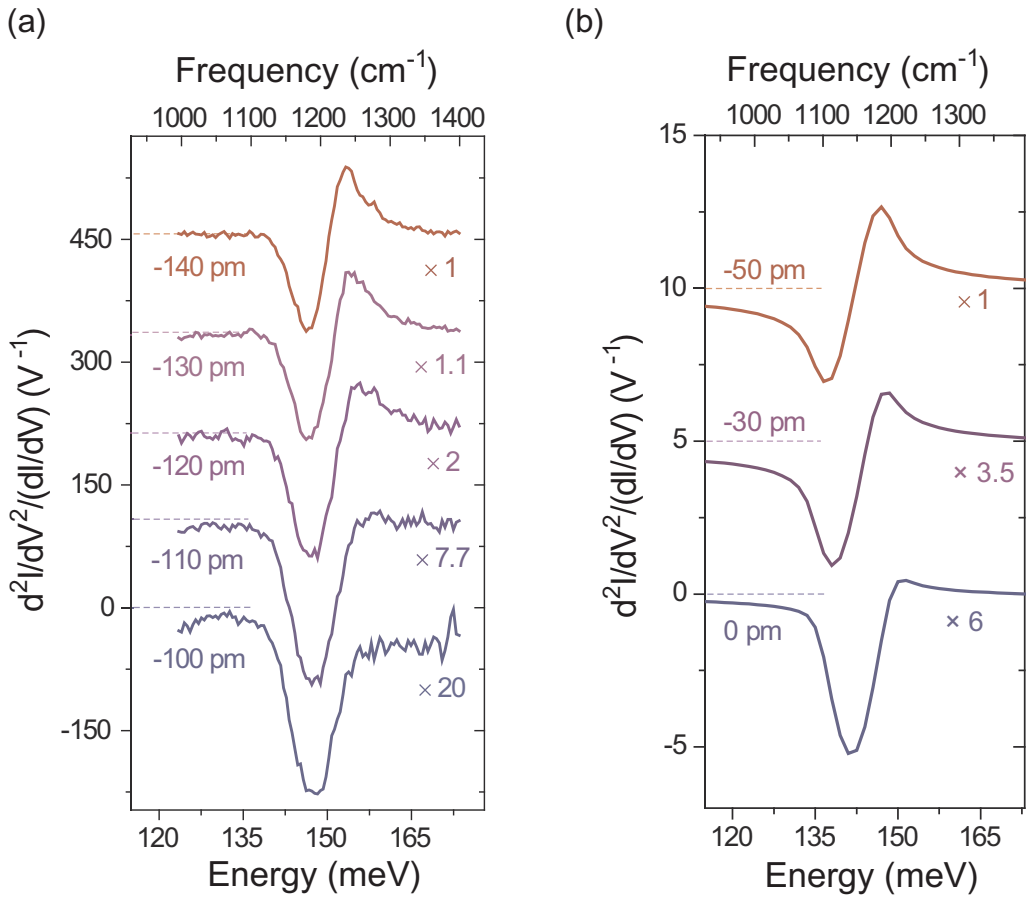

Fig. 18. Tip-enhanced IETS of bending mode of a water monomer. Experimental (a) and calculated (b) d^2I/dV^2 spectra (normalized by dI/dV) of the bending mode as a function of tip height. For clarity, each curve is scaled properly to ensure the same magnitude. Tip heights are referenced to the gap set with V = 100 mV and I = 50 pA. The tip height in calculation is defined as the vertical distance between the Cl atom at the tip apex and O atom of the water molecule. Reproduced from Ref. [132] with permission.

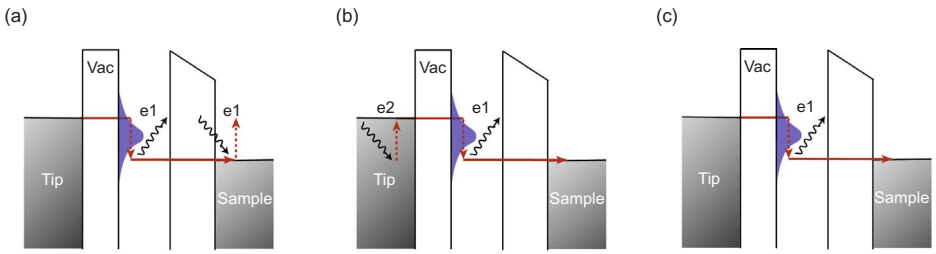

Fig. 19. Tunneling processes involved at the threshold bias and contributing to IETS. (a) One-electron elastic process: One electron makes an inelastic transition downward from the left to the right electrode, emitting a vibration; the same electron re-absorbs this vibration and makes an inelastic transition upward at the right electrode. (b) Two-electron elastic process: One electron tunnels inelastically from the left to the right electrode, emitting a vibration; a second electron makes an inelastic transition upward at the left electrode, re-absorbing the emitted vibration. (c) One-electron inelastic transition from the left to the right electrode. In our case, the molecular resonance couples stronger to the tip, so the process (b) is enhanced. Reproduced from Ref. [132] with permission.

prominent than the inelastic process, resulting in the dip feature. The observed dramatic increase of the spectral intensity arises from the enhanced HOMO DOS with decreasing tip-molecule separation. On the other hand, the elastic processes (Fig. 19a and b) also contribute to the asymmetric lineshape. But their contributions are opposite to each other and normally cancel out. Considering that the resonant state (HOMO) of water couples more strongly to the tip, the process e2 in the elastic process (Fig. 19b) should be enhanced and dominate over the other elastic channel, leading to the symmetric-to-asymmetric line shape change with decreasing tip height [196,198,205].

It is worth noting that the relative conductance change in the tip-enhanced IETS could be as high as 30%, such that a high signal-to-noise ratio of the IETS signal facilitates the accurate determination of the H-bonding strength, which is related to the redshift of the D1 stretching mode [206]. Therefore, developing the tip-enhanced IETS is a crucial step for us to probe the NQEs of H-bonding strength, which will be discussed in details in Section 5.

Although the intensity of IETS signal has been enhanced through the tip-enhanced techniques, it is still in the weak electron-vibration (e-vib) interaction regime as the lifetime of the tunneling electron in the water molecule is very short due to the strong tip-water coupling. Otherwise, for strong e-vib interaction, we expect much stronger signal or vibrational satellite peaks showing up, which is absent in our measurements.

3. Recent developments of *ab initio* PIMD and applications to surface water

In the above sections, we have summarized the recent advances of STM/S measurements on surface water, especially the ability of accessing the degree of freedom of protons. Now we turn to the theoretical part of this review. Developments of the first-principle methods mean that nowadays many of the experimental measurements can be understood in detail. These methods include STM imaging [207], surface and adsorption energy calculations [208], finite-temperature MD [209], and transition state searching [210], etc. In our studies, we have resorted to these methods for the understanding of the experimental observations [131,132,175,177]. A thorough description of these methods is a demanding task and clearly beyond the scope of this review. We refer the readers to Refs. [207–210] for details of this wide range of methods. In other sections of this review, the theoretical results have been discussed together with the experimental observation for the completeness of each story. Since the quantum nature of surface water is the specific problem we emphasize in this review, in this section, we focus on one method for the descriptions of the quantum nature of the H bonds in interfacial water, i.e. *ab initio* PIMD. We will summarize its developments for the simulations of realistic polyatomic systems starting from the early 1980s, its application to the understanding of the quantum nature of H bonds, and its recent applications to the simulations of surface water, separately.

3.1. Recent developments of the ab initio PIMD method

In a realistic molecule as well as in condensed matter, the system we want to simulate is a many-body entity composed of many electrons and many nuclei. In descriptions of the nuclei, when the classical approximation does not work, a natural choice is to construct a high-dimensional PES and solve the Schrödinger equation for the many-body entity of the nuclei. In so doing, the statistical and dynamical properties of the nuclei can be described very accurately at the quantum mechanical level. In the last ~20 years, this method has been very successfully applied to the studies of simple gas-phase reactions [82–84]. Because of the scaling problem in constructing the high-dimensional PES and solving the Schrödinger equation, the targeting problems are normally restricted to very small systems. In larger molecules and condensed matter, an alternative practical method is required.

Such a practical scheme can be provided by R.P. Feynman's path-integral representation of quantum mechanics [85]. Using finite-temperature sampling techniques like MD or Monte-Carlo (MC), a series of path-integral simulations had been carried out in the 1980s for the description of the nuclear quantum effects (NQEs) in condensed matter and molecular systems [86–90,92]. One feature in common in these simulations is that the interatomic potentials were modelled using force-fields. As a consequence, many interesting processes involving chemical bond breaking/forming could not be addressed. In the 1990s, using Car-Parrinello MD, these path-integral based simulations started to tackle these problems in an *on-the-fly* manner. Many interesting phenomena have been found [30,31,91], in which NQEs in terms of zero-point energy and quantum tunneling played a crucial role. After 2000, these path-

integral simulations have been further extended to rigorous Born-Oppenheimer MD/MC [45,93,98,100,101]. These *ab initio* PIMD simulations were normally done using electronic structures calculated on-the-fly with standard local or semi-local functionals within the density-functional theory. There exist problems when the so-called delocalization error of the electrons are serious [211]. In such cases, it is necessary to resort to more complicated functionals like the hybrid one, or the quantum chemistry methods. Recently, PIMD simulations based on quantum chemistry methods like MP2 were reported [95,96]. This new choice of the electronic structures provides a more flexible recipe in dealing with systems when standard local or semi-local functionals do not work. Most recently, methods like thermodynamic integration (TI) were further combined with *ab initio* PIMD for the calculation of the free-energies [94,97,99,102]. All these developments provide the tools to perform more practical simulations of the NQEs in realistic systems, accurately.

3.2. The principles of path-integral simulations

Using electronic structures calculated *on-the-fly*, *ab initio* PIMD method relies crucially on the treatment of temperature as an imaginary time and the representation of the quantum mechanical nuclear density matrix in terms of a fictitious polymer [91], through:

$$\rho(x_0,x_P,\beta) = \lim_{P\to\infty}\left[\prod_{j=1}^{N}\left(\frac{m_j P}{2\beta\pi\hbar^2}\right)^{P/2}\right]\times\int_V\int_V\cdots\int_V exp\left\{-\beta\sum_{i=1}^{N}\frac{1}{2}m_j\omega_P^2(x_i^j-x_{i-1}^j)^2 + \frac{1}{2P}(V(x_i^1,\ldots,x_i^N)+V(x_{i-1}^1,\ldots,x_{i-1}^N))\right\}dx_1dx_2,\ldots,dx_{P-1} \tag{1}$$

Here, m_j is the mass of the j-th nucleus; $\beta = 1/(k_BT)$, with k_B meaning the Boltzmann constant, and T is the temperature. P is the number of replicas in the fictitious polymer, *i.e.* the number of sampling points for the imaginary time path-integral. This replica is also called an image or a bead. The beads are coupled to each other by nearest neighbor harmonic interactions with the spring constants defined as $m_j\omega_P^2$ where $\omega_P = \sqrt{P}/(\beta\hbar)$. x_i means the spatial configuration of the nuclei on the i-th bead of the fictitious polymer, and x_i^j represents the position of the j-th atom in the i-th bead. Each bead is subjected to a potential, defined by $V(x_i^1,\ldots,x_i^N)$, obtained from the *ab initio* calculations.

In Eq. (1), if we take $x_0 = x_P$, the density matrix evolves into its diagonal part, *i.e.* the quantum density function. The partition function of the quantum system can be further obtained from:

$$Z^Q = \lim_{P\to 0}\left[\prod_{j=1}^{N}\left(\frac{m_j P}{2\beta\pi\hbar^2}\right)^{\frac{P}{2}}\right]\times\int_V\int_V\cdots\int_V e^{-\beta V^{\text{eff}}(x_i^1,\ldots,x_i^N)}dx_1dx_2,\ldots,dx_P \tag{2}$$

with V^{eff} defined as:

$$V^{\text{eff}}(x_i^1,\ldots,x_i^N) = \sum_{i=1}^{P}\sum_{j=1}^{N}\frac{1}{2}m_j\omega_P^2(x_i^j-x_{i-1}^j)^2 + \sum_{i=1}^{P}\frac{1}{P}V(x_i^1,\ldots,x_i^N) \tag{3}$$

In so doing, all quantum statistical properties of a quantum system can be obtained. Pictorially, this can be understood by the mapping between the quantum system and the polymer as shown in Fig. 20. When $P = 1$, the system is purely classical, but when P becomes infinite, Eq. (2) rigorously reaches the quantum limit.

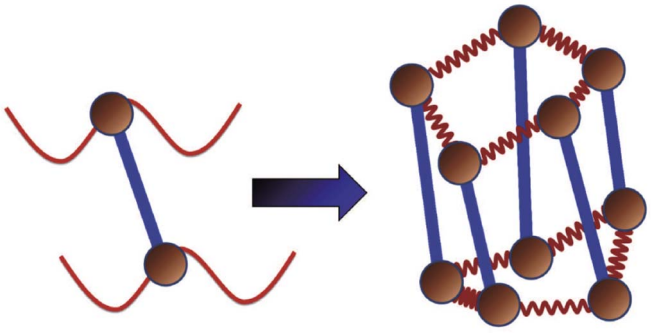

Fig. 20. Illustration of how the quantum system is mapped to a polymer in the path-integral simulations. molecule is taken as the example. What one does in the simulation is to construct an artificial polymer, which is composed by P beads of the real molecule. In each bead, the potential is determined by the potential of the molecule at the specific spatial configuration of this bead. In between the beads, the neighboring images (beads) of the same atoms are linked by springs.

3.3. Application to NQEs in H-bonded systems

Starting from the 1950s, it has been known that replacing H by D in H-bonded molecular crystals can result in noticeable changes of the lattice constants [212]. This phenomenon is called the Ubbelohde effect [213]. The implication is that nuclear statistical effects in the quantum limit also impact on the intermolecular interactions. This leads to a substantial improvement over the traditional "ball-and-stick" model in descriptions of chemical bonding interactions [81]. From the theoretical perspective, ever since the path-integral based methods were used to study the NQEs in realistic poly-atomic systems, the question concerning how NQEs impact on the strength of H-bonds in large molecular systems and condensed matter had been a subject of intense research [7,29,31,32,63,64,98,103–111]. For smaller water clusters, alternative quantum mechanical methods for the descriptions of the intermolecular vibrations such as diffusion Monte Carlo (DMC) and second-order vibrational perturbation theory also played an important role to inject new insights into how the traditional "ball-and-stick" model could be improved to provide an accurate description of the finite-temperature intermolecular interactions [81,214].

At present, a picture based on the competition of the NQEs on the intramolecular covalent bond stretching and intermolecular H bond bending was often used to interpret the computer simulation results [7,32,98,110], and to rationalize the corresponding experiments [132]. In this picture, the NQEs on the intramolecular covalent bond stretching mode strengthen intermolecular interactions, in comparison with the classical "ball-and-stick" model results. The NQEs on the intermolecular bending modes, on the other hand, weaken such interactions compared with the classical results. The final influence of NQEs, therefore, depends on the competition between contributions from these different modes [98]. For typical weak H bonds, it is easier for the NQEs to bend the H bonds in comparison with the covalent bond stretching. As a consequence, the NQEs weaken the intermolecular H-bonding interactions. For typical strong H bonds, the NQEs on the stretching modes are often dominant. Consequently, NQEs strengthen intermolecular interactions. Recently, this physical picture has been experimentally confirmed by STM [132], which will be discussed in Section 5. Considering the fact that in classical statistics this competition between different vibrational modes also exists, in liquid water, raising the temperature by 30 K in comparison with the classical simulation at room temperature often gives a very accurate description for the influence of NQEs on structural properties [106]. In other H-bonded systems, this is not guaranteed.

3.4. Further applications to surface problems and surface water

A large part of the success of first-principle computer simulation methods can be reflected by their applications to surface science problems [207,208]. Among them, applications to surface water have made a great contribution. One early example is the prediction that water dissociates barrierlessly on Ru (0001) [215]. Motivated by this study, *ab initio* simulations have significantly improved our understanding of the behavior of water on metal surfaces over the last decades [146]. We note that these simulations have resorted to the "ball-and-stick" model for the description of the chemical bonding interactions. Due to the light mass of H and the quantum nature of H bonds, a fully quantum description of the structures and reactions of surface water becomes necessary.

One early effort to understand the influence of NQEs on the adsorption energy was done for a water molecule on MgO(001) at low coverage using path-integral simulations [216]. Roughly at the same time, by comparing the structures obtained from the *ab initio* PIMD simulations with those obtained from the *ab initio* MD simulations, delocalized H within the water-hydroxyl monolayer was also predicted on some transition metal surfaces [45]. Some of these theoretical results agree well with the available experimental observations [15]. However, due to experimental restrictions on the spatial and temporal resolution for the processes measured and the relatively large computational cost of the theoretical simulations, systematic studies on how NQEs impact on the geometry, adsorption energies, and dynamics of surface water systems are very scarce.

One problem which is related but not exactly the same is the behavior of H diffusion on transition metal surfaces. Starting from the earlier 1990s, comparatively speaking, this problem has been studied quite systematically [217–223]. Evolution of the kinetic constant as a function of inverse temperature gives a clear indication where the dynamics changes from classical hopping to quantum tunneling [217]. At a fixed temperature, isotope substation also gives some hints on how the NQEs impact on the dynamical process. We believe similar methods can be used to study problems concerning the diffusion and clustering of water molecules on surfaces. And more systematic theoretical and experimental studies on surface water are highly desired.

The recent advances in STM/S towards accessing the quantum degree of freedom of protons actually enable the direct and quantitative comparison with *ab initio* PIMD simulations. On the one hand, the results by STM/S set an atomic-scale reference for the *ab initio* PIMD method to test its validity. On the other hand, the perfect match between the two methods may help reveal the underlying mechanism of NQEs in a more decisive way. In the following two sections, we will discuss how the combination of STM/S and PIMD are used to attack two key issues of NQEs at a water/solid interface: concerted proton tunneling and anharmonic zero-point motion.

4. Concerted proton tunneling in water nanoclusters

4.1. Background

Proton tunneling is fundamental to many physical, chemical and biological processes [1,8,9,75,224–228]. In comparison with the well-studied single proton tunneling, many-body tunneling is more complicated but participates in much broader proton dynamic processes, for instance, the phase transition of ice [11,17,32], molecular tautomerization and enzyme catalysis reactions [66,67,70,71,133]. However, our understanding of multiple proton tunneling is far from complete. Since protons within a H-bonding

network are usually correlated [229], the proton tunneling may occur in a collective way. To date, some spectroscopic studies reported concerted proton tunneling in ices and H-bonded crystals [11,16,17], but the evidence is quite indirect and elusive. In addition, the correlated tunneling of protons is very sensitive to the local environment due to the demanding requirement of phase coherence among protons. Spectroscopic techniques are not able to provide such local information because of the limited spatial resolution.

STM has shown the capability to probe and manipulate the intramolecular and intermolecular proton dynamics at the single-molecule level [15,46,49,130,230–232]. What is more, the impact of local environment on the proton dynamics has also been investigated by modifying the surrounding environment with atomic precision [15,232]. However, the observed proton hopping in those works was mainly induced by inelastic tunneling electrons or thermal fluctuations, leading to classical over-barrier motion, whereas the through-barrier quantum tunneling of proton was seldom explored.

As a pioneering work, Lauhon and Ho directly observed with STM, the quantum tunneling of single H atoms on Cu(001) surface and further characterized the transition temperature (60 K) from thermally excited hopping to quantum tunneling based on the dependence of H/D hopping rate on the temperature [13]. Subsequently, the quantum tunneling of heavy atoms and molecules were also directly visualized with STM [127–129]. What's more, Kumagai et al. suggested that the H tunneling was involved in the flipping motion of OH/OD group and H bond exchange within the water dimer [14,49]. The sequential proton tunneling has also been evidenced in the H-bonded water-hydroxyl chain [130]. Recently, Koch et al. presented the direct observation of stepwise double proton tunneling in a single porphycene molecule on a Ag(110) Surface [133]. In spite of those great achievements, whether the concerted proton tunneling exists or not still remains controversial [17,32,33,233]. In this section, we present the direct observation of concerted proton tunneling in a cyclic water tetramer adsorbed on the NaCl(001) surface [131,234] using the submolecular-resolution imaging technique [175].

4.2. Chirality switching of the water tetramer

Water tetramers adsorbed on the NaCl surface exhibit two different chiral states, clockwise and anticlockwise H-bonded loops, which can be distinguished by orbital imaging based on STM (Section 2.1) [175]. Apparently, the chirality of a water tetramer could be switched once the four H-bonded protons collectively transfer towards the nearest neighbor oxygen atoms through the H bonds. Therefore, the proton transfer dynamics can be investigated by probing the chirality switching of the water tetramer.

Using a Cl-terminated tip, we show the possibility of manipulating the reversible interconversion of two different chiral states of the water tetramer in a well-controlled manner (Fig. 21a). The proton dynamics could be monitored by recording the tunneling current as a function of time (Fig. 21b). When the tip is far above the water tetramer, the tunneling current is constant, indicating the chirality switching doesn't happen. After approaching the Cl-tip towards the tetramer, the tunneling current increases dramatically and splits into two levels. The upward and downward jump of the tunneling current from one level to the other arises from the reversible interconversion between the two chiral states. The Cl-tip was usually positioned slightly off the center of the tetramer in order to read out the current difference between the two chiral states. Retracting the tip to the initial height at any of the two levels left the tetramer in a certain chirality, which could be identified by high-resolution orbital imaging. This method allows us to attribute the high and low current level to the anticlockwise state (AS) and clockwise state (CS) of the water tetramer, respectively. Besides the two-level current trace, we also observed multi-level (three, four, five and six levels) current trace, which may arise from the structural relaxation of the Cl atom adsorbed at the tip apex at small tip-water distance [131].

In order to analyze the chirality switching in a quantitative way, the switching rates of AS → CS and CS → AS are extracted from the current versus time trace by fitting the lifetime distribution of the higher and lower current levels, respectively, to an exponential decay (Fig. 22). To achieve reliable statistics of the intervals of each state, hundreds of switching events are required. The switching rate was obtained simply by taking the inverse of the decay constants.

4.3. Mechanism of the proton transfer

In order to explore the mechanism of proton transfer in the water tetramer, we carried out a series of controlled experiments by varying the bias voltage and temperature as well as isotope substitution experiments. As shown in Fig. 23a, within the sample bias range from −6 mV to 4 mV, the switching rates of AS → CS and CS → AS remain nearly the same. It suggests that both of the switching rates are independent on the magnitude as well as the polarity of the bias voltage and the tunneling current. When the sample bias was set to zero, the switching dynamics did not cease, but with the same rate as the case of finite bias voltages. These results reveal that the chirality switching is neither induced by the excitation of the inelastic tunneling electrons [151,235], nor by the electric field between the tip and the sample [236].

Another very important factor that might dominate the proton dynamics is the thermal effect. Upon changing the temperature from 5 K to 15 K, the switching rates of the water tetramer stay almost constant except for the slight increase at 15 K (Fig. 23b), clearly deviating from the Arrhenius-law behavior, which excluded the influence of the thermal fluctuations [13]. Therefore, it is very likely that the proton transfer in the water tetramer is driven by quantum tunneling. The proton tunneling was further confirmed by the isotope substitution experiment, which showed that the switching rate of a D_2O tetramer dropped two orders of magnitude with respect to the H_2O tetramer (Fig. 23c). The similar isotope effect has been observed in the H bond exchange process within a water dimer adsorbed on the Cu(110) surface at 6 K [49]. However, whether the many-body tunneling is concerted or sequential is still unclear.

We notice that strong isotope effect for the anion state was also reported by Petek et al. previously, where the lifetime of the anion state is quite long [237]. In our experiment, the lifetime of the tunneling electron staying in the water molecule is very short and the

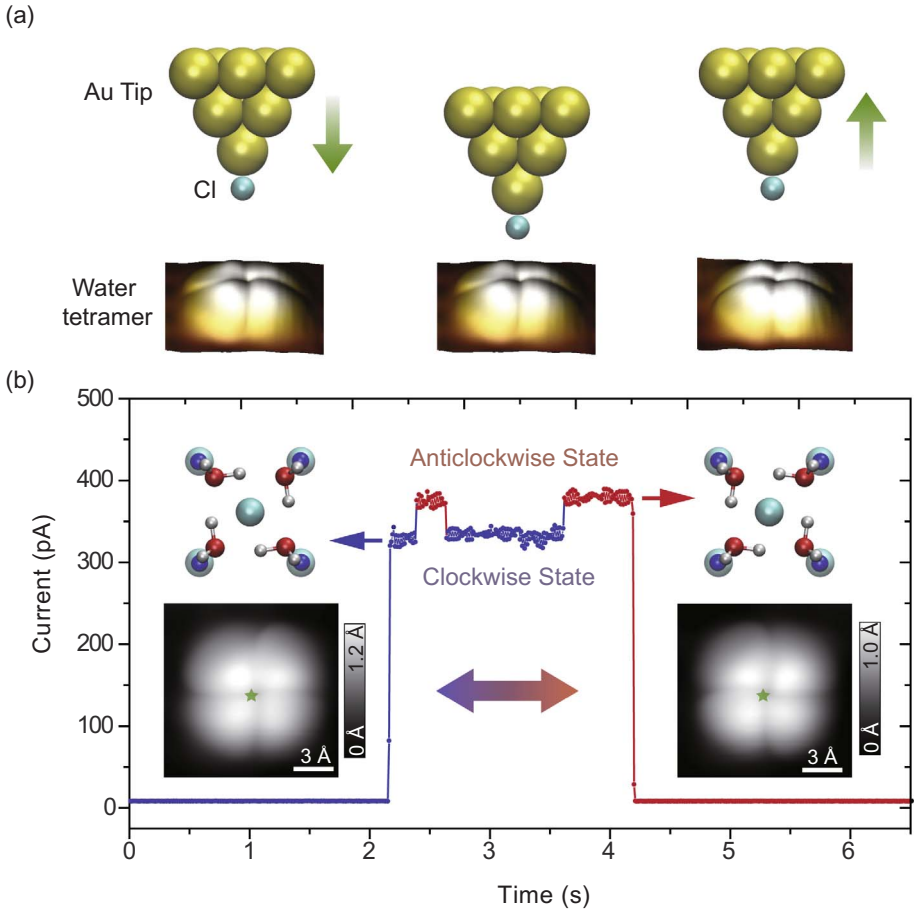

Fig. 21. Chirality switching of a water tetramer. (a) Manipulation procedure of chirality switching of a water tetramer with a Cl-functionalized tip. Left, the tetramer stays in the clockwise state (CS) at large tip height (5 mV and 5 pA). Middle, approaching the tip toward water tetramer by 230 pm, then the tetramer would undergo reversible interconversion between two H-bonding chiralities. Right, retracing the tip to the original tip height leaves the tetramer in the anticlockwise state (AS). (b) Tunneling current trace during chirality switching acquired at the position of green stars on the water tetramer. The higher and lower level of current correspond to the AS and CS state, respectively. The adsorption configuration and STM images of CS and AS state of tetramer are inserted in the (b). O, H, Au, Cl^- and Na^+ are denoted by red, white, golden, cyan and blue spheres, respectively. Reproduced from Ref. [131] with permission. (For interpretation of the references to color in this figure legend, the reader is referred to the web version of this article.)

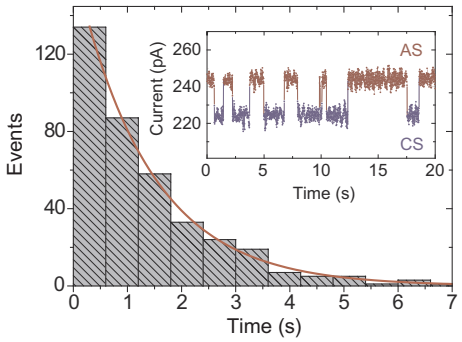

Fig. 22. Extraction of the chirality switching rate. Based on the current trace versus time (inset), we obtain the lifetime distribution (bin size: 0.6 s) of the clockwise tetramer, which is fitted by an exponential decay (red curve) with a time constant of 1.37 s. The switching rate is the inverse of the time constant, $(0.73 \pm 0.016)\ s^{-1}$. The current trace is acquired at a sample bias of 3 mV and a tip height of −295 pm, referenced to the gap set with V = 5 mV and I = 5 pA. Reproduced from Ref. [131] with permission. (For interpretation of the references to color in this figure legend, the reader is referred to the web version of this article.)

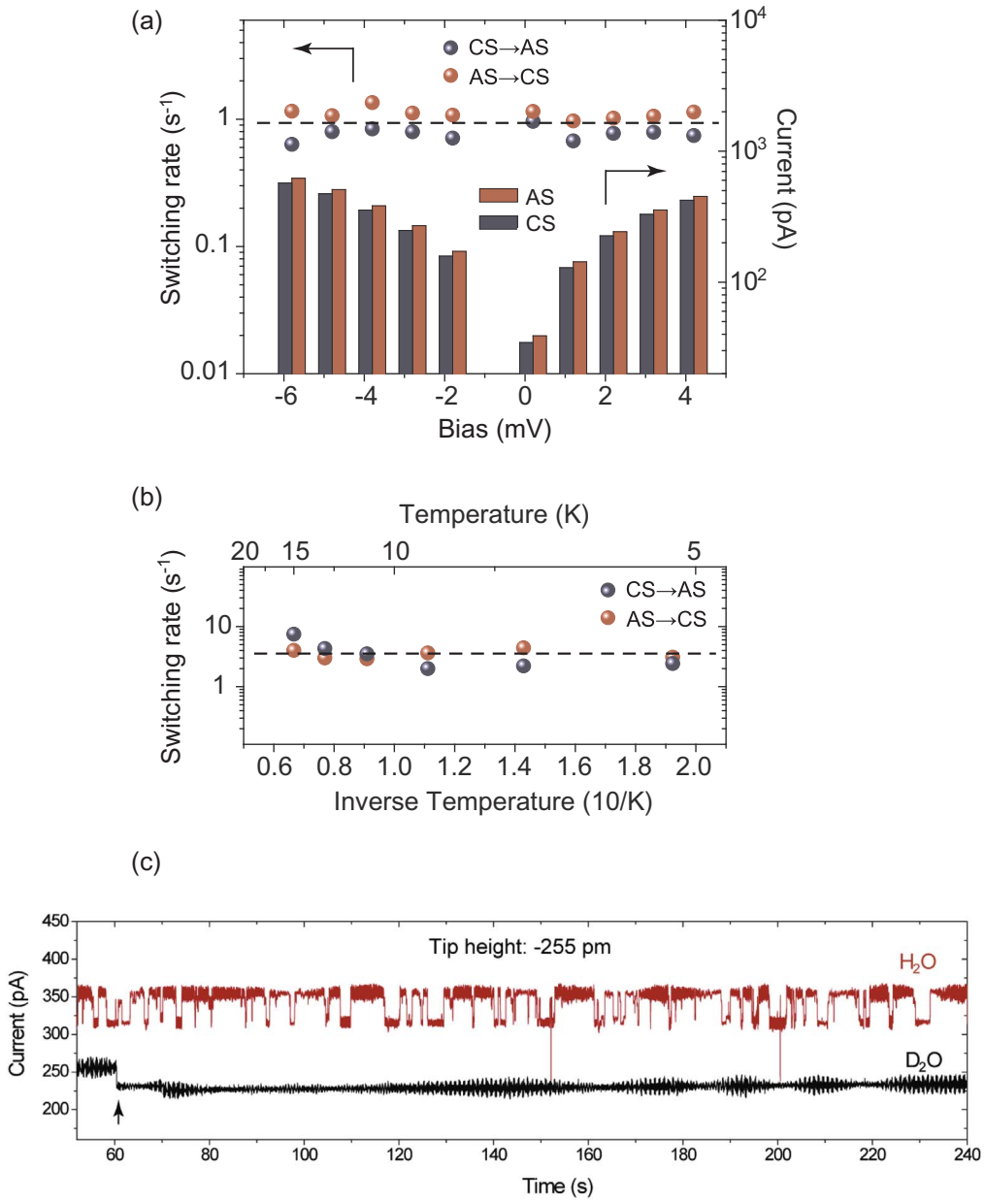

Fig. 23. Quantum nature of the proton transfer in the water tetramer. (a) Switching rate and tunneling current as a function of the sample bias with the tip height of −295 pm. (b) Switching rate as a function of temperature. Sample bias: 5 mV and tip height: −260 pm. The dashes lines in (a) and (b) are the average of switching rates. (c) Tunneling current trace of H_2O and D_2O water tetramer during chirality switching. Tip height is referenced to the gap set with V = 5 mV and I = 5 pA. Reproduced from Ref. [131] with permission.

electron will transfer to the tip quickly due to the strong tip-molecule coupling [131,175]. Therefore, the isotope effects of the chirality switching rate in our experiment occur in the neutral water molecule.

To gain deeper insights into the proton tunneling, we calculated the reaction barrier for the interchange between the AS and CS of the water tetramer using the climbing image nudged elastic band (cNEB) method [238] based on *ab initio* DFT. Calculation results verified that the energy barrier is the lowest when the four protons hop concertedly towards the nearest neighbor oxygen atoms (Fig. 24a). Any conceivable sequential or stepwise rearrangement of the protons would result in significantly higher barrier heights (Fig. 24b). In addition, the collective rotation of four water molecules could also lead to the chirality switching of water tetramers. However, such a mechanism could be excluded considering the following two points. On the one hand, the calculated reaction barrier exhibits a monotonic decrease when approaching the tip to the water tetramer, which is not agreement with the experimental behavior (Fig. 25a, see the discussion in Section 4.4). On the other hand, in contrast to the substantial reduction of the switching barrier due to NQEs for collective proton tunneling, NQEs on the barrier of collective molecular rotation are much weaker according

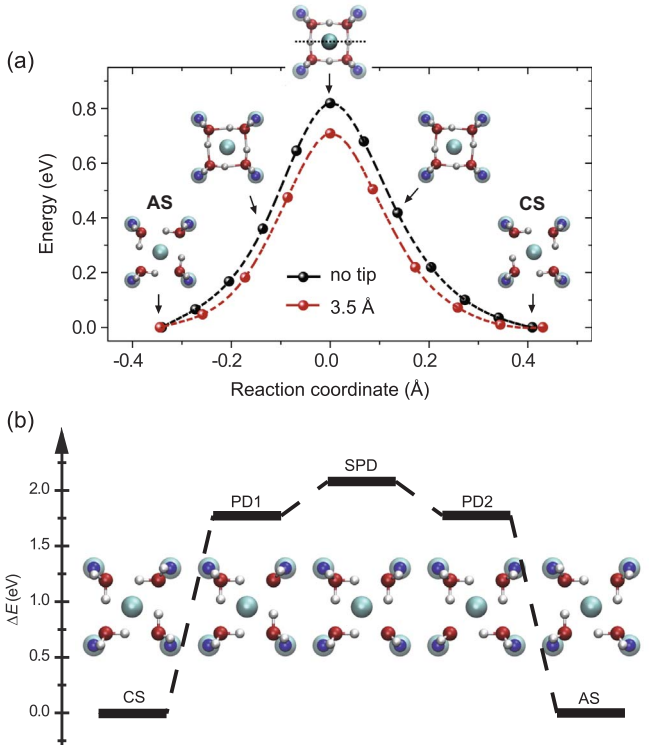

Fig. 24. Reaction barrier for the chirality switching of water tetramer. (a) Reaction barrier for the concerted proton transfer in a water tetramer with and without tip. Insets show snapshots along the transition path. The calculated reaction barrier did not include the ZPE correction. (b) Energy profile of the stepwise proton transfer in a water tetramer. In a stepwise proton transfer process two paired defect states (PD1 and PD2) and a separated paired state (SPD) are visited. Insets show the structures of these states. Reproduced from Ref. [131] with permission.

to the PIMD simulations. The preference of concerted proton movement was also substantiated by constrained PIMD simulations in a H-bonded loop of bulk ice recently [33]. In addition, both the barrier height and width were reduced once the Cl-tip was positioned above the center of the tetramer (Fig. 24a).

We noticed that the minimal reaction barrier is about several hundreds of meV, which is too high to be overcome by classical thermal fluctuations or electron excitation, as the experiment was conducted at low temperature ($T < 20$ K) and small bias voltage ($V < 10$ mV). Therefore, the interchange of the AS and CS of the water tetramer is dominated by concerted and collective quantum tunneling of four protons. As a matter of fact, our NEB calculation shows that along with the proton transfer motion as displayed in Fig. 24a, the oxygen atoms in the tetramer undergo inward displacement simultaneously. It is likely that the internal breathing mode of the tetramer is involved in the concerted proton tunneling process, leading to a phonon-assisted tunneling process [239,240].

4.4. Impact of local environments on the concerted proton tunneling

The Cl-tip can be used to probe the impact of atomic-scale environment on the concerted proton tunneling by tuning the coupling between the Cl-tip and the water tetramer in xyz dimensions. We first investigate the effect of tip height (z dimension). As presented in Fig. 25a, the proton tunneling in the water tetramer is extraordinarily sensitive to the tip-molecule distance. Moving the tip toward the water tetramer, the switching rates first undergo an initial rise (region I) followed by a rapid drop (region II). At smaller tip heights, the switching rate of CS → AS is much larger than the AS → CS, implying that the water tetramer prefers to stay at the AS, which is caused by the asymmetric double-well potential. Such an asymmetry can be understood considering the fact that the STM tip was not located at the perfect geometry center of the water tetramer so as to distinguish the two chiral states.

In order to understand the dependence of switching rate on the tip height, we calculated the effective energy barrier by subtracting from the original potential barrier the zero-point energy difference between the initial and transition states of the adsorbed water tetramer (Fig. 25b). As the tip moved towards the water tetramer, both the barrier height and width fall off. Further decreasing the tip height, the barrier height and width exhibit a reversal behavior, which is consistent with the experimental observations (Fig. 25a).

To clarify the crucial role of the Cl-decorated tip in the tetramer switching, we calculated the electron density differences of Cl-tip/tetramer/NaCl-bilayer system (Fig. 25c) in a plane perpendicular to the surface (Fig. 25d–f). DFT calculations reveal that the Cl atom at the tip apex is not neutral, but negatively charged with a partial charge of 0.4e. When a Cl-tip was placed above the tetramer, local charge rearrangement appeared with depletion (accumulation) of density on the H (Cl) atoms, implying the formation of weak electrostatic attractive interaction between the H^+ and $Cl^{\delta-}$ (Fig. 25d). At smaller tip height, the charge rearrangement is enhanced

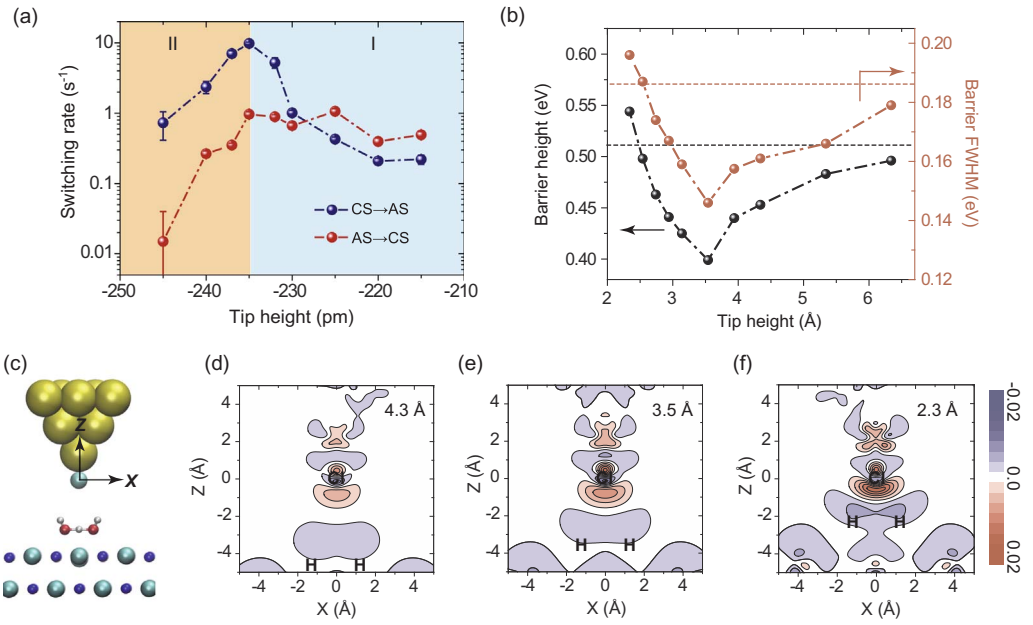

Fig. 25. Dependence of the switching rate on the tip height. (a) Switching rate as a function of tip height. With decreasing tip height, the switching rate first undergoes a rise (region I), then a rapid drop (region II). Sample bias: 5 mV. Tip height is referenced to the gap set with V = 5 mV and I = 5 pA. (b) Calculated effective barrier height and full-width at half-maximum (FWHM) as a function of tip height after considering the ZPE difference between the initial and transition states. The tip height is defined as the distance between the Cl atom on the tip and the centroid of four oxygen atoms of the water tetramer. The dashed lines denote the barrier height and width without the tip. (c) Schematic model of C-tip/water tetramer/NaCl system. (d–f) Calculated electron density difference of the experimental system (a) at the plane perpendicular to the NaCl surface with the tip-water distance of 4.3 Å (d), 3.5 Å (e), 2.3 Å (f), respectively. Red and blue in the color bar represent electron gain and depletion, respectively. The units of electron density are e Å^{-3}. Reproduced from Ref. [131] with permission.

producing stronger electrostatic force (Fig. 25e). This attractive interaction facilitates the proton transfer through the H bonds. Thus, the reaction barrier is lowered when the Cl-terminated tip approaches the water tetramer. However, Coulomb repulsion between the O^{2-} and $Cl^{\delta-}$ gradually dominants over the H^{+} and $Cl^{\delta-}$ attraction when the tip-water distance is too small (Fig. 25f), leading to the expansion of O—O separation and consequently the rapid increase of reaction barrier. Therefore, the switching rates of the two H-bonded chiral states of the tetramer are very sensitive to the local environment, determined by the delicate competition between the H^{+}–$Cl^{\delta-}$ attraction and the O^{2-}–$Cl^{\delta-}$ repulsion.

Another very interesting finding is that the concerted proton tunneling is extremely sensitive to the lateral position of the Cl-tip (x–y dimensions). Moving the tip only 0.5 Å from the center to the edge of the tetramer, the switching rates dropped by almost one order of magnitude (Fig. 26). Such a fast decay is closely related to the collective and concerted nature of the proton tunneling. When the Cl-tip was at the center of the tetramer, the Cl anion at the tip apex interacted with the four protons equally. Then four protons could be considered as a quantum quasiparticle and moved in a fully correlated manner. However, the degeneracy of the four H bonds was broken because of the asymmetric coupling between the Cl anion and the four protons once the tip was positioned off the center of the tetramer. As a result, the correlated proton tunneling would be dramatically suppressed. In addition, the collective

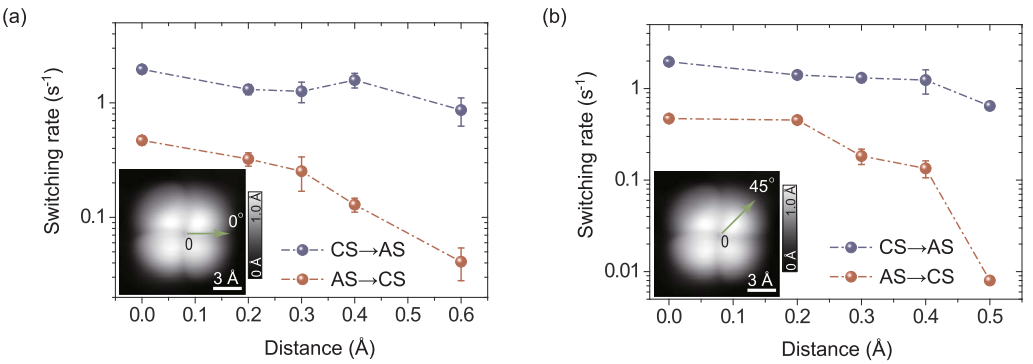

Fig. 26. Dependence of the switching rate on the lateral position of the Cl-tip. (a, b) Switching rates acquired at the different lateral positions of the tip along the 0° and 45° direction away from the center of the tetramer (highlighted by the green arrows), respectively. The zero point of the tip position is set about 0.1 Å away from the center of the tetramer so as to distinguish the two different chiral states in the tunneling current. The error bars represent the standard error. Sample bias: 5 mV. Tip height: −265 pm referenced to the gap set with V = 5 mV and I = 5 pA. Reproduced from Ref. [131] with permission.

proton tunneling could also be destroyed upon the partial deuteration, which has been reported by Drechsel-Grau and Marx through PIMD simulations [136,233].

4.5. Recent advances of concerted proton tunneling in water and ice

Recently, similar concerted proton tunneling has been also observed in water hexamer prism and bulk ice, using rotational spectroscopy [16] and dielectric measurement [34], respectively, indicating that it may be a very general phenomenon in water/ice and other H-bonded materials. In addition, the existence of concerted proton tunneling implies that the proton dynamics in ice does not freeze out even at very low temperature [17], which may be responsible for the nonzero value of the zero-temperature entropy of ices I_h [241]. A recent theoretical study pointed out that the protons in ice I_h could form a quantum liquid at low temperatures, in which protons are not merely disordered, but continually fluctuate between different configurations obeying the ice rules [242].

5. Nuclear quantum effects of H-bonding strength

5.1. Background

NQEs, in terms of zero-point fluctuation, could influence the H-bonding interactions and consequently the structure of H-bonded networks due to the anharmonic nature of the potential well (see Section 1.1). For instance, high-pressure ice exhibits a prominent proton delocalization effect between the oxygen atoms due to the relatively small O—O separation, leading to the blurring between covalent bond and H bond [1,35,107,243]. The magnitude of proton delocalization is quite sensitive to the distance of two nearest neighbouring oxygen atoms, as evidenced in the water-hydroxyl complex on metal surfaces using the PIMD calculations [45]. Experimentally, the symmetric H bond was observed in a water-hydroxyl complex on Cu(110) surface by STM [46], which confirmed the proton delocalization effect.

Conventionally, the Ubbelohde effect yields an elongation of the O—O distance and the weakening of H bond upon deuteration, whereas the reverse Ubbelohde effect has also been observed [121,213]. SFG spectroscopy combined with PIMD calculations revealed that the NQEs influence the bond orientation of the interfacial water (HOD), in which the OH bond prefers to orient up toward the vapor phase, whereas the OD tends to form a D bond with the bulk water because of the stronger D bond of the deuterium [126]. In HF H-bonded systems, both weakening and strengthening of H bond by NQEs was reported by the theoretical PIMD calculations, depending on the cluster size [64,81,244]. Up to now, a clear cohesive picture for the influence of NQEs on the H-bonding strength at the atomic level is still not available and it still remains an open question how large the quantum component of the H bond is in spite of the enormous theoretical efforts devoted to proper treatment of the nuclear motion at the quantum mechanical level [4,30,98,106,245].

The estimation of H-bonding strength comes from the redshift (softening) in the X–H stretching frequency of the H-bond donor molecule [206]. As described in Section 2.2, the recently developed tip-enhanced IETS enables us to probe the vibrational energy of O—H/D stretching mode with ultrahigh accuracy. In this section, we will report the quantitative assessment of NQEs on the strength of a single H bond formed at a water-salt interface using the tip-enhanced IETS technique and discuss the key impact of the local environment on the NQEs.

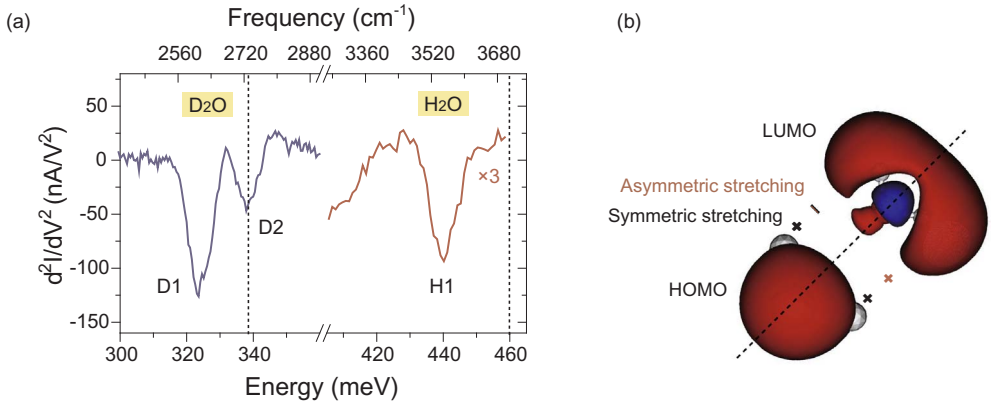

Fig. 27. High-resolution IETS of stretching mode. (a) d^2I/dV^2 spectra of D_2O (blue) and H_2O (red) monomers. Vertical dashed lines denote the vibrational energies of the free OD and OH stretching modes. D2 mode coincides with that of the free OD stretching. The D1 mode exhibited considerable red-shift because of the formation of D bond with the NaCl surface. (b) The symmetry of HOMO and LUMO with respect to the plane (marked by a dashed line) is the same as that of the symmetric stretching mode, but opposite to that of the asymmetric one, resulting in larger IETS signal of the symmetric mode. Reproduced from Ref. [132] with permission. (For interpretation of the references to color in this figure legend, the reader is referred to the web version of this article.)

5.2. Stretching mode of water monomers

The stretching mode of water is of particular interests since it is most sensitive to the H bond interactions and NQEs. However, measuring reliable signals of stretching mode with STM-IETS has long been a challenge. Using tip-enhanced IETS, we can obtain the high quality stretching band frequencies of a D_2O monomer (Fig. 27a). As we already know, the water monomer adsorbed on the NaCl surface in a "standing" configuration has one dangling OD and the other D-bonded OD [175]. Accordingly, the D_2O shows two distinct stretching modes (D1 and D2 in Fig. 27a). The energy of D2 mode coincides with that of the free OD stretching frequency and thus should mainly arise from the upright dangling OD bond. The D1 mode exhibits considerable redshift because of formation of the D bond with the NaCl surface. We have also acquired the IETS of a H_2O monomer, in which only the red-shifted H1 mode appeared. The signal of H2 mode might be too weak and beyond our detection limit.

Due to the coupling-induced mode mixing, the D1 (D2) mode actually corresponds to a symmetric (asymmetric) stretching mode. We notice that the weight of the symmetric (asymmetric) stretching mode is mostly on the bonded (free) OD, suggesting a weak coupling between the two modes. We note that the spectral intensity of symmetric stretching mode (D1) is much larger than that of the asymmetric stretching mode (D2) (Fig. 27a), which can be explained by considering the symmetry of the vibrational modes and electronic states [202]. As shown in Fig. 27b, both the HOMO and LUMO are symmetric with respect to the plane containing the line equally dividing the D−O−D angle, and perpendicular to the D−O−D plane. Since the D2 mode is anti-symmetric with respect to the plane, its matrix element should be much smaller than that of D1 mode, resulting much weaker IET signal. Recently, Shiotari et al. also reported the role of molecular resonance state around E_F in the qualitative analysis of IETS based on the propensity rules [246]. IETS propensity rules allow us to selectively activate the vibrational modes by properly functionalizing the tip apex, as discussed in Section 2.2.4 (Fig. 16).

As mentioned in Section 2.2.4, we could obtain the intrinsic energies of the vibrational modes via extrapolating the fitting curves to infinite tip height to eliminate the tip effect (Fig. 17). Compared with the OD stretching mode of a gas-phase HOD molecule (338 meV), the extrapolated D2 energy (338.7 ± 0.3 meV) is mildly blue-shifted, mainly arising from the intramolecular vibrational coupling between the D1 and D2 transition dipoles [247].

5.3. Tuning the H-bonding strength with Cl-tip

Using tip-enhanced IETS triggered by STM, we have obtained high-resolution vibrational signals of a water monomer adsorbed on the Au(111)-supported 2 ML NaCl (001) films, in particular the stretching mode. By changing the tip height, we can tune the strength of the H bond formed between the water and the NaCl substrate in analogy to high-pressure experiments. We plot the 2D color map of the stretching bands of a D_2O monomer as a function of tip height (Fig. 28a). The D1 and D2 modes are both red-shifted with decreasing tip height. D2 mode vanishes at a certain tip height and subsequently D1 mode changes from symmetric line shape to asymmetric Fano-shape feature. Further decreasing the tip-molecule distance, the energy of D1 mode keeps red-shifting. In a word, as

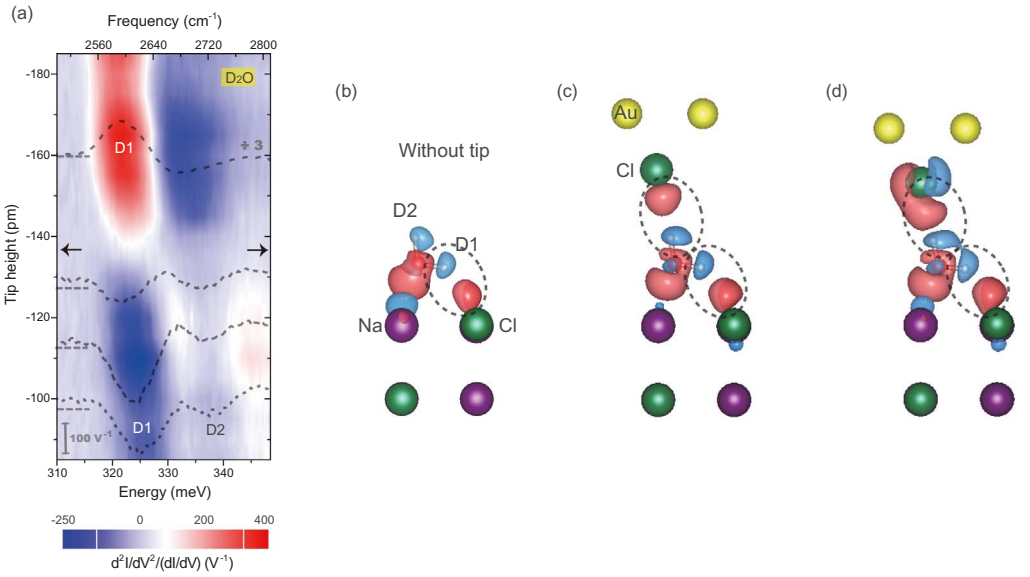

Fig. 28. Tuning the H-bonding strength by adjusting the tip height. (a) Two dimensional (2D) IETS color map of the D1 and D2 mode of a D_2O monomer as a function of tip height. Four typical IET spectra at different tip heights (dashed curves) are superimposed onto the color map. At the tip height of −1.36 Å (denoted by arrows), the D2 mode almost fade out and the line shape of D1 mode changed from symmetric to asymmetric. (b–d) The isosurface contours of differential charge density of the water/NaCl system without (b) and with Cl-terminated tip at the tip height of 4.25 Å (c) and 3.45 Å (d). Red and blue represent charge gain and depletion, respectively. Dashed ellipses denote the local charge arrangement due to the water-NaCl interactions and tip-water interactions. The tip height is defined as the vertical distance between the Cl atom at the tip apex and O atom of the water molecule. Reproduced from Ref. [132] with permission.

the tip approaches the water molecule, the stretching modes shift to lower energies, implying a strengthening of the H bond. In such a manner, we can continuously modify the H-bonding strength simply by adjusting the tip height.

In order to confirm that the H bond can be tuned by the tip, we calculated the electron density difference of tip/water/NaCl system (Fig. 28b–d). When the tip is absent, except for the local charge rearrangement between the water molecule and the NaCl, there is no obvious charge transfer or orbital hybridization. The charge rearrangement highlighted by dashed ellipse (Fig. 28b) denotes the H-bond character between the D1 atom and the Cl^- of the NaCl surface. When the STM tip is introduced, additional local charge rearrangement appears between the D2 atom and the Cl atom at tip apex (Fig. 28c), indicating the formation of H bond between the STM tip and the water molecule. As the tip height decreases, the water is gradually pushed close to the NaCl surface due to the Pauli repulsion force between the close-shell water molecule and the Cl-tip, resulting in enhancement of the local charge rearrangement in the regions of the two H bonds (highlighted by two ellipses in Fig. 28d). That is the reason why the H bond is strengthened with decreasing tip height, corresponding to the measured redshifts of both D1 and D2 modes.

5.4. High-resolution IETS of the HOD monomer

As we have already mentioned in Section 5.2, the intramolecular vibrational coupling between D1 and D2 transition dipoles of the D_2O monomer leads to an additional shift of the measured energies, thus complicating the determination of the H-bonding energy. While the intramolecular coupling is absent in a HOD monomer due to the large energy mismatch of the OH and OD stretching mode. So, we switched to measure the IETS of the HOD monomer. Surprisingly, both the OH and OD stretching modes show considerable redshifts (Fig. 29), suggesting they are both H-bonded. At smaller tip heights, the D2 mode appears coexisting with the D1 and H1 mode (Fig. 29a). These features indicate that the water monomer might be rapidly flipping so that the OH and OD form H-bonds with the NaCl surface alternatively (Fig. 29b). To confirm such a flipping behavior, we calculated the flipping barrier using NEB method in VASP. We found that the energy barrier for the flipping motion is as small as 20 mV [132], such that the flipping motion of a water monomer could be easily excited by the tunneling electrons during the IETS measurements.

In order to accurately extract the vibrational energy from the IET spectra, especially from those with asymmetric line shapes, we fitted the IETS data using a model of resonantly enhanced IETS [196,205]:

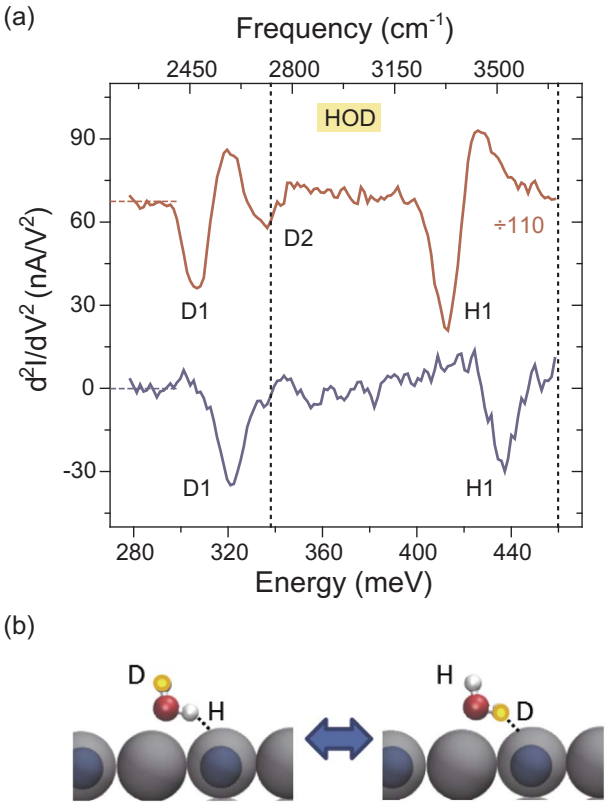

Fig. 29. High-resolution IETS of a HOD monomer. (a) IET spectra of the stretching mode of a HOD monomer at the tip height of −1.4 Å (blue curve) and −2.3 Å (red curve). (b) Schematic model of the alternatively formation of H bond between the OH/OD and the Cl^- via rapidly flipping of the HOD monomer. O, H, D, Cl^- and Na^+ are denoted by red, white, golden, gray and dark-cyan spheres, respectively. Tip height is referenced to the gap set with V = 100 mV and I = 50 pA. Reproduced from Ref. [132] with permission.

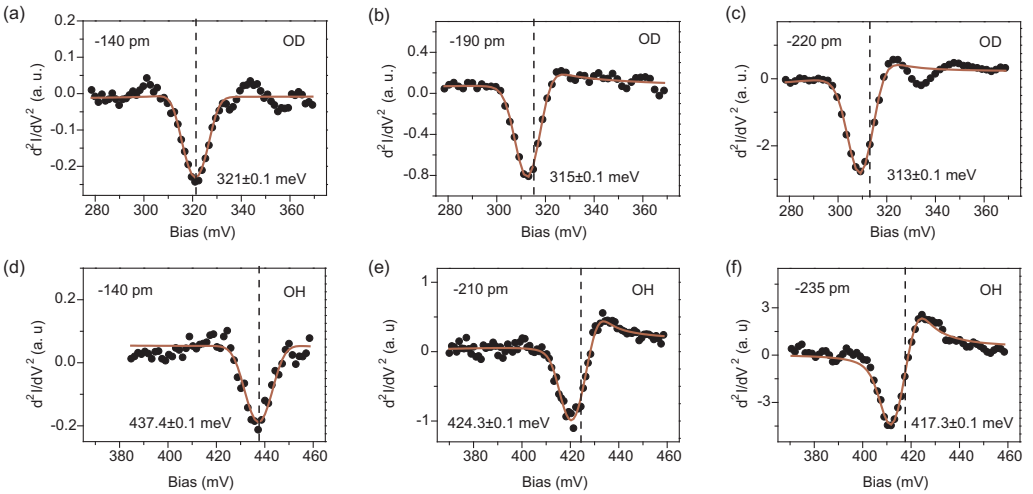

Fig. 30. IETS fitting for the H-bonded stretching modes of a HOD molecule at different tip heights. (a–c) OD stretching mode. (d–f) OH stretching mode. The tip height (indicated at the upper left of each graph) is referenced to the gap set with: V = 100 mV and I = 50 pA. The vibrational threshold energies obtained by IETS fitting are denoted by vertical dashed lines. The errors (0.1 meV) reflect the fitting error based on estimated Hessian and covariance of residuals. Reproduced from Ref. [132] with permission.

$$\sigma = \frac{m^2}{(\in_a - \in_F)^2 + (\Gamma/2)^2}\left\{\frac{(\in_a - \in_F + \hbar\omega)^2 - \left(\frac{\Gamma}{2}\right)^2}{(\in_a - \in_F + \hbar\omega)^2 + \left(\frac{\Gamma}{2}\right)^2}\Theta(eV - \hbar\omega) + \frac{\Gamma}{\pi}\frac{\in_a - \in_F + \hbar\omega}{(\in_a - \in_F + \hbar\omega)^2 + \left(\frac{\Gamma}{2}\right)^2} ln\left|\frac{eV - \hbar\omega}{\hbar\omega}\right|\right\} \quad (4)$$

Here, σ is the total tunneling conductance, m is the electron-vibration coupling constant, $\in_F$ is the Fermi energy. $\in_a$, resonance state of the molecule, denotes the position of the molecular resonance with respect to E_F, and is coupled to the left and right electrode with constant Γ_L and Γ_R, respectively.

It should be noticed that the expression applies only when $\Gamma_{Tip} = \Gamma_L = \Gamma \gg \Gamma_R = \Gamma_{Sur}$. In our case, the water molecule is strongly coupled to the STM tip, and decoupled from the Au substrate by the NaCl bilayer film, thus satisfying the requirement. With this model, we achieve excellent agreement between simulated and experimental IETS data (Fig. 30).

5.5. Impact of NQEs on the strength of a single H bond

Due to the flipping motion of water monomer on NaCl surface, OH and OD form H bonds with the Cl^- alternatively. This offers us a perfect platform to probe the NQEs on the H-bonding strength by comparing the H1 and D1 modes in the same HOD molecule with the same STM tip. First, we plot the ratio between the vibrational frequency of H1 and D1 stretching modes as a function of tip-water distance (Fig. 31a). In general, the ratio decreases as the STM tip approaching the water molecule and crosses over the value of 1.361, which is the ratio of the free HOD monomer in gas phase, where without NQEs [248]. In addition to the general decreasing trend

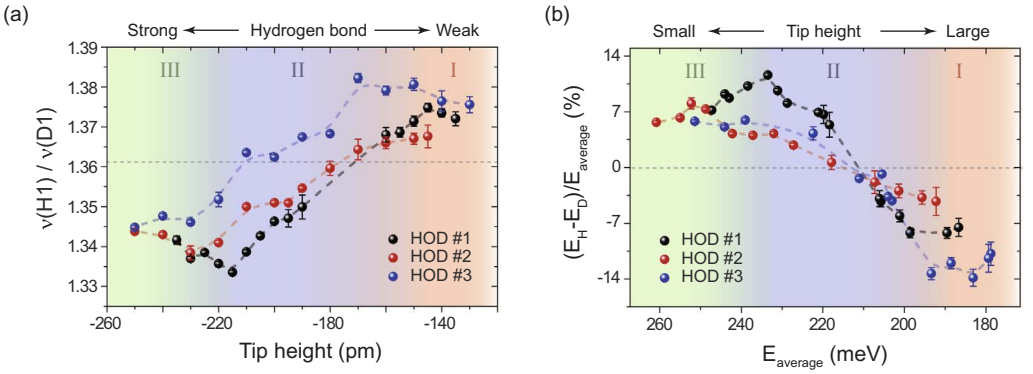

Fig. 31. Impact of NQEs on the H-bonding strength of HOD monomers. (a) Tip height dependence of the ratio between the vibration frequency of H1 and D1 mode, showing an initial increase (region I) followed by a monotonous decay (region II) until a turnover appears (region III) as the tip height decreases. The ratio (1.361) between the frequency of free OH and OD stretching modes is indicated by a horizontal dashed line. (b) Relative difference between the H-bonding energies of O—H···Cl (E_H) and O—D···Cl (E_D) as a function of their averaged energies ($E_{average} = (E_H + E_D)/2$). The data of different color (red, blue, black) are obtained from three different HOD water monomers, exhibiting the similar trend. Error bars in (a) and (b) are calculated by the uncertainty propagation formula from the fitting errors of the D1 and H1 modes. Reproduced from Ref. [132] with permission.

(region II), reversal behaviors appear at the large and small tip heights (region I and region III in Fig. 31a). The variation of the ratio at different tip heights clearly indicates that the H-bonding strength changes upon isotope substitution because of the NQEs. The data of different molecules exhibit the same trend but with distinct variation, mainly due to the different tip apex structure and the inhomogeneous local environment of the molecules resulting from the Au(111) substrate.

The H-bonding energy could be converted from the redshift of the H-bonded OH stretching frequency (relative to the free OH stretching energy) using an empirical formula [206]:

$$\Delta H = 1.3 \times \sqrt{\Delta\nu} \tag{5}$$

where ΔH is the H-bonding energy, in kJ/mol; $\Delta\nu$ is the redshift of the OH stretching mode, in cm^{-1}. We could also convert the unit of H-bonding strength to meV by: 1 kJ/mol = 10.4 meV/atom. To apply Eq. (5) to the OD stretching mode, the quantity $\nu(OH)\Delta\nu$ should be multiplied by a factor: $\nu(OH)/\nu(OD) = 1.3612$ [248], where and $\nu(OD)$ are the OH and OD stretching frequencies of the free HOD molecule, respectively. In tip-enhanced IETS, the tip-water coupling is very strong such that the HOMO of water can be shifted and broadened significantly towards the E_F, leading to very short lifetime of electron/hole staying in the water molecule. Therefore, we are still in the weak electron-vibration (e-vib) interaction regime, which will not change the character of the OH and OD stretching frequencies.

This empirical formula allows us to convert the redshifts of H1 and D1 into H-bonding energies, from which we obtained the relative difference of H-bonding energy between O—H···Cl and O—D···Cl as a function of their averaged energies (Fig. 31b). Generally, the NQEs weaken the weak H bond and strengthen the relatively strong ones. In addition, we noticed that the impact of the NQEs tends to fade out at the strong- and weak- H-bond limits. Surprisingly, the quantum component of the H bond could be up to 14%, which is even bigger than the thermal energy at room temperature. When taking the average of seven different groups of data [132], the crossover behavior of the NQEs is still observable, but the turning point at the strong- and weak-bond limits are smeared out. Therefore, the ability to probe the H-bonding strength at single bond limit is critical to accurately assess the impact of NQEs.

5.6. The physical picture of NQEs on the H-bonding strength

To explore the physical picture of the impact of NQEs on the H-bonding strength, we calculated the H1/D1···Cl distance and the corresponding H-bonding energy based on the PIMD simulations. As the tip approaches the water molecule, the H-bond length decreased and H-bond energy becomes stronger [132]. Additionally, prominent isotope effects on the H-bonding interactions are demonstrated in Fig. 32a (black curve), nicely reproducing the experimental observations: the NQEs weaken the weak H bonds and strengthen the strong ones, and tend to fade out at the strong- and weak-bond limits. Then, we compare the projection of O—H and O—D covalent bonds length along the intermolecular axis. Interestingly, with decreasing tip height, the ratio of the projections between O—H and O—D Fig. 32a (red curve) shows a similar behavior as the relative H-bonding energies difference between H and D. Calculation results reveal that the anharmonic quantum fluctuations of O—H(D) mainly locate on the intramolecular covalent bond stretching and intermolecular H-bond bending. On the one hand, the zero-point motion of O—H(D) stretching increases the projection, resulting in the enhancement of the H-bonding strength. On the other hand, the zero-point motion of the H-bond bending makes the H-bond more bent, thus weakening the H bond. Therefore, there is a delicate competition between O—H(D) stretching and H-bond bending that induces the isotope effect on the H-bonding energy.

However, this picture could not explain the reversal behaviors in regions I and III. For the turning point at the weak H-bond limit, it is easy to understand since when there is no H-bonding interaction, the difference between the O—H···Cl and O—D···Cl bonding energies simply disappears. At the strong-bond limit, the reversal feature is closely related to the noncolinear geometry of the O—H···Cl H-bond. Generally speaking, the stronger the H bond is, the more collinear the geometry becomes, but it is not true for

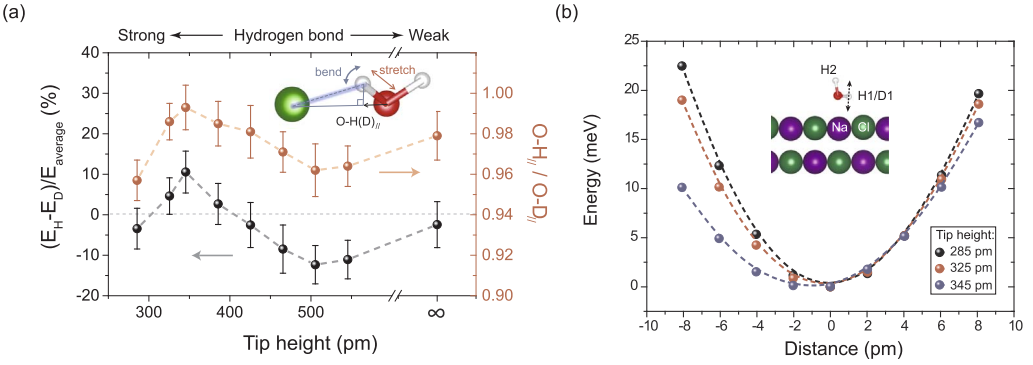

Fig. 32. The mechanism of NQEs on the H-bonding strength. (a) Calculated H-bonding energy difference when replacing H with D (black) and the ratio between averaged projection of O—H and O—D covalent bonds along the intermolecular axis (red) at different tip height. The projection geometry model is inserted in (a). Error bars reflect the statistical error in the PIMD calculations. (b) Potential energy profiles along direction of H-bond bending motion (double-ended arrow in the inset) acquired at three different tip heights (black: 285 pm, red: 325 pm, blue: 345 pm). Negative (positive) distance corresponds to the downward (upward) direction as denoted by the double arrow (inset). Reproduced from Ref. [132] with permission.

O—H···Cl H-bond because of the repulsive interaction between the H^+ of the water and the Na^+ of NaCl surface, which leads to the noncolinear configuration of the O—H···Cl H bond.

In order to clarify how such a non-collinear H-bond geometry influence the NQEs, we moved the H atom along the axis corresponding to the H-bond bending motion and plot the evolution of the PES for different tip heights (Fig. 32b). It is clear that while the energy profiles on the right-hand side (distance > 0) change mildly as the tip approaches the surface, the change of these profiles on the left-hand side (distance < 0) becomes significantly steeper. The faster rise of the energy profile close to the surface means that the zero-point motion of the H-bond bending mode tends to push the H atom further away from the surface, making the H-bond more bent. Therefore, at the small tip height (strong H-bond case) the anharmonic bending motion is greatly enhanced, giving rise to the turning point in region III. This is in clear contrast to the case of a normal collinear H-bond, where the anharmonic bending motion becomes less pronounced as the H-bond gets stronger. This reversed behavior infers that the NQEs of the H bond is extremely sensitive to the local environment, which is, at present, inaccessible by macroscopic spectroscopic methods.

The last point we want to emphasize concerning this picture of competition resides on the recently discovered temperature dependence. In Watson-Crick CG base pair, Fang et al. found that the influence of NQEs can invert strengthening the intermolecular H bond interaction to weakening it with decreasing temperatures [111]. This looks similar to the turnover discussed above. But we note that the geometric noncolinear feature of the H bond does not exist in their system. To understand this, it is important to realize that the occupation numbers of these different vibrational modes change with temperatures. At lower temperature, the bending modes can be highly populated compared with the stretching mode. Since bending weakens the intermolecular H bond interaction. It is easy to expect that this weakening feature can exist. As a matter of fact, in their paper [111], Fang and coauthors specifically calculated the evolution of the occupation numbers of the bending and stretching modes at different temperatures as well as their impact on the intermolecular interactions. They clearly demonstrated that the final influence can be rationalized using this competition of different vibrational modes in a very clean manner. Therefore, in addition to the complexity induced by the noncolinear feature of the H bond, this picture of competition between contributions of NQEs in bending and stretching modes can be enriched by further considering this temperature dependence. This picture has been discussed in detail in a recent review [7].

6. Summary and outlook

In this review, we have presented the atomic-scale investigation of NQEs of water adsorbed on the NaCl(001) surface. This was achieved by developing a series of imaging and spectroscopic techniques based on STM, which allow tracking the quantum motion of H nuclei both in real space and energy space. Thanks to those novel techniques, it is possible to directly visualize the concerted quantum tunneling of protons within the H-bonded network and quantify the quantum component of a single H bond at a water-solid interface. Furthermore, we have explored the impact of the atomic-scale local environment on the NQEs in a well-controlled manner. These findings not only renew our understanding of water from a quantum mechanical view, but also open up a new route for the studies of other H-bonded systems and light-elements materials.

As a matter of fact, the investigation of NQEs with STM is still in its infancy and there are many important issues yet to be solved. For instance, the studies in this review mainly focused on simple model systems. What if many-body correlation effects are entangled with the NQEs? It would be very interesting to study such correlated NQEs in larger water clusters or more extended H-bonded network such as overlayer ice. Considering that the collective and correlated NQEs in water should be susceptible to the partial deuteration [17,233], we could conduct partially isotope substitution experiments in a controlled fashion, where the H_2O and D_2O could be distinguished with tip-enhanced IETS and manipulated with the functionalized STM tip. In addition to the isotope effect, it is also encouraging to explore how the confinement affects the NQEs, by changing different substrates and confinement geometries. Moreover, simulation results reveal that the concerted proton tunneling in hexagonal ice changes to thermally activated sequential over-barrier hopping at a surprisingly high transition temperature ($\sim$200 K) [136]. Hence, it is imperative to carry out NQEs experiments in a wide range of temperature to explore the transition temperature from quantum tunneling to classic hopping. So far, most of the studies on NQEs are still focused on the quantum behavior of the protons themselves. The effect of nuclear quantization on the electronic degree of freedom is yet to be clarified.

Technically, there is an urgent need to develop new ways to study the NQEs. For instance, quantum motion of protons as well as the resulting electronic transition usually happen at rather short time scales (in the order of femtoseconds) [66,67], which is way beyond the temporal-resolution of STM (usually in the order of a few hundred microseconds). Ultrafast laser combined STM has been proven to be an efficient tool to overcome this limitation [249,250] and could be employed to investigate the ultrafast dynamics of NQEs. Given the insulating nature of multilayer ice or liquid water, applying noncontact atomic force microscopy (nc-AFM) to study NQEs in these complex systems is very essential. The state-of-the-art qPlus-based nc-AFM could gain much higher sensitivity to the nuclear degree of freedom than STM by probing the short-range Pauli repulsion and electrostatic force [180,251–257].

However, an intrinsic problem of STM and AFM is that all the probes inevitably induce perturbation to the fragile water structure, due to the excitation of the tunneling electrons and the tip-water interaction forces, especially under the close-imaging condition applied in order to achieve ultrahigh spatial resolution. Considering that the water molecule has a strong internal dipole moment, it is promising to achieve the weak-disturbance AFM imaging of interfacial water by probing the high-order weak electrostatic force once the tip apex is properly functionalized [258]. Furthermore, the nitrogen-vacancy (NV) center in diamond could act as a sensitive atomic-scale probe to detect very weak magnetic signals such as the spin fluctuations of protons in water and conduct NMR spectroscopy at nanoscale [259–261]. Combing NV center with SPM provides a promising tool to probe the NQEs of interfacial water at the ambient condition and in a nearly non-invasive manner.

Theoretically, in spite of several reported successful applications on surface water [45,130–132,146,154,169,175,177], it is still challenging to quantitatively decipher the atomistic details of these experimental observations. The environment of many experimental observations is hard to be accounted for with accurate atomistic details. And some observables, e.g. the chemical reaction rate, can be very sensitive to the underlying electronic structures. Changes of the transition barrier by a magnitude of chemical accuracy (1 kcal/mol) may easily result in a rate change of more than 2 orders at low temperatures. For quantum tunneling in a high-dimension system when the chemical reaction degree of freedom is strongly coupled to the others, an efficient computation scheme which is able to discriminate the different tunneling channels and allow contributions from other degrees of freedom to be accounted for accurately, is still lacking. When multiple light elements like protons are involved in this process, discriminating single and concerted tunneling mechanism and providing useful atomistic detail of the later is also in its infancy stage [15,33,130,131,133,136,233,234]. In short, there are promising possibility for exploring the exotic quantum states of light nuclei at surfaces. The methods reviewed provide an option, but alluring challenges also exist. We hope this review can stimulate new theoretical and experimental studies in this direction.

Acknowledgements

We thank many people who have supported us to fulfill the works in this manuscript: Jing-Tao Lü, Yexin-Feng, Ji Chen, Andrew Hodgson, Angelos Michaelides, Limei Xu, Junren Shi, Xiangzhi Meng, Jinbo Peng, Zeren Lin, Zhichang Wang. X.Z.L. also acknowledge helpful discussion with Zhigang Sun on quantum dynamics. This work is funded by the National Key R&D Program under Grant No. 2016YFA0300901, 2017YFA0205003, and 2016YFA0300903, the National Natural Science Foundation of China under Grant No. 11634001, 21725302, 11290162/A040106, and 61371015. Y.J. acknowledges support by National Science Fund for Distinguished Young Scholars and Cheung Kong Young Scholar Program. J. G. acknowledges support from the National Postdoctoral Program for Innovative Talents. We are grateful for the computational resources provided by the supercomputer TianHe-1A in Tianjin, China.

References

[1] M. Benoit, D. Marx, M. Parrinello, Tunnelling and zero-point motion in high-pressure ice, Nature 392 (1998) 258–261.
[2] A.K. Soper, C.J. Benmore, Quantum differences between heavy and light water, Phys. Rev. Lett. 101 (2008) 065502.
[3] A. Hodgson, S. Haq, Water adsorption and the wetting of metal surfaces, Surf. Sci. Rep. 64 (2009) 381–451.
[4] F. Paesani, G.A. Voth, The properties of water: insights from quantum simulations, J. Phys. Chem. B 113 (2009) 5702–5719.
[5] I. Errea, M. Calandra, C.J. Pickard, J.R. Nelson, R.J. Needs, Y. Li, H. Liu, Y. Zhang, Y. Ma, F. Mauri, Quantum hydrogen-bond symmetrization in the superconducting hydrogen sulfide system, Nature 532 (2016) 81–84.
[6] B. Pamuk, J.M. Soler, R. Ramirez, C.P. Herrero, P.W. Stephens, P.B. Allen, M.V. Fernandez-Serra, Anomalous nuclear quantum effects in ice, Phys. Rev. Lett. 108 (2012) 193003.
[7] M. Ceriotti, W. Fang, P.G. Kusalik, R.H. McKenzie, A. Michaelides, M.A. Morales, T.E. Markland, Nuclear quantum effects in water and aqueous systems: experiment, theory, and current challenges, Chem. Rev. 116 (2016) 7529–7550.
[8] D. Marx, Proton transfer 200 years after von Grotthuss: insights from *ab initio* simulations, ChemPhysChem 7 (2006) 1848–1870.
[9] D. Marx, A. Chandra, M.E. Tuckerman, Aqueous basic solutions: hydroxide solvation, structural diffusion, and comparison to the hydrated proton, Chem. Rev. 110 (2010) 2174–2216.
[10] M. Nishijima, H. Okuyama, N. Takagi, T. Aruga, W. Brenig, Quantum delocalization of hydrogen on metal surfaces, Surf. Sci. Rep. 57 (2005) 113–156.
[11] D.F. Brougham, R. Caciuffo, A.J. Horsewill, Coordinated proton tunnelling in a cyclic network of four hydrogen bonds in the solid state, Nature 397 (1999) 241–243.
[12] P.M. Tomchuk, V.V. Krasnoholovets, Macroscopic quantum tunneling of polarization in the hydrogen-bonded chain, J. Mol. Struct. 416 (1997) 161–165.
[13] L.J. Lauhon, W. Ho, Direct observation of the quantum tunneling of single hydrogen atoms with a scanning tunneling microscope, Phys. Rev. Lett. 85 (2000) 4566–4569.
[14] T. Kumagai, M. Kaizu, H. Okuyama, S. Hatta, T. Aruga, I. Hamada, Y. Morikawa, Tunneling dynamics of a hydroxyl group adsorbed on Cu(110), Phys. Rev. B 79 (2009) 035423.
[15] T. Kumagai, Direct observation and control of hydrogen-bond dynamics using low-temperature scanning tunneling microscopy, Prog. Surf. Sci. 90 (2015) 239–291.
[16] J.O. Richardson, C. Perez, S. Lobsiger, A.A. Reid, B. Temelso, G.C. Shields, Z. Kisiel, D.J. Wales, B.H. Pate, S.C. Althorpe, Concerted hydrogen-bond breaking by quantum tunneling in the water hexamer prism, Science 351 (2016) 1310–1313.
[17] L.E. Bove, S. Klotz, A. Paciaroni, F. Sacchetti, Anomalous proton dynamics in ice at low temperatures, Phys. Rev. Lett. 103 (2009) 165901.
[18] NIST Chemistry WebBook; NIST Standard Reference Database 69; National Insitute of Standards and Technology (NIST): Gaithersburg, MD, 2005; available at http://Webbook.Nist.gov (accessed Dec 19, 2014).
[19] IAPWS Releases, Supplementary Releases, Guidelines, and Advisory Notes. International Association for the Properties of Water and Steam (IAPWS). http://www.iapws.org/release.html (accessed Dec 21, 2014).
[20] A.I. Kudish, F. Steckel, D. Wolf, Physical properties of heavy-oxygen water. Absolute viscosity of $H_2{}^{18}O$ between 15 and 35 °C, J. Chem. Soc., Faraday Trans. 68 (1972) 2041–2046.
[21] P.G. Hill, R.D.C. Macmillan, V. Lee, A fundamental equation of state for heavy-water, J. Phys. Chem. Ref. Data 11 (1982) 1–14.
[22] M. Holz, S.R. Heil, A. Sacco, Temperature-dependent self-diffusion coefficients of water and six selected molecular liquids for calibration in accurate ^{1}H NMR PFG measurements, Phys. Chem. Chem. Phys. 2 (2000) 4740–4742.
[23] W.S. Price, H. Ide, Y. Arata, O. Soderman, Temperature dependence of the self-diffusion of supercooled heavy water to 244 K, J. Phys. Chem. B 104 (2000) 5874–5876.
[24] J.H. Root, P.A. Egelstaff, A. Hime, Quantum effects in the structure of water measured by gamma ray diffraction, Chem. Phys. 109 (1986) 437–453.
[25] B. Tomberli, C.J. Benmore, P.A. Egelstaff, J. Neuefeind, V. Honkimaki, Isotopic quantum effects in water structure measured with high energy photon diffraction, J. Phys.: Condens. Matter 12 (2000) 2597–2612.
[26] U. Bergmann, D. Nordlund, P. Wernet, M. Odelius, L.G.M. Pettersson, A. Nilsson, Isotope effects in liquid water probed by x-ray Raman spectroscopy, Phys. Rev. B 76 (2007) 024202.
[27] Y. Harada, T. Tokushima, Y. Horikawa, O. Takahashi, H. Niwa, M. Kobayashi, M. Oshima, Y. Senba, H. Ohashi, K.T. Wikfeldt, et al., Selective probing of the OH or OD stretch vibration in liquid water using resonant inelastic soft-X-ray scattering, Phys. Rev. Lett. 111 (2013) 193001.
[28] A.F. Goncharov, V.V. Struzhkin, H.K. Mao, R.J. Hemley, Raman spectroscopy of dense H_2O and the transition to symmetric hydrogen bonds, Phys. Rev. Lett. 83

(1999) 1998–2001.
[29] B. Chen, I. Ivanov, M.L. Klein, M. Parrinello, Hydrogen bonding in water, Phys. Rev. Lett. 91 (2003) 215503.
[30] M.E. Tuckerman, D. Marx, M.L. Klein, M. Parrinello, On the quantum nature of the shared proton in hydrogen bonds, Science 275 (1997) 817–820.
[31] D. Marx, M.E. Tuckerman, J. Hutter, M. Parrinello, The nature of the hydrated excess proton in water, Nature 397 (1999) 601–604.
[32] L. Lin, J.A. Morrone, R. Car, Correlated tunneling in hydrogen bonds, J. Stat. Phys. 145 (2011) 365–384.
[33] C. Drechsel-Grau, D. Marx, Quantum simulation of collective proton tunneling in hexagonal ice crystals, Phys. Rev. Lett. 112 (2014) 148302.
[34] F. Yen, T. Gao, Dielectric anomaly in ice near 20 K: evidence of macroscopic quantum phenomena, J. Phys. Chem. Lett. 6 (2015) 2822–2825.
[35] P. Loubeyre, R. LeToullec, E. Wolanin, M. Hanfland, D. Husermann, Modulated phases and proton centring in ice observed by X-ray diffraction up to 170 GPa, Nature 397 (1999) 503–506.
[36] K. Hirsch, W. Holzapfel, Effect of high pressure on the Raman spectra of ice VIII and evidence for ice X, J. Chem. Phys. 84 (1986) 2771–2775.
[37] K.R. Hirsch, W.B. Holzapfel, Symmetric hydrogen bonds in ice X, Phys. Lett. A 101 (1984) 142–144.
[38] M.A. Henderson, The interaction of water with solid surfaces: fundamental aspects revisited, Surf. Sci. Rep. 46 (2002) 1–308.
[39] P.A. Thiel, T.E. Madey, The interaction of water with solid surfaces: fundamental aspects, Surf. Sci. Rep. 7 (1987) 211–385.
[40] A. Verdaguer, G.M. Sacha, H. Bluhm, M. Salmeron, Molecular structure of water at interfaces: wetting at the nanometer scale, Chem. Rev. 106 (2006) 1478–1510.
[41] J. Israelachvili, H. Wennerstrom, Role of hydration and water structure in biological and colloidal interactions, Nature 379 (1996) 219–225.
[42] Z. Zou, J. Ye, K. Sayama, H. Arakawa, Direct splitting of water under visible light irradiation with an oxide semiconductor photocatalyst, Nature 414 (2001) 625–627.
[43] N. Akiya, P.E. Savage, Roles of water for chemical reactions in high-temperature water, Chem. Rev. 102 (2002) 2725–2750.
[44] A. Kudo, Y. Miseki, Heterogeneous photocatalyst materials for water splitting, Chem. Soc. Rev. 38 (2009) 253–278.
[45] X.-Z. Li, M.I.J. Probert, A. Alavi, A. Michaelides, Quantum nature of the proton in water-hydroxyl overlayers on metal surfaces, Phys. Rev. Lett. 104 (2010) 066102.
[46] T. Kumagai, M. Kaizu, H. Okuyama, S. Hatta, T. Aruga, I. Hamada, Y. Morikawa, Symmetric hydrogen bond in a water-hydroxyl complex on Cu(110), Phys. Rev. B 81 (2010) 045402.
[47] T. Mitsui, M.K. Rose, E. Fomin, D.F. Ogletree, M. Salmeron, Water diffusion and clustering on Pd(111), Science 297 (2002) 1850–1852.
[48] V.A. Ranea, A. Michaelides, R. Ramirez, P.L. de Andres, J.A. Verges, D.A. King, Water dimer diffusion on Pd(111) assisted by an H-bond donor-acceptor tunneling exchange, Phys. Rev. Lett. 92 (2004) 136104.
[49] T. Kumagai, M. Kaizu, S. Hatta, H. Okuyama, T. Aruga, I. Hamada, Y. Morikawa, Direct observation of hydrogen-bond exchange within a single water dimer, Phys. Rev. Lett. 100 (2008) 166101.
[50] B. Roux, M. Karplus, Ion transport in a gramicidin-like channel: dynamics and mobility, J. Phys. Chem. 95 (1991) 4856–4868.
[51] R. Pomes, B. Roux, Structure and dynamics of a proton wire: a theoretical study of H^+ translocation along the single-file water chain in the gramicidin A channel, Biophys. J. 71 (1996) 19–39.
[52] K. Koga, G.T. Gao, H. Tanaka, X.C. Zeng, Formation of ordered ice nanotubes inside carbon nanotubes, Nature 412 (2001) 802–805.
[53] C. Dellago, M.M. Naor, G. Hummer, Proton transport through water-filled carbon nanotubes, Phys. Rev. Lett. 90 (2003) 105902.
[54] A.I. Kolesnikov, J.M. Zanotti, C.K. Loong, P. Thiyagarajan, A.P. Moravsky, R.O. Loutfy, C.J. Burnham, Anomalously soft dynamics of water in a nanotube: a revelation of nanoscale confinement, Phys. Rev. Lett. 93 (2004) 035503.
[55] Y. Maniwa, H. Kataura, M. Abe, A. Udaka, S. Suzuki, Y. Achiba, H. Kira, K. Matsuda, H. Kadowaki, Y. Okabe, Ordered water inside carbon nanotubes: formation of pentagonal to octagonal ice-nanotubes, Chem. Phys. Lett. 401 (2005) 534–538.
[56] G. Reiter, C. Burnham, D. Homouz, P.M. Platzman, J. Mayers, T. Abdul-Redah, A.P. Moravsky, J.C. Li, C.K. Loong, A.I. Kolesnikov, Anomalous behavior of proton zero point motion in water confined in carbon nanotubes, Phys. Rev. Lett. 97 (2006) 247801.
[57] V. Garbuio, C. Andreani, S. Imberti, A. Pietropaolo, G.F. Reiter, R. Senesi, M.A. Ricci, Proton quantum coherence observed in water confined in silica nanopores, J. Chem. Phys. 127 (2007) 154501.
[58] G.F. Reiter, A. Deb, Y. Sakurai, M. Itou, V.G. Krishnan, S.J. Paddison, Anomalous ground state of the electrons in nanoconfined water, Phys. Rev. Lett. 111 (2013) 036803.
[59] G. Algara-Siller, O. Lehtinen, F.C. Wang, R.R. Nair, U. Kaiser, H.A. Wu, A.K. Geim, I.V. Grigorieva, Square ice in graphene nanocapillaries, Nature 519 (2015) 443–445.
[60] A.I. Kolesnikov, G.F. Reiter, N. Choudhury, T.R. Prisk, E. Mamontov, A. Podlesnyak, G. Ehlers, A.G. Seel, D.J. Wesolowski, L.M. Anovitz, Quantum tunneling of water in beryl: a new state of the water molecule, Phys. Rev. Lett. 116 (2016) 167802.
[61] K.V. Agrawal, S. Shimizu, L.W. Drahushuk, D. Kilcoyne, M.S. Strano, Observation of extreme phase transition temperatures of water confined inside isolated carbon nanotubes, Nat. Nanotech. 12 (2017) 267–273.
[62] A.P. Drozdov, M.I. Eremets, I.A. Troyan, V. Ksenofontov, S.I. Shylin, Conventional superconductivity at 203 kelvin at high pressures in the sulfur hydride system, Nature 525 (2015) 73–76.
[63] S. Raugei, M.L. Klein, Nuclear quantum effects and hydrogen bonding in liquids, J. Am. Chem. Soc. 125 (2003) 8992–8993.
[64] C. Swalina, Q. Wang, A. Chakraborty, S. Hammes-Schiffer, Analysis of nuclear quantum effects on hydrogen bonding, J. Phys. Chem. A 111 (2007) 2206–2212.
[65] T. Koitaya, J. Yoshinobu, The quantum nature of C-H··· metal interaction: vibrational spectra and kinetic and geometric isotope effects of adsorbed cyclohexane, Chem. Rec. 14 (2014) 848–856.
[66] A. Douhal, S.K. Kim, A.H. Zewail, Femtosecond molecular dynamics of tautomerization in model base pairs, Nature 378 (1995) 260–263.
[67] O.H. Kwon, A.H. Zewail, Double proton transfer dynamics of model DNA base pairs in the condensed phase, Proc. Nat. Acad. Sci. U.S.A. 104 (2007) 8703–8708.
[68] A. Perez, M.E. Tuckerman, H.P. Hjalmarson, O.A. von Lilienfeld, Enol tautomers of watson-crick base pair models are metastable because of nuclear quantum effects, J. Am. Chem. Soc. 132 (2010) 11510–11515.
[69] J.K. Hwang, A. Warshel, How important are quantum mechanical nuclear motions in enzyme catalysis? J. Am. Chem. Soc. 118 (1996) 11745–11751.
[70] S.R. Billeter, S.P. Webb, P.K. Agarwal, T. Iordanov, S. Hammes-Schiffer, Hydride transfer in liver alcohol dehydrogenase: quantum dynamics, kinetic isotope effects, and role of enzyme motion, J. Am. Chem. Soc. 123 (2001) 11262–11272.
[71] J.Z. Pu, J.L. Gao, D.G. Truhlar, Multidimensional tunneling, recrossing, and the transmission coefficient for enzymatic reactions, Chem. Rev. 106 (2006) 3140–3169.
[72] D.R. Glowacki, J.N. Harvey, A.J. Mulholland, Taking Ockham's razor to enzyme dynamics and catalysis, Nat. Chem. 4 (2012) 169–176.
[73] L. Wang, S.D. Fried, S.G. Boxer, T.E. Markland, Quantum delocalization of protons in the hydrogen-bond network of an enzyme active site, Proc. Nat. Acad. Sci. U.S.A. 111 (2014) 18454–18459.
[74] D.G. Truhlar, Tunneling in enzymatic and nonenzymatic hydrogen transfer reactions, J. Phys. Org. Chem. 23 (2010) 660–676.
[75] L. Masgrau, A. Roujeinikova, L.O. Johannissen, P. Hothi, J. Basran, K.E. Ranaghan, A.J. Mulholland, M.J. Sutcliffe, N.S. Scrutton, D. Leys, Atomic description of an enzyme reaction dominated by proton tunneling, Science 312 (2006) 237–241.
[76] M.J. Sutcliffe, N.S. Scrutton, A new conceptual framework for enzyme catalysis. Hydrogen tunneling coupled to enzyme dynamics in flavoprotein and quinoprotein enzymes, Eur. J. Biochem. 269 (2002) 3096–3102.
[77] J.P. Klinman, A. Kohen, Hydrogen tunneling links protein dynamics to enzyme catalysis, Annu. Rev. Biochem 82 (2013) 471–496.
[78] Y.M. Efimova, S. Haemers, B. Wierczinski, W. Norde, A.A. van Well, Stability of globular proteins in H_2O and D_2O, Biopolymers 85 (2007) 264–273.
[79] Y. Cho, L.B. Sagle, S. Iimura, Y. Zhang, J. Kherb, A. Chilkoti, J.M. Scholtz, P.S. Cremer, Hydrogen bonding of beta-Turn structure is stabilized in D_2O, J. Am. Chem. Soc. 131 (2009) 15188–15193.
[80] O.V. Mosin, V.I. Shvets, D.A. Skladnev, I. Ignatov, Studying of microbic synthesis of deuterium labelled L-Phenylalanine by facultative methylotrophic bacterium brevibacterium methylicum on media with different content of heavy water, Russ. J. Biopharm 60 (2012) 11–22.

[81] D.C. Clary, D.M. Benoit, T. Van Mourik, H-densities: a new concept for hydrated molecules, Acc. Chem. Res. 33 (2000) 441–447.
[82] D.H. Zhang, M.A. Collins, S.Y. Lee, First-principles theory for the $H+H_2O$, D_2O reactions, Science 290 (2000) 961–963.
[83] M.A. Collins, Molecular potential-energy surfaces for chemical reaction dynamics, Theor. Chem. Acc. 108 (2002) 313–324.
[84] S.C. Althorpe, D.C. Clary, Quantum scattering calculations on chemical reactions, Annu. Rev. Phys. Chem. 54 (2003) 493–529.
[85] R.P. Feynman, A.R. Hibbs, Quantum Mechanics and Path Integrals, McGraw-Hill, New York, 1965.
[86] D. Chandler, P.G. Wolynes, Exploiting the isomorphism between quantum theory and classical statistical mechanics of polyatomic fluids, J. Chem. Phys. 74 (1981) 4078–4095.
[87] M. Parrinello, A. Rahman, Study of an F center in molten KCl, J. Chem. Phys. 80 (1984) 105–116.
[88] D.M. Ceperley, E.L. Pollock, Path-integral computation of the low-temperature properties of liquid ^{4}He, Phys. Rev. Lett. 56 (1986) 351–354.
[89] E.L. Pollock, D.M. Ceperley, Path-integral computation of superfluid densities, Phys. Rev. B 36 (1987) 8343–8352.
[90] D.M. Ceperley, Path integrals in the theory of condensed helium, Rev. Mod. Phys. 67 (1995) 279–355.
[91] M.E. Tuckerman, D. Marx, M.L. Klein, M. Parrinello, Efficient and general algorithms for path integral Car-Parrinello molecular dynamics, J. Chem. Phys. 104 (1996) 5579–5588.
[92] B. Berne, J, D. Thirumalai, On the simulation of quantum systems: path integral methods, Annu. Rev. Phys. Chem. 37 (2003) 401–424.
[93] M.A. Morales, C. Pierleoni, E. Schwegler, D.M. Ceperley, Evidence for a first-order liquid-liquid transition in high-pressure hydrogen from *ab initio* simulations, Proc. Nat. Acad. Sci. U.S.A. 107 (2010) 12799–12803.
[94] J.J. Morales, K. Singer, Path integral simulation of the free-energy of the (Lennard-Jones) neon, Mol. Phys. 73 (1991) 873–880.
[95] M. Tachikawa, M. Shiga, Geometrical H/D isotope effect on hydrogen bonds in charged water clusters, J. Am. Chem. Soc. 127 (2005) 11908–11909.
[96] A. Kaczmarek, M. Shiga, D. Marx, Quantum effects on vibrational and electronic spectra of hydrazine studied by "on-the-fly" *ab initio* ring polymer molecular dynamics, J. Phys. Chem. A 113 (2009) 1985–1994.
[97] S. Habershon, D.E. Manolopoulos, Thermodynamic integration from classical to quantum mechanics, J. Chem. Phys. 135 (2011).
[98] X.-Z. Li, B. Walker, A. Michaelides, Quantum nature of the hydrogen bond, Proc. Nat. Acad. Sci. U.S.A. 108 (2011) 6369–6373.
[99] A. Perez, O.A. von Lilienfeld, Path integral computation of quantum free energy differences due to alchemical transformations involving mass and potential, J. Chem. Theory Comput. 7 (2011) 2358–2369.
[100] J. Chen, X.-Z. Li, Q. Zhang, M.I.J. Probert, C.J. Pickard, R.J. Needs, A. Michaelides, E. Wang, Quantum simulation of low-temperature metallic liquid hydrogen, Nat. Commun. 4 (2013) 2064.
[101] M.A. Morales, J.M. McMahon, C. Pierleoni, D.M. Ceperley, Nuclear quantum effects and nonlocal exchange-correlation functionals applied to liquid hydrogen at high pressure, Phys. Rev. Lett. 110 (2013) 065702.
[102] Y. Feng, J. Chen, D. Alfe, X.-Z. Li, E. Wang, Nuclear quantum effects on the high pressure melting of dense lithium, J. Chem. Phys. 142 (2015) 064506.
[103] M. Pavese, S. Chawla, D. Lu, J. Lobaugh, G.A. Voth, Quantum effects and the excess proton in water, J. Chem. Phys. 107 (1997) 7428–7432.
[104] C. Swalina, S. Hammes-Schiffer, Impact of nuclear quantum effects on the molecular structure of bihalides and the hydrogen fluoride dimer, J. Phys. Chem. A 109 (2005) 10410–10417.
[105] J.A. Morrone, V. Srinivasan, D. Sebastiani, R. Car, Proton momentum distribution in water: an open path integral molecular dynamics study, J. Chem. Phys. 126 (2007) 234504.
[106] J.A. Morrone, R. Car, Nuclear quantum effects in water, Phys. Rev. Lett. 101 (2008) 017801.
[107] J.A. Morrone, L. Lin, R. Car, Tunneling and delocalization effects in hydrogen bonded systems: a study in position and momentum space, J. Chem. Phys. 130 (2009) 204511.
[108] L. Lin, J.A. Morrone, R. Car, M. Parrinello, Displaced path integral formulation for the momentum distribution of quantum particles, Phys. Rev. Lett. 105 (2010) 110602.
[109] L. Lin, J.A. Morrone, R. Car, M. Parrinello, Momentum distribution, vibrational dynamics, and the potential of mean force in ice, Phys. Rev. B 83 (2011) 220302.
[110] L. Wang, M. Ceriotti, T.E. Markland, Quantum fluctuations and isotope effects in *ab initio* descriptions of water, J. Chem. Phys. 141 (2014) 104502.
[111] W. Fang, J. Chen, M. Rossi, Y. Feng, X.-Z. Li, A. Michaelides, Inverse temperature dependence of nuclear quantum effects in DNA base pairs, J. Phys. Chem. Lett. 7 (2016) 2125–2131.
[112] A. Pietropaolo, R. Senesi, C. Andreani, A. Botti, M.A. Ricci, F. Bruni, Excess of proton mean kinetic energy in supercooled water, Phys. Rev. Lett. 100 (2008) 127802.
[113] R. Senesi, D. Flammini, A.I. Kolesnikov, E.D. Murray, G. Galli, C. Andreani, The quantum nature of the OH stretching mode in ice and water probed by neutron scattering experiments, J. Chem. Phys. 139 (2013) 074504.
[114] R. Senesi, G. Romanelli, M.A. Adams, C. Andreani, Temperature dependence of the zero point kinetic energy in ice and water above room temperature, Chem. Phys. 427 (2013) 111–116.
[115] A. Zeidler, P.S. Salmon, H.E. Fischer, J.C. Neuefeind, J.M. Simonson, H. Lemmel, H. Rauch, T.E. Markland, Oxygen as a site specific probe of the structure of water and oxide materials, Phys. Rev. Lett. 107 (2011) 145501.
[116] G. Romanelli, M. Ceriotti, D.E. Manolopoulos, C. Pantalei, R. Senesi, C. Andreani, Direct measurement of competing quantum effects on the kinetic energy of heavy water upon melting, J. Phys. Chem. Lett. 4 (2013) 3251–3256.
[117] C.J. Burnham, G.F. Reiter, J. Mayers, T. Abdul-Redah, H. Reichert, H. Dosch, On the origin of the redshift of the OH stretch in Ice Ih: evidence from the momentum distribution of the protons and the infrared spectral density, Phys. Chem. Chem. Phys. 8 (2006) 3966–3977.
[118] C.J. Burnham, D.J. Anick, P.K. Mankoo, G.F. Reiter, The vibrational proton potential in bulk liquid water and ice, J. Chem. Phys. 128 (2008) 154519.
[119] C. Pantalei, A. Pietropaolo, R. Senesi, S. Imberti, C. Andreani, J. Mayers, C. Burnham, G. Reiter, Proton momentum distribution of liquid water from room temperature to the supercritical phase, Phys. Rev. Lett. 100 (2008) 177801.
[120] G.F. Reiter, A.I. Kolesnikov, S.J. Paddison, P.M. Platzman, A.P. Moravsky, M.A. Adams, J. Mayers, Evidence for an anomalous quantum state of protons in nanoconfined water, Phys. Rev. B 85 (2012) 045403.
[121] A.R. Ubbelohde, K.J. Gallagher, Acid-base effects in hydrogen bonds in crystals, Acta Crystallogr. 8 (1955) 71–83.
[122] D.T. Major, A. Heroux, A.M. Orville, M.P. Valley, P.F. Fitzpatrick, J.L. Gao, Differential quantum tunneling contributions in nitroalkane oxidase catalyzed and the uncatalyzed proton transfer reaction, Proc. Nat. Acad. Sci. U.S.A. 106 (2009) 20734–20739.
[123] K. Aoki, H. Yamawaki, M. Sakashita, H. Fujihisa, Infrared absorption study of the hydrogen-bond symmetrization in ice to 110 GPa, Phys. Rev. B 54 (1996) 15673–15677.
[124] A.F. Goncharov, V.V. Struzhkin, M.S. Somayazulu, R.J. Hemley, H.K. Mao, Compression of ice to 210 gigapascals: infrared evidence for a symmetric hydrogen-bonded phase, Science 273 (1996) 218–220.
[125] A. Polian, M. Grimsditch, New high-pressure phase of H_2O: ice X, Phys. Rev. Lett. 52 (1984) 1312–1314.
[126] Y. Nagata, R.E. Pool, E.H.G. Backus, M. Bonn, Nuclear quantum effects affect bond orientation of water at the water-vapor interface, Phys. Rev. Lett. 109 (2012) 226101.
[127] A.J. Heinrich, C.P. Lutz, J.A. Gupta, D.M. Eigler, Molecule cascades, Science 298 (2002) 1381–1387.
[128] J. Repp, G. Meyer, K.H. Rieder, P. Hyldgaard, Site determination and thermally assisted tunneling in homogenous nucleation, Phys. Rev. Lett. 91 (2003) 206102.
[129] J.A. Stroscio, R.J. Celotta, Controlling the dynamics of a single atom in lateral atom manipulation, Science 306 (2004) 242–247.
[130] T. Kumagai, A. Shiotari, H. Okuyama, S. Hatta, T. Aruga, I. Hamada, T. Frederiksen, H. Ueba, H-atom relay reactions in real space, Nat. Mater. 11 (2012) 167–172.
[131] X. Meng, J. Guo, J. Peng, J. Chen, Z. Wang, J.-R. Shi, X.-Z. Li, E.-G. Wang, Y. Jiang, Direct visualization of concerted proton tunnelling in a water nanocluster, Nat. Phys. 11 (2015) 235–239.

[132] J. Guo, J.-T. Lü, Y. Feng, J. Chen, J. Peng, Z. Lin, X. Meng, Z. Wang, X.-Z. Li, E.-G. Wang, et al., Nuclear quantum effects of hydrogen bonds probed by tip-enhanced inelastic electron tunneling, Science 352 (2016) 321–325.
[133] M. Koch, M. Pagan, M. Persson, S. Gawinkowski, J. Waluk, T. Kumagai, Direct observation of double hydrogen transfer via quantum tunneling in a single porphycene molecule on a Ag(110) surface, J. Am. Chem. Soc. 139 (2017) 12681–12687.
[134] C. Andreani, D. Colognesi, J. Mayers, G.F. Reiter, R. Senesi, Measurement of momentum distribution of light atoms and molecules in condensed matter systems using inelastic neutron scattering, Adv. Phys. 54 (2005) 377–469.
[135] C. Andreani, G. Romanelli, R. Senesi, A combined INS and DINS study of proton quantum dynamics of ice and water across the triple point and in the supercritical phase, Chem. Phys. 427 (2013) 106–110.
[136] C. Drechsel-Grau, D. Marx, Collective proton transfer in ordinary ice: local environments, temperature dependence and deuteration effects, Phys. Chem. Chem. Phys. 19 (2017) 2623–2635.
[137] J. Repp, G. Meyer, S.M. Stojkovic, A. Gourdon, C. Joachim, Molecules on insulating films: scanning-tunneling microscopy imaging of individual molecular orbitals, Phys. Rev. Lett. 94 (2005) 026803.
[138] C. Weiss, C. Wagner, C. Kleimann, M. Rohlfing, F.S. Tautz, R. Temirov, Imaging pauli repulsion in scanning tunneling microscopy, Phys. Rev. Lett. 105 (2010) 086103.
[139] C. Weiss, C. Wagner, R. Temirov, F.S. Tautz, Direct imaging of intermolecular bonds in scanning tunneling microscopy, J. Am. Chem. Soc. 132 (2010) 11864–11865.
[140] B.C. Stipe, M.A. Rezaei, W. Ho, Single-molecule vibrational spectroscopy and microscopy, Science 280 (1998) 1732–1735.
[141] B.C. Stipe, H.A. Rezaei, W. Ho, Localization of inelastic tunneling and the determination of atomic-scale structure with chemical specificity, Phys. Rev. Lett. 82 (1999) 1724–1727.
[142] C.L. Chiang, C. Xu, Z.M. Han, W. Ho, Real-space imaging of molecular structure and chemical bonding by single-molecule inelastic tunneling probe, Science 344 (2014) 885–888.
[143] D.M. Eigler, E.K. Schweizer, Positioning single atoms with as a scanning tunneling microscope, Nature 344 (1990) 524–526.
[144] J.A. Stroscio, D.M. Eigler, Atomic and molecular manipulation with the scanning tunneling microscope, Science 254 (1991) 1319–1326.
[145] P.J. Feibelman, The first wetting layer on a solid, Phys. Today 63 (2010) 34–39.
[146] J. Carrasco, A. Hodgson, A. Michaelides, A molecular perspective of water at metal interfaces, Nat. Mater. 11 (2012) 667–674.
[147] S. Maier, M. Salmeron, How does water wet a surface? Acc. Chem. Res. 48 (2015) 2783–2790.
[148] M. Salmeron, H. Bluhm, N. Tatarkhanov, G. Ketteler, T.K. Shimizu, A. Mugarza, X. Deng, T. Herranz, S. Yamamoto, A. Nilsson, Water growth on metals and oxides: binding, dissociation and role of hydroxyl groups, Faraday Discuss. 141 (2009) 221–229.
[149] B. Hammer, S. Wendt, F. Besenbacher, Water Adsorption on TiO_2, Top. Catal. 53 (2010) 423–430.
[150] R.T. Mu, Z.J. Zhao, Z. Dohnalek, J.L. Gong, Structural motifs of water on metal oxide surfaces, Chem. Soc. Rev. 46 (2017) 1785–1806.
[151] W. Ho, Single-molecule chemistry, J. Chem. Phys. 117 (2002) 11033–11061.
[152] Y. Kim, K. Motobayashi, T. Frederiksen, H. Ueba, M. Kawai, Action spectroscopy for single-molecule reactions - experiments and theory, Prog. Surf. Sci. 90 (2015) 85–143.
[153] K. Morgenstern, Scanning tunnelling microscopy investigation of water in submonolayer coverage on Ag(111), Surf. Sci. 504 (2002) 293–300.
[154] A. Michaelides, K. Morgenstern, Ice nanoclusters at hydrophobic metal surfaces, Nat. Mater. 6 (2007) 597–601.
[155] J. Carrasco, A. Michaelides, M. Forster, S. Haq, R. Raval, A. Hodgson, A one-dimensional ice structure built from pentagons, Nat. Mater. 8 (2009) 427–431.
[156] M. Tatarkhanov, D.F. Ogletree, F. Rose, T. Mitsui, E. Fomin, S. Maier, M. Rose, J.I. Cerda, M. Salmeron, Metal- and hydrogen-bonding competition during water adsorption on Pd(111) and Ru(0001), J. Am. Chem. Soc. 131 (2009) 18425–18434.
[157] S. Nie, P.J. Feibelman, N.C. Bartelt, K. Thurmer, Pentagons and heptagons in the first water layer on Pt(111), Phys. Rev. Lett. 105 (2010) 026102.
[158] K. Thurmer, S. Nie, P.J. Feibelman, N.C. Bartelt, Clusters, molecular layers, and 3D crystals of water on Ni(111), J. Chem. Phys. 141 (2014) 18C520.
[159] T. Yamada, S. Tamamori, H. Okuyama, T. Aruga, Anisotropic water chain growth on Cu(110) observed with scanning tunneling microscopy, Phys. Rev. Lett. 96 (2006) 036105.
[160] T. Kumagai, H. Okuyama, S. Hatta, T. Aruga, I. Hamada, Water clusters on Cu(110): chain versus cyclic structures, J. Chem. Phys. 134 (2011) 024703.
[161] I. Horcas, R. Fernandez, J.M. Gomez-Rodriguez, J. Colchero, J. Gomez-Herrero, A.M. Baro, WSXM: a software for scanning probe microscopy and a tool for nanotechnology, Rev. Sci. Instrum. 78 (2007) 013705.
[162] G. Kresse, J. Hafner, *Ab initio* molecular dynamics for liquid metals, Phys. Rev. B 47 (1993) 558–561.
[163] G. Kresse, J. Furthmuller, Efficient iterative schemes for *ab initio* total-energy calculations using a plane-wave basis set, Phys. Rev. B 54 (1996) 11169–11186.
[164] J. Klimes, D.R. Bowler, A. Michaelides, Van der Waals density functionals applied to solids, Phys. Rev. B 83 (2011) 195131.
[165] G. Kresse, D. Joubert, From ultrasoft pseudopotentials to the projector augmented-wave method, Phys. Rev. B 59 (1999) 1758–1775.
[166] K. Lauwaet, K. Schouteden, E. Janssens, C. Van Haesendonck, P. Lievens, M.I. Trioni, L. Giordano, G. Pacchioni, Resolving all atoms of an alkali halide via nanomodulation of the thin NaCl film surface using the Au(111) reconstruction, Phys. Rev. B 85 (2012) 245440.
[167] F. Matthaei, S. Heidorn, K. Boom, C. Bertram, A. Safiei, J. Henzl, K. Morgenstern, Coulomb attraction during the carpet growth mode of NaCl, J. Phys.: Condens. Matter 24 (2012) 354006.
[168] W. Hebenstreit, J. Redinger, Z. Horozova, M. Schmid, R. Podloucky, P. Varga, Atomic resolution by STM on ultra-thin films of alkali halides: experiment and local density calculations, Surf. Sci. 424 (1999) L321–L328.
[169] A. Michaelides, V.A. Ranea, P.L. de Andres, D.A. King, General model for water monomer adsorption on close-packed transition and noble metal surfaces, Phys. Rev. Lett. 90 (2003) 216102.
[170] P. Cabrera-Sanfelix, A. Arnau, G.R. Darling, D. Sanchez-Portal, Water adsorption and diffusion on NaCl(100), J. Phys. Chem. B 110 (2006) 24559–24564.
[171] Y. Yang, S. Meng, E.G. Wang, Water adsorption on a NaCl (001) surface: a density functional theory study, Phys. Rev. B 74 (2006) 245409.
[172] J.K. Norskov, Chemisorption on metal surfaces, Rep. Prog. Phys. 53 (1990) 1253–1295.
[173] J.I. Martinez, E. Abad, C. Gonzalez, F. Flores, J. Ortega, Improvement of scanning tunneling microscopy resolution with H-sensitized tips, Phys. Rev. Lett. 108 (2012) 246102.
[174] T.J. Lawton, J. Carrasco, A.E. Baber, A. Michaelides, E.C.H. Sykes, Visualization of hydrogen bonding and associated chirality in methanol hexamers, Phys. Rev. Lett. 107 (2011) 256101.
[175] J. Guo, X.Z. Meng, J. Chen, J.B. Peng, J.M. Sheng, X.Z. Li, L.M. Xu, J.R. Shi, E.G. Wang, Y. Jiang, Real-space imaging of interfacial water with submolecular resolution, Nat. Mater. 13 (2014) 184–189.
[176] S. Meng, E.G. Wang, S.W. Gao, Water adsorption on metal surfaces: A general picture from density functional theory studies, Phys. Rev. B 69 (2004) 195404.
[177] J. Chen, J. Guo, X. Meng, J. Peng, J. Sheng, L. Xu, Y. Jiang, X.-Z. Li, E.-G. Wang, An unconventional bilayer ice structure on a NaCl(001) film, Nat. Commun. 5 (2014) 4056.
[178] N. Bjerrum, Structure and properties of ice, Science 115 (1952) 385–390.
[179] M. Forster, R. Raval, A. Hodgson, J. Carrasco, A. Michaelides, c(2 x 2) Water-hydroxyl layer on Cu(110): a wetting layer stabilized by Bjerrum defects, Phys. Rev. Lett. 106 (2011) 046103.
[180] A. Shiotari, Y. Sugimoto, Ultrahigh-resolution imaging of water networks by atomic force microscopy, Nat. Commun. 8 (2017) 14313.
[181] J.D. Bernal, R.H. Fowler, A theory of water and ionic solution, with particular reference to hydrogen and hydroxyl ions, J. Chem. Phys. 1 (1933) 515–548.
[182] F. Huisken, M. Kaloudis, A. Kulcke, Infrared spectroscopy of small size-selected water clusters, J. Chem. Phys. 104 (1996) 17–25.
[183] U. Buck, F. Huisken, Infrared spectroscopy of size-selected water and methanol clusters, Chem. Rev. 100 (2000) 3863–3890.
[184] C.J. Fecko, J.D. Eaves, J.J. Loparo, A. Tokmakoff, P.L. Geissler, Ultrafast hydrogen-bond dynamics in the infrared spectroscopy of water, Science 301 (2003) 1698–1702.
[185] H.J. Bakker, J.L. Skinner, Vibrational spectroscopy as a probe of structure and dynamics in liquid water, Chem. Rev. 110 (2010) 1498–1517.

[186] F. Bensebaa, T.H. Ellis, Water at surfaces: what can we learn from vibrational spectroscopy? Prog. Surf. Sci. 50 (1995) 173–185.
[187] Q. Du, R. Superfine, E. Freysz, Y.R. Shen, Vibrational spectroscopy of water at the vapor/water interface, Phys. Rev. Lett. 70 (1993) 2313–2316.
[188] Y.R. Shen, V. Ostroverkhov, Sum-frequency vibrational spectroscopy on water interfaces: polar orientation of water molecules at interfaces, Chem. Rev. 106 (2006) 1140–1154.
[189] R.C. Jaklevic, J. Lambe, Molecular vibration spectra by electron tunneling, Phys. Rev. Lett. 17 (1966) 1139.
[190] T. Komeda, Chemical identification and manipulation of molecules by vibrational excitation via inelastic tunneling process with scanning tunneling microscopy, Prog. Surf. Sci. 78 (2005) 41–85.
[191] M. Galperin, M.A. Ratner, A. Nitzan, Molecular transport junctions: vibrational effects, J. Phys.: Condens. Matter 19 (2007) 103201.
[192] N. Lorente, M. Persson, Theory of single molecule vibrational spectroscopy and microscopy, Phys. Rev. Lett. 85 (2000) 2997–3000.
[193] M. Galperin, M.A. Ratner, A. Nitzan, A. Troisi, Nuclear coupling and polarization in molecular transport junctions: beyond tunneling to function, Science 319 (2008) 1056–1060.
[194] K. Morgenstern, J. Nieminen, Intermolecular bond length of ice on Ag(111), Phys. Rev. Lett. 88 (2002) 066102.
[195] H. Okuyama, I. Hamada, Hydrogen-bond imaging and engineering with a scanning tunnelling microscope, J. Phys. D: Appl. Phys. 44 (2011) 464004.
[196] B.N.J. Persson, A. Baratoff, Inelastic electron tunneling from a metal tip: the contribution from resonant processes, Phys. Rev. Lett. 59 (1987) 339–342.
[197] H. Song, Y. Kim, Y.H. Jang, H. Jeong, M.A. Reed, T. Lee, Observation of molecular orbital gating, Nature 462 (2009) 1039–1043.
[198] J.T. Lü, R.B. Christensen, G. Foti, T. Frederiksen, T. Gunst, M. Brandbyge, Efficient calculation of inelastic vibration signals in electron transport: beyond the wide-band approximation, Phys. Rev. B 89 (2014) 081405.
[199] J.M. Soler, E. Artacho, J.D. Gale, A. Garcia, J. Junquera, P. Ordejon, D. Sanchez-Portal, The SIESTA method for *ab initio* order-N materials simulation, J. Phys.: Condens. Matter 14 (2002) 2745–2779.
[200] M. Brandbyge, J.L. Mozos, P. Ordejon, J. Taylor, K. Stokbro, Density-functional method for nonequilibrium electron transport, Phys. Rev. B 65 (2002) 165401.
[201] T. Frederiksen, M. Paulsson, M. Brandbyge, A.-P. Jauho, Inelastic transport theory from first principles: methodology and application to nanoscale devices, Phys. Rev. B 75 (2007) 205413.
[202] N. Lorente, M. Persson, L.J. Lauhon, W. Ho, Symmetry selection rules for vibrationally inelastic tunneling, Phys. Rev. Lett. 86 (2001) 2593–2596.
[203] M. Ohara, Y. Kim, S. Yanagisawa, Y. Morikawa, M. Kawai, Role of molecular orbitals near the Fermi level in the excitation of vibrational modes of a single molecule at a scanning tunneling microscope junction, Phys. Rev. Lett. 100 (2008) 136104.
[204] M. Galperin, M.A. Ratner, A. Nitzan, Inelastic electron tunneling spectroscopy in molecular junctions: peaks and dips, J. Chem. Phys. 121 (2004) 11965–11979.
[205] A. Baratoff, B.N.J. Persson, Theory of the local tunneling spectrum of a vibrating adsorbate, J. Vac. Sci. Technol., A 6 (1988) 331–335.
[206] M. Rozenberg, A. Loewenschuss, Y. Marcus, An empirical correlation between stretching vibration redshift and hydrogen bond length, Phys. Chem. Chem. Phys. 2 (2000) 2699–2702.
[207] W.A. Hofer, A.S. Foster, A.L. Shluger, Theories of scanning probe microscopes at the atomic scale, Rev. Mod. Phys. 75 (2003) 1287–1331.
[208] B. Hammer, J.K. Norskov, Theoretical surface science and catalysis-calculations and concepts, Adv. Catal. 45 (2000) 71–129.
[209] M. Bockstedte, A. Kley, J. Neugebauer, M. Scheffler, Density-functional theory calculations for poly-atomic systems: electronic structure, static and elastic properties and ab initio molecular dynamics, Comput. Phys. Commun. 107 (1997) 187–222.
[210] G. Henkelman, H. Jonsson, Improved tangent estimate in the nudged elastic band method for finding minimum energy paths and saddle points, J. Chem. Phys. 113 (2000) 9978–9985.
[211] A.J. Cohen, P. Mori-Sanchez, W. Yang, Challenges for density functional theory, Chem. Rev. 112 (2012) 289–320.
[212] D.H.W. Dickson, A.R. Ubbelohde, The hydrogen bond in crystals. VIII. The isotope effect in KH_2AsO_4, Acta Crystallogr. 3 (1950) 6–9.
[213] E. Matsushita, T. Matsubara, Note on isotope effect in hydrogen bonded crystals, Prog. Theor. Phys. 67 (1982) 1–19.
[214] K. Diri, E.M. Myshakin, K.D. Jordan, On the contribution of vibrational anharmonicity to the binding energies of water clusters, J. Phys. Chem. A 109 (2005) 4005–4009.
[215] P.J. Feibelman, Partial dissociation of water on Ru(0001), Science 295 (2002) 99–102.
[216] D. Alfe, M.J. Gillan, *Ab initio* statistical mechanics of surface adsorption and desorption. II. Nuclear quantum effects, J. Chem. Phys. 133 (2010) 044103.
[217] T.R. Mattsson, U. Engberg, G. Wahnstrom, H diffusion on Ni(100): a quantum Monte Carlo simulation, Phys. Rev. Lett. 71 (1993) 2615–2618.
[218] L.Y. Chen, S.C. Ying, Theory of surface diffusion: crossover from classical to quantum regime, Phys. Rev. Lett. 73 (1994) 700–703.
[219] T.R. Mattsson, G. Wahnstrom, Quantum Monte Carlo study of surface diffusion, Phys. Rev. B 51 (1995) 1885–1896.
[220] T.R. Mattsson, G. Wahnstrom, Isotope effect in hydrogen surface diffusion, Phys. Rev. B 56 (1997) 14944–14947.
[221] T.R. Mattsson, G. Wahnstrom, L. Bengtsson, B. Hammer, Quantum-mechanical calculation of H on Ni(001) using a model potential based on first-principles calculations, Phys. Rev. B 56 (1997) 2258–2266.
[222] J. Kua, L.J. Lauhon, W. Ho, W.A. Goddard, Direct comparisons of rates for low temperature diffusion of hydrogen and deuterium on Cu(001) from quantum mechanical calculations and scanning tunneling microscopy experiments, J. Chem. Phys. 115 (2001) 5620–5624.
[223] E.M. McIntosh, K.T. Wikfeldt, J. Ellis, A. Michaelides, W. Allison, Quantum effects in the diffusion of hydrogen on Ru(0001), J. Phys. Chem. Lett. 4 (2013) 1565–1569.
[224] P.-O. Löwdin, Proton tunneling in DNA and its biological implications, Rev. Mod. Phys. 35 (1963) 724–732.
[225] E.F. Caldin, Tunneling in proton-transfer reactions in solution, Chem. Rev. 69 (1969) 135–156.
[226] K.D. Kreuer, Proton conductivity: materials and applications, Chem. Mater. 8 (1996) 610–641.
[227] R.A.W. Frank, C.M. Titman, J.V. Pratap, B.F. Luisi, R.N. Perham, A molecular switch and proton wire synchronize the active sites in thiamine enzymes, Science 306 (2004) 872–876.
[228] S. Horiuchi, Y. Tokunaga, G. Giovannetti, S. Picozzi, H. Itoh, R. Shimano, R. Kumai, Y. Tokura, Above-room-temperature ferroelectricity in a single-component molecular crystal, Nature 463 (2010) 789–792.
[229] A.H. Castro Neto, P. Pujol, E. Fradkin, Ice: a strongly correlated proton system, Phys. Rev. B 74 (2006) 024302.
[230] P. Liljeroth, J. Repp, G. Meyer, Current-induced hydrogen tautomerization and conductance switching of naphthalocyanine molecules, Science 317 (2007) 1203–1206.
[231] W. Auwarter, K. Seufert, F. Bischoff, D. Ecija, S. Vijayaraghavan, S. Joshi, F. Klappenberger, N. Samudrala, J.V. Barth, A surface-anchored molecular four-level conductance switch based on single proton transfer, Nat. Nanotech. 7 (2012) 41–46.
[232] T. Kumagai, F. Hanke, S. Gawinkowski, J. Sharp, K. Kotsis, J. Waluk, M. Persson, L. Grill, Controlling intramolecular hydrogen transfer in a porphycene molecule with single atoms or molecules located nearby, Nat. Chem. 6 (2014) 41–46.
[233] C. Drechsel-Grau, D. Marx, Exceptional isotopic-substitution effect: breakdown of collective proton tunneling in hexagonal ice due to partial deuteration, Angew. Chem. Int. Ed. 53 (2014) 10937–10940.
[234] C. Drechsel-Grau, D. Marx, Tunneling in chiral water clusters. Protons in concert, Nat. Phys. 11 (2015) 216–218.
[235] T. Huang, J. Zhao, M. Peng, A.A. Popov, S. Yang, L. Dunsch, H. Petek, A molecular switch based on current-driven rotation of an encapsulated cluster within a fullerene cage, Nano Lett. 11 (2011) 5327–5332.
[236] H. Gawronski, J. Carrasco, A. Michaelides, K. Morgenstern, Manipulation and control of hydrogen bond dynamics in absorbed ice nanoclusters, Phys. Rev. Lett. 101 (2008) 136102.
[237] H. Petek, J. Zhao, Ultrafast interfacial proton-coupled electron transfer, Chem. Rev. 110 (2010) 7082–7099.
[238] G. Henkelman, B.P. Uberuaga, H. Jonsson, A climbing image nudged elastic band method for finding saddle points and minimum energy paths, J. Chem. Phys. 113 (2000) 9901–9904.
[239] A.J. Horsewill, Quantum tunnelling in the hydrogen bond, Prog. Nucl. Magn. Reson. Spectrosc. 52 (2008) 170–196.
[240] E.J. Spahr, L. Wen, M. Stavola, L.A. Boatner, L.C. Feldman, N.H. Tolk, G. Lupke, Proton tunneling: a decay channel of the O-H stretch mode in $KTaO_3$, Phys. Rev. Lett. 102 (2009) 075506.

[241] L. Pauling, The structure and entropy of ice and of other crystals with some randomness of atomic arrangement, J. Am. Chem. Soc. 57 (1935) 2680–2684.
[242] O. Benton, O. Sikora, N. Shannon, Classical and quantum theories of proton disorder in hexagonal water ice, Phys. Rev. B 93 (2016) 125143.
[243] E. Schwegler, M. Sharma, F. Gygi, G. Galli, Melting of ice under pressure, Proc. Nat. Acad. Sci. U.S.A. 105 (2008) 14779–14783.
[244] J.K. Gregory, D.C. Clary, Structure of water clusters. The contribution of many-body forces, monomer relaxation, and vibrational zero-point energy, J. Phys. Chem. 100 (1996) 18014–18022.
[245] G.A. Voth, D. Chandler, W.H. Miller, Rigorous formulation of quantum transition state theory and its dynamical corrections, J. Chem. Phys. 91 (1989) 7749–7760.
[246] A. Shiotari, H. Okuyama, S. Hatta, T. Aruga, M. Alducin, T. Frederiksen, Role of valence states of adsorbates in inelastic electron tunneling spectroscopy: a study of nitric oxide on Cu(110) and Cu(001), Phys. Rev. B 94 (2016) 075442.
[247] I.V. Stiopkin, C. Weeraman, P.A. Pieniazek, F.Y. Shalhout, J.L. Skinner, A.V. Benderskii, Hydrogen bonding at the water surface revealed by isotopic dilution spectroscopy, Nature 474 (2011) 192–195.
[248] A.V. Iogansen, Direct proportionality of the hydrogen bonding energy and the intensification of the stretching ν(XH) vibration in infrared spectra, Spectrochim. Acta, Part A 55 (1999) 1585–1612.
[249] Y. Terada, S. Yoshida, O. Takeuchi, H. Shigekawa, Real-space imaging of transient carrier dynamics by nanoscale pump-probe microscopy, Nat. Photonics 4 (2010) 869–874.
[250] S. Yoshida, Y. Aizawa, Z.H. Wang, R. Oshima, Y. Mera, E. Matsuyama, H. Oigawa, O. Takeuchi, H. Shigekawa, Probing ultrafast spin dynamics with optical pump-probe scanning tunnelling microscopy, Nat. Nanotech. 9 (2014) 588–593.
[251] L. Gross, F. Mohn, N. Moll, P. Liljeroth, G. Meyer, The chemical structure of a molecule resolved by atomic force microscopy, Science 325 (2009) 1110–1114.
[252] L. Gross, F. Mohn, N. Moll, G. Meyer, R. Ebel, W.M. Abdel-Mageed, M. Jaspars, Organic structure determination using atomic-resolution scanning probe microscopy, Nat. Chem. 2 (2010) 821–825.
[253] J. Zhang, P.C. Chen, B.K. Yuan, W. Ji, Z.H. Cheng, X.H. Qiu, Real-space identification of intermolecular bonding with atomic force microscopy, Science 342 (2013) 611–614.
[254] P. Hapala, M. Svec, O. Stetsovych, N.J. van der Heijden, M. Ondracek, J. van der Lit, P. Mutombo, I. Swart, P. Jelinek, Mapping the electrostatic force field of single molecules from high-resolution scanning probe images, Nat. Commun. 7 (2016) 11560.
[255] J. van der Lit, F. Di Cicco, P. Hapala, P. Jelinek, I. Swart, Submolecular resolution imaging of molecules by atomic force microscopy: the influence of the electrostatic force, Phys. Rev. Lett. 116 (2016) 096102.
[256] F.J. Giessibl, Advances in atomic force microscopy, Rev. Mod. Phys. 75 (2003) 949–983.
[257] S. Kawai, T. Nishiuchi, T. Kodama, P. Spijker, R. Pawlak, T. Meier, J. Tracey, T. Kubo, E. Meyer, A.S. Foster, Direct quantitative measurement of the C=O··· H-C bond by atomic force microscopy, Sci. Adv. 3 (2017) e1603258.
[258] J. Peng, J. Guo, P. Hapala, D. Cao, R. Ma, B. Cheng, L. Xu, M. Ondráček, P. Jelínek, E.-G. Wang, et al., Submolecular-resolution non-invasive imaging of interfacial water with atomic force microscopy, arXiv (2017) 1703.04400.
[259] H.J. Mamin, M. Kim, M.H. Sherwood, C.T. Rettner, K. Ohno, D.D. Awschalom, D. Rugar, Nanoscale nuclear magnetic resonance with a nitrogen-vacancy spin sensor, Science 339 (2013) 557–560.
[260] T. Staudacher, F. Shi, S. Pezzagna, J. Meijer, J. Du, C.A. Meriles, F. Reinhard, J. Wrachtrup, Nuclear magnetic resonance spectroscopy on a (5-nanometer)^3 sample volume, Science 339 (2013) 561–563.
[261] N. Aslam, M. Pfender, P. Neumann, R. Reuter, A. Zappe, F. Favaro de Oliveira, A. Denisenko, H. Sumiya, S. Onoda, J. Isoya, et al., Nanoscale nuclear magnetic resonance with chemical resolution, Science 357 (2017) 67–71.